1994

Muon transfer from muonic deuterium to carbon

David William Viel
College of William & Mary - Arts & Sciences

Order Number 9501415

Muon transfer from muonic deuterium to carbon

Viel, David William, Ph.D.

The College of William and Mary, 1994

U·M·I
300 N. Zeeb Rd.
Ann Arbor, MI 48106

MUON TRANSFER FROM MUONIC DEUTERIUM TO CARBON

A Dissertation

Presented to

The Faculty of the Department of Physics

The College of William and Mary in Virginia

In Partial Fulfillment

of the Requirements for the Degree of

Doctor of Philosophy

---

by

David William Viel

1993

APPROVAL SHEET

This dissertation is submitted in partial fulfilment of
the requirements for the degree of

Doctor of Philosophy

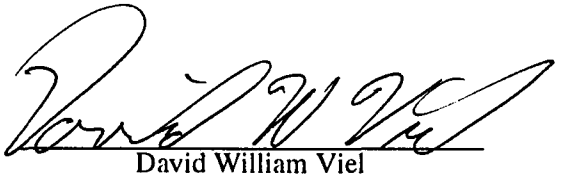

David William Viel

Approved, December 1993

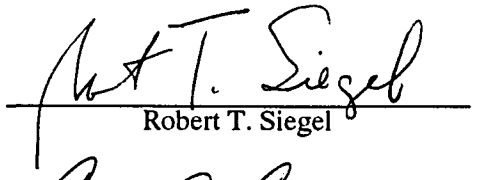

Robert T. Siegel

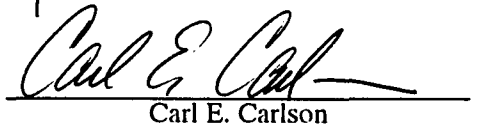

Carl E. Carlson

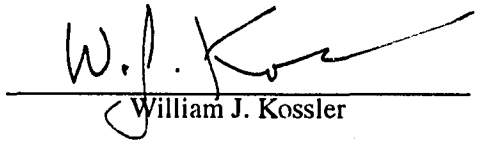

William J. Kossler

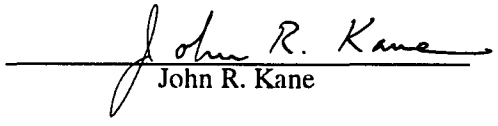

John R. Kane

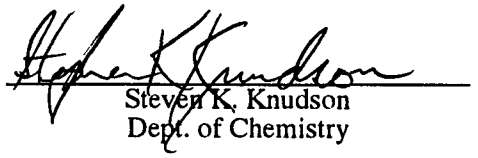

Steven K. Knudson
Dept. of Chemistry

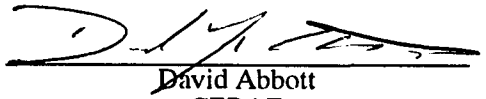

David Abbott
CEBAF

DEDICATION

To my parents, Arthur and Maria Viel, for their support and encouragement throughout my life, and for just believing in me.

To my grandparents, Tomaso and Ana Viel, and George and Maria Nita, for traveling so far from their homelands in search of a better life for their children and grandchildren. Their sacrifices allowed me to reach this goal.

TABLE OF CONTENTS

ACKNOWLEDGEMENTS

I would like to thank the many people who have contributed in numerous ways to make this dissertation possible:

Dr. Robert Siegel, my adviser, for his time and patience, for keeping me on the right path, and for showing me that doing physics well is hard, but much more satisfying than not.

Dr. Leopold Simons, for devising this experiment on the fly when all else failed, without his thorough knowledge of muon physics the run would not have proceeded so successfully.

Paola DeCecco, mia buon' amica, without her friendship, support, caring and laughter I would not have made it through my time in Europe or this run.

Dr. John Missimer, for those great lunches, his endless words of encouragement, and for being my guide post in a strange new place.

Dr. David Abbott, for keeping everything under control, making sure everything worked, always being available to help, his long hours on shift and his consistently positive attitude.

Dr. Franz Kottmann, for his always pleasant demeanor, his helpful comments, his willingness to listen to my sometime silly ideas, and his understanding of the problems at hand.

Dr. Dezso Horvath, for his hard work, keeping the peace, and his bad jokes.

Peter Hauser, for his time on shift, the Pilsner Urquels, and his good spirits.

Benny Bach, for well, being Benny.

The numerous technicians and staff at PSI, without whom the lab simple would not function, for their willingness to help, taking time from their normal duties, for patiently trying to understand my poor German, and for the friendships I had with them.

Paula Perry, Dianne Fannin, and Sylvia Stoust, for all their help, caring, and understanding through the years.

The members of my committee, for reading this dissertation.

ABSTRACT

Negative muons were brought to rest in a gas mixture of 30 torr CH_4 and 570 torr D_2, using the cyclotron trap at PSI. The muons formed muonic deuterium atoms which diffused through the mixture and transferred their muons to the carbon of the CH_4 molecules. A planar germanium detector and a silicon detector were used to observe x-rays from the initial muon cascade in the deuterium, and from subsequent cascade in the muonic carbon after transfer. A transfer rate of $(4.5 \pm 1.8) \times 10^{10}$ /sec was found which agrees well with a previous result measured at 50 bar of $(5.1 \pm 1.0) \times 10^{10}$ /sec. Transfer was found to occur predominantly to the n=4 state in μC. The initial angular momentum state distribution in the μC was constructed using the cascade program of V. Markushin, and found to be consistent with any combination of two possible initial distributions (I 0.252 (4s) + 0.409 (4f) + 0.339 (4p)) and (II 0.284 (4d) + 0.377 (4f) + 0.339 (4p)). The transfer theories of Gershtein and that of Holtzwarth and Pfeifer both agree well with the measured transfer rate and initial energy state, but not with the initial angular momentum distributions. The 2S population in μC was also determined to lie between 5% and 11%, which is higher than the 3% population in direct capture.

Muon Transfer from Muonic Deuterium to Carbon

I
INTRODUCTION

The properties of the muon are similar to those of the electron. A muon is a lepton, classified in the second generation of fundamental particles. It occupies the same position in its generation as the electron does in the first generation. The main differences are its mass, which is ≈200 times heavier, and its lifetime of ≈2.2 μsec, while the electron is a stable particle.

Like all leptons, the muon interacts by the weak interaction. For example,

$$\mu^- \rightarrow e^- + \nu_\mu + \overline{\nu}_e. \tag{1.1}$$

The muon can therefore be used to study the weak force by observing the muon interacting with other particles, such as hadrons. An example of this is proton absorption of a negative muon,

$$\mu^- + p \rightarrow n + \nu_\mu, \tag{1.2}$$

which permits the measurement of the hadronic form factors of the weak interaction.

Muons were first observed in the cosmic rays raining down from the upper atmosphere. However, the low flux of muons from the atmosphere does not make for an effective source for doing muonic interaction experiments. In practice muons are created for experiments from the decay of pions produced by strong interactions by particle accelerators using the reaction,

$$\pi^- \rightarrow \mu^- + \overline{\nu}_\mu. \tag{1.3}$$

This provides a beam of muons with a low momentum spread that can be directed to experimental areas in a controlled fashion.

Initially, it might be assumed that interactions can be observed in the scattering of muons from target nuclei as is done with other particles such as protons or deuterons. Muon scattering, however, is dominated by the electromagnetic interaction, since scattering does not provide much time for the weak interaction to have a large effect. Therefore, the negative muons are instead allowed to slow and capture on a target nucleus to form a bound state, customarily referred to as a muonic atom.

Generally, muonic atoms have only one bound muon and few or no bound electrons. Therefore, the muonic atom has a "hydrogenic" like muon-atomic structure. The time available for a weak interaction to occur in a muonic-atom is determined predominantly by the overlap of the muon state with the nucleus and the lifetime of the muon.

If muonic atoms are to be used as systems to study the weak or other interaction their properties must first be determined. This has spawned several areas of research on muonic atoms to study properties such as: μ^- capture, muon cascade down the μ-atomic levels, diffusion of μ-atoms through gases, scattering of μ-atoms from other atoms, formation of muonic molecules, etc. Another property is that of transfer of the muon from hydrogen, or one of its isotopes, to a nucleus of higher charge Z. Here, we study the transfer of muons from deuterium to carbon,

$$\mu d + C \rightarrow \mu C + d \tag{1.4}$$

In mixtures of deuterium (or other Z=1) and some other element of Z>1, transfer of the muon can occur from the initial μd to the higher Z element. Work to explore this possibility began experimentally with Schiff[1] by looking for muon transfer to neon in a hydrogen bubble chamber. The purpose was to study the effect of contaminants on muonic atomic processes in hydrogen, and to explore the possibility of using transfer to do other muonic experiments. Many other experiments have followed, using both liquid and gaseous hydrogen (and isotopes) mixtures. Most of these have concentrated on transfer to the noble gases, neon, argon, krypton and xenon[2-5] to eliminate the possibility

of any molecular effects in muonic atomic interactions. Results from these experiments, for argon in particular, have been conflicting and only recently have consistent values for the transfer rates been obtained[5]. Tests of theoretical rates of muon-atomic cascade and transfer can also be made using the mono-atomic elements, with the hope of then being able to calculate transfer to molecules and surfaces.

The possibility of making muon catalyzed fusion (μCF) a practical source of energy is also a motivation for studying transfer. Knowledge of the transfer processes and other complicated reactions of muons in mixtures of isotopes of hydrogen and helium are require if accurate models of the fusion process are to be constructed. To this end, experiments to measure muon transfer between the isotopes of hydrogen[6] and from these isotopes to helium[5] have been performed.

More recent work has looked at muon transfer to SO_2 from hydrogen[7], which is of interest because of the unexpected time dependence of the transfer rate. Unlike the transfer rate of muonic oxygen, which shows the expected exponential decay in time that was observed in all previous transfer experiments, the sulfur transfer rate shows an initial rise with time before it to changes to the decay shape. No consistent explanation has been found for this phenomenon. Further experiments are being performed on this mixture, and on hydrogen plus methane at high pressure to see if a similar effect is observed for carbon. All previous transfer experiments have been, and continue to be, done with high pressure targets of about 10 -50 atm, which is needed to stop the muon beam effectively. The high pressures also account for the high statistics of the data[7], since essentially the entire muon beam is stopped in the target making availible the maximum number of muon for transfer reactions.

In the work reported here, muon transfer from deuterium to carbon was observed in mixtures of deuterium plus methane at pressures below one bar. Transfer at such low pressures was of interest because of the possibility of using the mechanism in parity violation experiments and to extend the range of transfer observations to the low pressure

region. Working at these low pressures entailed many difficulties, and required the use of a cyclotron trap[39] to stop the muon beam, and to enhance a low event rate. Even so, data of the quantity and quality of similar high pressure experiments[7] was not expected, but the possibility for interesting results justified the attempt.

II
THEORY

A. Introduction

A muon undergoes a number of processes in the target chamber enroute to the process of transfer. Initially the muon is an independent particle, which is injected into the target gas composed of deuterium with a small amount of methane, and has a high momentum compared to the orbital velocity of a deuterium electron. Then the muon slows to an energy where atomic capture occurs and becomes bound to a deuterium atom ejecting the electron from that deuterium atom in the process. Following capture the muonic deuterium system (μd) is an atom in a highly excited state ($n \approx 14$), which proceeds to de-excite by a combination of external Auger and cascade processes down to the ground state, where it is a neutral, small object with a mean kinetic energy of about 1 eV. The μd atom diffuses through the gas, colliding with neighboring atoms and losing energy until it is in thermal equilibrium with the gas. If the μd encounters a carbon atom in a methane molecule, it may transfer its muon to the carbon nucleus. Transfer can occur from the ground state of the μd, or possibly while the muon is still cascading in the μd atom, i.e. the μd is in an excited state. The resulting muonic carbon atom created by the transfer of the muon is in an excited state, and subsequently de excites by processes similar to those for the μd atom.

B. Slowing Down and Capture

The process of slowing down and capture begins when the muon passes through the scintillator (T_3) (See Fig.3-1) at the entrance of the cyclotron trap gas chamber which is described in section III. The scintillator material, and a succession of moderators

reduce the muon momentum from ~25 MeV/c to a momentum optimal for the target gas and pressure (determined emperically during setup). The muon then slows by colliding with gas molecules as it spirals through the gas in the magnetic field of the trap until it is captured by a deuteron to form a μd atom. The fraction of muons captured by carbon atoms is small because methane comprises only 5% of the mixture.

Data from muonic x-ray studies can provide information on the time it takes the muon to capture on an atom and the x-ray yields of the cascade, but provides no direct information on the mechanism of the slowing down and the capture processes. For this reason theoretical models of slowing down and capture are important, and much effort using a variety of techniques has gone into developing them[11-14].

Three energy regions are involved in the slowing down and capture processes. The initial slowing process of the muon is governed by the standard formula for particles passing through matter, the Bethe-Bloch Eq[8]:

$$-\frac{dE}{dx} = \frac{4\pi z^2 e^4}{m_e v^2}\left\{\ln\frac{2m_e v^2}{I\left[1-\left(v/c\right)^2\right]} - \left(\frac{v}{c}\right)^2\right\} \qquad (2.1)$$

A more elaborate version of this equation which includes higher order effects is presented by Janni[9]. Use of the Bethe-Bloch equation is valid until the muon slows to the second energy region, with a momentum of about 3 MeV/c (~50KeV), where the energy loss becomes proportional to $\sqrt{E}$, instead of the $1/E$ of the above formula[10].

The third region includes kinetic energies below ~2.8 KeV. There the muon velocity drops below that of the electron in the ground state of the hydrogen atom, which is $v_\mu = \alpha c$. In this region many models of slowing and capture have been constructed. The early ones treated the moderator as an electron gas[11]; others used an adiabatic approximation[12]. More recent models make use of a diabatic approach[13] and of a classical trajectory muon scattering monte-carlo simulation[14]. Most of the models predict that capture will take place in approximately the n=14 state with a nearly

statistical distribution of angular momentum states, *lm*, and although the capture takes place on a molecule, it is expected that the molecule will break up from the energy imparted during the capture, leaving a single μd atom.

C. Cascade in Muonic Deuterium

From the initial high (≈n=14) state the muon cascades down to the ground state by a succession of Auger and radiative transitions. The cascade in deuterium (or any Z=1) is unique in that there are no bound electrons so the resulting μd atom is electrically neutral. This allows it to pass easily through neighboring atoms, allowing several reactions to occur during the cascade process.

There is at present a standard cascade model[15] which has resulted from a merging of previous calculations. The basic cascade processes are tabulated in Table 2-1.

The E1 radiative transition rate is given by:

$$\Gamma_{if}^{\gamma} = \frac{4}{3}\alpha R_{if}^{2}\omega^{3} \qquad (2.2)$$

Table 2-1 Cascade Processes used in the Standard Cascade Model

Process	Dependence on the Collision Energy
Radiative de-excitation $(\mu p)_i$ ---> $(\mu p)_f + \gamma$	none
External Auger effect $(\mu p)_i + H_2$ ---> $(\mu p)_f + e^- + H_2^+$	weak
Chemical de-excitation $(\mu p)_i + H_2$ ---> $(\mu p)_f + H + H$	?
Stark mixing $(\mu p)_{nl} + H_2$ ---> $(\mu p)_{nl'} + H_2$	moderate
Coulomb collision $(\mu p)_i + p$ ---> $(\mu p)_f + p$	strong

where R_{if} is the dipole matrix element and $\omega_{if}=E_i-E_f$ is the energy difference of final and initial states. The initial statistical population of the angular momentum states causes a predominantly circular cascade of $\Delta n=1$ transitions. The radiative transition rate therefore, decreases rapidly with increasing initial state n. All the other de excitation processes occur through collisions, therefore their rates depend on the number density N_e, of electrons available from neighboring molecules.

The ratio of the Auger rate to the radiative rate is:

$$\frac{\Gamma_{if}^{e}}{\Gamma_{if}^{\gamma}} = \beta(\mathrm{E1}) N_e \pi a_o^3 \qquad (2.3)$$

where

$$\beta(\mathrm{E1}) = 2\alpha\left(Z_{eff}\alpha\right)^3 \left(\frac{2\omega^2 + 4m_e^2}{2\omega_{if}^2}\right)\left(1+2\frac{m_e}{\omega_{if}}\right)^{\frac{1}{2}} \frac{m_e}{\omega_{if}} \qquad (2.4)$$

Here a_o is the electron Bohr radius and $Z_{eff} = Z\text{-}1$. From this it is seen that the Auger transitions are more important for smaller transition energies ω_{if}, therefore the radiative rates will exceed Auger rates only for the transitions from lower n states. At one bar of H_2 this occurs below about n=5.

Stark mixing is significant in the cascade because the neutral μd can experience a strong electric field close to neighboring nuclei. The electric field due to the nucleus is approximated as constant, which is calculated at the electronic Bohr radius a_o, $E = \alpha^{1/2} a_o^{-2}$, using mesic-atomic units: $h=m_\mu=e=1$. The Stark mixing rate ω_{st} is then

$$\omega_{st} = \left\langle \mathrm{nl}\left| \alpha^{1/2}\, \vec{r}\, E \right| \mathrm{n,l-1} \right\rangle = \alpha a_o^{-2} \langle \mathrm{nl}|r|\mathrm{n,l\text{-}1}\rangle = \mathrm{n}\left(\mathrm{n}^2 - 1^2\right)^{1/2} \mathrm{x}\ 2\mathrm{x}10^{14}\ \mathrm{sec}^{-1} \qquad (2.5)$$

If this is compared to the mean rate of collisions, which is $\omega_{col} \sim v/a_o \sim 1.0x10^{14}$, with $v \sim 1.0x10^6$ for an ~1 eV μd[28] and $a_o \sim 10^{-8}$ cm, Stark mixing is found to be faster and will therefore be the dominant rate in the cascade, until the $n \sim 3$ state is reached. For levels where Stark mixing dominates, its effect is to produce a statistical population of the angular momentum L values at each energy level *n*, during the cascade. In practice this means that any initial angular momentum value L may be chosen to start a cascade calculation, since L will be mixed statistically at the next level.

Cascade calculations were done by V. Markushin[22] for the two pure deuterium conditions in this experiment, 350 and 697 torr, using his code based on the above model. Table 2-2 shows the resulting x-ray yields for the K-series.

The time required for the cascade has been measured[16] for very low pressure hydrogen gas and found to be ~ 200 ns at 0.25 torr. An estimate of a few nanoseconds for the cascade at 94 mbar was made by J. Kraiman[17] and will be shorter for the higher pressures used in this work.

Table 2-2 Cascade in μd following capture for 350 and 697 torr D_2 using the Standard Cascade Model.

X-Ray Transition	Total Yield	
	350 torr Target Pressure	697 torr
$K\alpha$	0.504	0.528
$K\beta$	0.188	0.144
$K\gamma$	0.200	0.169
$K\delta$	0.0754	0.100
K_{tot}	0.999	1.000

D. Diffusion

At the end of the cascade process the μd atom is in its ground state, and the size of the atom is ~200 times smaller than an electronic hydrogen atom. The μd also has been found to have an initial kinetic energy distribution with mean energy much greater then that of the room temperature gas[17]. It diffuses through the gas by colliding with neighboring molecules of deuterium and methane.

Experiments[17] conducted at PSI have yielded most of the information on the diffusion process. Results from analysis of this experiment indicate an empirical fit the the initial energy distribution is a truncated power law distribution of the form E^{α} with a mean energy of ≈1.0 eV[28], where $\alpha \approx 0.5$, the truncation is at 40 eV. The important results from this experiment for the interpretation of the transfer rate, include the mean free path Λ and the average time for the μd velocity to be thermalized. From the monte-carlo simulation of the diffusion experiment, Λ is calculated to be about 0.1 cm for the conditions of the present experiment and the mean number of collisions until thermalization is about eight. The mean time to thermalization (also found from the monte-carlo) for these conditions is therefore expected to be a few hundred nanoseconds[28].

The diffusion continues as long as the μd exists but there are some processes that can destroy the μd[18]. First, the muon can decay, with a rate of $(4.55135 \pm 0.00014) \times 10^5$ sec^{-1}. The muon can undergo nuclear absorption in the reaction $\mu^- + d \rightarrow n + n + \nu_\mu$, with a rate of 445 ± 60 sec^{-1}. The μd can form a dμd molecule in a collision with another D_2, $\mu d + d \rightarrow d\mu d$ with a rate of $(23.4 \pm 0.17) \times 10^5$ sec^{-1} for liquid D_2 density, leading to a rate of $\sim 10^3$ sec^{-1} for the present experiment. Lastly the muon can transfer to an impurity of higher Z, which is the focus of the present experiment.

E. Transfer from the Ground State

During the diffusion process the μd may encounter a methane molecule rather than a deuterium molecule. Since the mixture contains about 5% methane there is about a 5% probability for this type of encounter per collision. In the collision the muon may transfer from the deuterium to the carbon, due to its greater charge and therefore greater binding energy.

Although the carbon atom is bound in a methane molecule, which has four hydrogen atoms arranged in a tetrahedral structure, it is thought that these hydrogen atoms and the molecular structure have little effect on the transfer process. This is because the μd is so small on the scale of a normal atom that when it passes through a molecule it experiences only a small polarization force from the atoms in the molecule. But, if the μd approaches the carbon nucleus to a distance at which transfer can take place (this will later be shown to be about 35 fermi), the major force on the μd will be due to the carbon nucleus and the polarization force of other atoms in the molecule will be insignificantly small. Also, if the μd first encounters the proton it may scatter from it, but in doing so the muon is probably not affected by the carbon. Finally, it has been observed in experiments[35] of muons stopping in pure carbon and in hydrocarbons, that both conditions produce the same yields of μC x-rays indicating that all muons eventually are captured by the carbon atom.

E. 1. Gershtein Calculation of Transfer

Gershtein[19] has made a calculation for muon transfer from hydrogen to carbon and oxygen. An energy level scheme (See Fig. 2-1) shows that transfer can only occur to a level $n \leq Z$ by energy conservation, which for carbon is n=6. The kinetic energy of the collision is insignificant compared to the binding energies, and is ignored in this calculation.

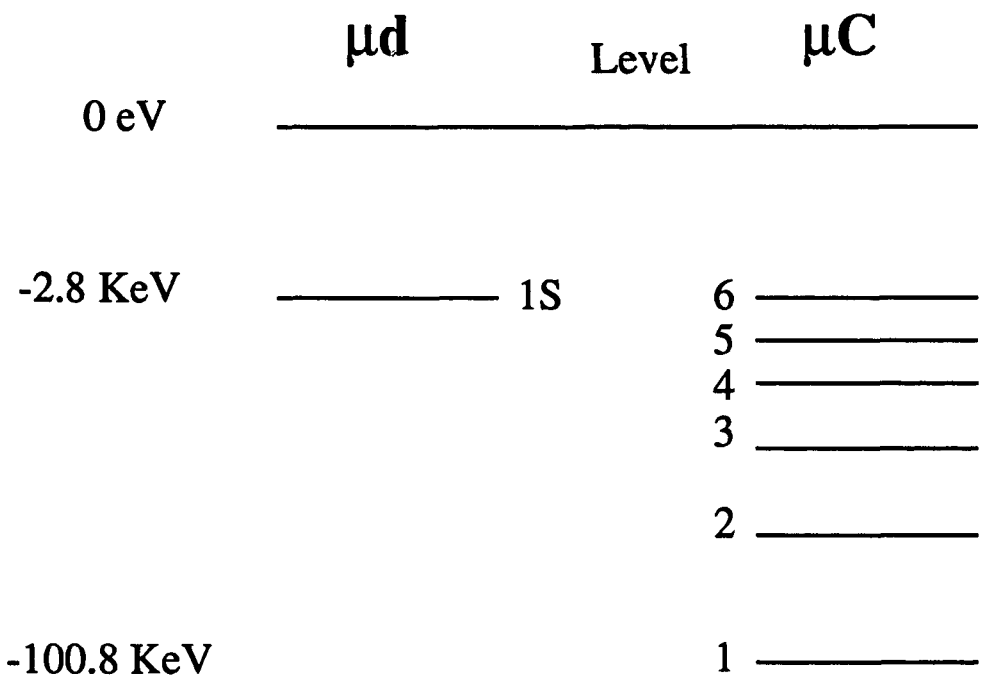

Fig. 2-1 Energy Level Diagram for μd and μC

The hamiltonian of the muon, carbon, proton(deuteron) system is (still using mesic-atomic units: $\hbar=m_\mu=e=1$):

$$H=-\frac{1}{2M_1}\Delta_{\mathbf{R}_1}-\frac{1}{2M_2}\Delta_{\mathbf{R}_2}-\frac{1}{2}\Delta_{\mathbf{r}}-\frac{1}{r_1}-\frac{Z}{r_2}+\frac{Z}{R} \qquad (2.6)$$

where $\boldsymbol{R}_1$, $\boldsymbol{R}_2$ and $\boldsymbol{r}$ are the coordinates of the proton or deuteron, Z nucleus and muon respectively, $r_1=|\boldsymbol{r}-\boldsymbol{R}_1|$, $r_2=|\boldsymbol{r}-\boldsymbol{R}_2|$, $R=|\boldsymbol{R}_2-\boldsymbol{R}_1|$ and $\Delta\equiv\nabla^2$ operator. The system is described in the Born-Oppenheimer approximation -- also called the adiabatic approximation -- in which it is assumed that the speed of the proton with respect to the Z-nucleus is small compared to that of the muon. A solution of the form,

$$\Psi=\Phi_0(\mathbf{R})\,\varphi_0(r_1)+\sum_i\Phi_i(\mathbf{R})\,\varphi_i^Z(r_2) \qquad (2.7)$$

is sought where $\varphi_0(r_1)$ is the ground state wave function of the muon in the μp subsystem and $\varphi_i^Z(r_2)$ is the muon wave function in the μZ system. The functions Φ_0 and Φ_i are the wave functions of the proton and nucleus in the equivalent two body reduced mass problem with the muon bound to the proton or the Z-nucleus, respectively. The muon is assumed to "belong" to either the Z-nucleus or the proton at all times. This is reasonable for $R >> 1$ (muonic Bohr radius) at which transfer is shown to take place. Since the wave functions, φ, are for hydrogenic atoms they must satisfy the following Schrödinger Eqs.:

$$\left(-\frac{1}{2}\Delta_r - \frac{1}{r_1}\right)\varphi_0 = -\frac{1}{2}\varphi_0$$
$$\left(-\frac{1}{2}\Delta_r - \frac{1}{r_2}\right)\varphi_i^Z = -\frac{Z^2}{2n^2}\varphi_i^Z \qquad (2.8)$$

Integrating the known wave functions from the Schrödinger Eq. constructed from the hamiltonian Eq. 2.6, leaves the following equations to be solved for the two body scattering case,

$$\left(-\frac{1}{2M_1}\Delta_R - E + E_0 + V_{00}(R)\right)\Phi_0 = \sum_i V_{0i}\Phi_i$$
$$\left(-\frac{1}{2M_1}\Delta_R - E + E_i + V_{ii}(R)\right)\Phi_i = \sum_i V_{i0}\Phi_0 \qquad (2.9)$$

where $M=M_1M_2/(M_1 + M_2)$ is the reduced mass of the p - Z system, E_0 and E_i are the binding energies of the individual muonic atoms of the proton and Z-nucleus respectively and the following potentials are

$$
\begin{aligned}
V_{00} &= Z\left(1/R - \left\langle 1/r_2 \right\rangle_{00}\right) \\
V_{ii} &= \left(Z/R - \left\langle 1/r_1 \right\rangle_{ii}\right) \\
V_{0i} &= \left(\left\langle 1/r_1 \right\rangle_{0i} - \left\langle 1/r_1 \right\rangle_{ii} S\right) \\
V_{i0} &= Z\left(\left\langle 1/r_2 \right\rangle_{i0} - \left\langle 1/r_2 \right\rangle_{00} S\right)
\end{aligned}
\qquad (2.10)
$$

where

$$
\begin{aligned}
S &= \int \varphi_0 \varphi_i^Z \, d\tau \\
\left\langle 1/r_1 \right\rangle_{0i} &= \int \varphi_0 r_1^{-1} \varphi_i^Z \, d\tau \text{ , etc.}
\end{aligned}
\qquad (2.11)
$$

Gershtein makes approximations which eliminate terms of $O(1/R^3)$ and higher when they are not the leading terms in an effect. This leads to energies of

$$
\begin{aligned}
E_0 &= -\frac{1}{2}\frac{M_1}{M_1+1} \approx -\frac{1}{2}\left(1 - \frac{1}{M_1}\right) \\
E_i &\approx -\frac{Z^2}{2n^2}\left(1 - \frac{1}{M_2}\right)
\end{aligned}
\qquad (2.12)
$$

An incoming plane wave and outgoing spherical wave for the μp + Z system is

$$
\Phi_0 \approx \frac{1}{\sqrt{v}} \sum_i i^l (2l+1) e^{i\alpha_l} P_l(\cos\theta) \left\{ \sin\left(kR - \frac{\pi l}{2} + \alpha_l\right) + \gamma_l \exp i\left(kR - \frac{\pi l}{2} + \alpha_l\right) \right\} \frac{1}{kR}
\qquad (2.13)
$$

where α_l are the phase shifts for the radial part of the wave function, γ_l are the coefficients of the scattered μp, which leads to the scattered waves for the p + μZ system,

$$\Phi_i \approx \frac{1}{\sqrt{v_i}} \frac{e^{ik_i R}}{k_i R} \sum_i i^l (2l+1) q_l^i P_l(\cos\theta) \tag{2.14}$$

where the q_i are the coefficients for the scattered waves. This finally leads to the transfer cross section of[34]

$$\sigma_i = \frac{4\pi}{k^2} \sum_l (2l+1) \left| q_l^i \right|^2 \tag{2.15}$$

To determine this cross section the method of crossing molecular terms is used[20]. The total energy E for the μp + Z system is approximately $E_p(R) = E_0 + V_{00}$ and for the p + μZ system. is $E_Z(R) = E_i + V_{ii}$ where

$$V_{00} \approx O\left(e^{-R}\right), \qquad R \to \infty \tag{2.16}$$

$$V_{ii} \approx \frac{Z-1}{R} + \frac{3}{2} \frac{n\left(n_1 + n_2\right)}{ZR^2} \tag{2.17}$$

Here n_1 and n_2 are the parabolic quantum numbers, and $n = n_1 + n_2 + 1$ is the principle spherical quantum number. Equating the total energies $E_p = E_Z$, we get the distance of crossing, R_0, and hence the distance where transfer occurs.

$$-\frac{1}{2} \frac{M_1}{1+M_1} = -\frac{Z^2}{2n^2} \frac{M_2}{1+M_2} + \frac{Z-1}{R} + \frac{3}{2} \frac{n\left(n_1 + n_2\right)}{ZR^2} \tag{2.18}$$

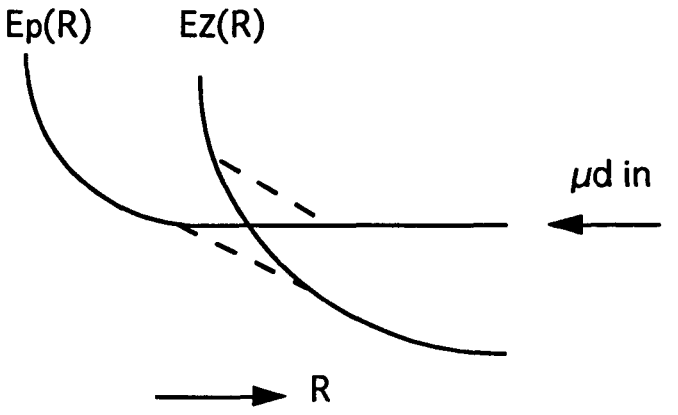

Fig 2-2a - One total energy curve crossing

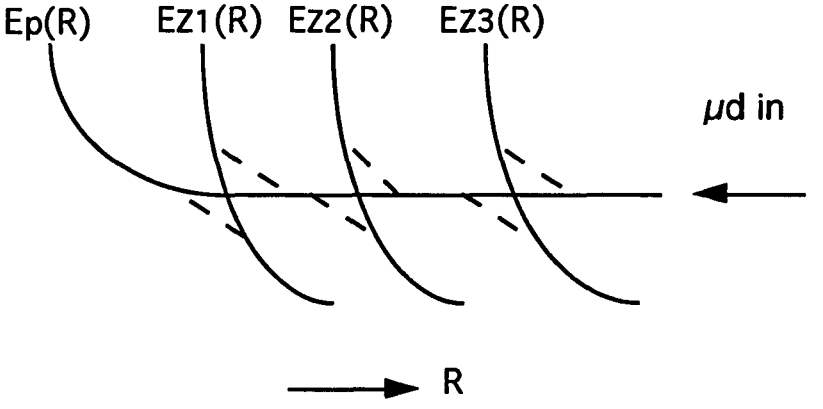

Fig. 2-2b - Total energy curves for crossing

At the separation R_0, the energy of the system is independent of whether the muon is associated with the proton or the Z-nucleus. Therefore, the incoming ($\mu p + Z$) state can possibly change to a ($\mu Z + p$) state. This is illustrated schematically in Fig. 2-2a.

In Fig. 2-2, the μp comes in from the right on the potential curve $E_p(R)$, and as it comes closer to the Z-nucleus it crosses the potential curve $E_Z(R)$ at R_0. The muon can either continue with the proton, staying on the initial curve or there is a probability that the muon will transfer to the Z-nucleus, in which case the system will follow the $E_Z(R)$

curve. It is clear that on the return path the system will again pass through the crossing region, so that if the muon did not transfer on the incoming path it can possibly do so on the return. In principle several $E_Z(R)$ curves, each representing a principle quantum number n, are crossed so there is a probability of transferring to each of these that combined give the total transfer probability (See Fig 2-2b).

The cross section and hence the rate is determined from

$$\left|q_l^i\right|^2 = \left(1-e^{-\delta_i}\right)e^{-\delta_i}\sin\tau_i \qquad (2.19)$$

where τ_i is the scattering angle and the phases are

$$\delta_i = \left\{2\pi\frac{\left|V_{i0}\right|^2}{v_0}\left|F^i - F^0\right|\right\}, R = R_0 \qquad (2.20)$$

with $F^i = -dV_{ii}/dR$ and $F^0 = -dV_{00}/dR$. The relative velocity (v_0) of the nuclei at crossing point R_0 is given by

$$v_0 = \left[\frac{2}{M}\left(E - E_0 + \frac{9}{4}\frac{Z^2}{R_0^4} - \frac{\left(l-1/2\right)^2}{2MR_0^2}\right)\right]^{1/2} \qquad (2.21)$$

The scattering angle is then averaged over to give $\sin^2\tau_i = 1/2$.

The probability of transfer, from one curve to the other [20] for this method is given for a single crossing by,

$$P = e^{-\delta} \qquad (2.22)$$

Since each curve is crossed twice the total probability for transfer to a particular μZ state is

$$\omega = 2e^{-\delta}\left(1-e^{-\delta}\right) \qquad (2.23)$$

This is generalized by Gershtein to several crossings, and a total probability for each final state ω_i is computed.

The transfer radii, phases and probabilities are given in Table 2-3 for the case of carbon, Z=6, from which it is seen that about 95% of the transfer should go into the n=4 state of μ-carbon. The μC states are described by the parabolic quantum numbers n_1, n_2, m or their principal $n=n_1+n_2+1$.

The parabolic states give the initial angular momentum distribution when they are converted to spherical coordinates, which is done for the two n=4 states that make up the majority of the transfer, and for the combination of these states calculated from their probabilities (See Table 2-4).

Table 2-3 Transfer parameters of μd on Carbon for Gershtein calculation.

State		R_0	δ_i	ω_i
	n_1=0, n_2=2	2.93	0.66	0.016
n=3	n_1=1, n_2=1	3.26	0.08	<0.01
	n_1=2, n_2=0	3.54	4×10^{-5}	<0.01
	n_1=0, n_2=3	6.86	3.24	0.05
n=4	n_1=1, n_2=2	7.31	0.08	0.14
	n_1=2, n_2=1	7.71	4×10^{-4}	$<10^{-2}$
	n_1=3, n_2=0	8.08	4×10^{-7}	$<10^{-2}$
	n_1=0, n_2=4	17.89	7×10^{-4}	
	n_1=1, n_2=3	18.43	4×10^{-6}	
n=5	n_1=2, n_2=2	18.95	4×10^{-6}	$<10^{-2}$
	n_1=3, n_2=1	19.43	10^{-7}	
	n_1=4, n_2=0	19.90	2×10^{-9}	

Table 2-4 Initial Population of μC after transfer, Gershtein Calculation, in Spherical coordinates, n=4 state.

Spherical States	Parabolic States (n_1, n_2, m)		Predicted Combination
	(210)	(300)	74% (210) + 26% (300)
4s	.245	.249	.246
4p	.0482	.448	.153
4d	.246	.254	.248
4f	.461	.0487	.352

Although the calculation was done for hydrogen the results for deuterium should be similar since the reduced mass is only a few percent different. Lastly an estimate is made for the transfer rate. Under the conditions for a liquid hydrogen bubble chamber ($N=3.5\times10^{22}$ / cm^3) the rate is predicted to be approximately $\lambda_C = 2.8\times10^{10}$ /sec and twice this for deuterium.

E. 2. Holzwarth and Pfeiffer Calculation of Transfer

A calculation of transfer that is very similar to the Gershtein calculation was done by Holzwarth and Pfeiffer[41]. This calculation mainly differs by not including the wave functions of the two nuclei in the wave function approximation, and not including the kinetic energy terms for the nuclei in the Hamiltonian. This is a reasonable thing to do since the motion of the two nuclei are calculated classically, even in the Gershtein model. The phases δ_i are also calculated somewhat differently. The result of this calculation is that the muon transfers to the n=4 state of carbon as in the Gershtein calculation but the angular momentum distribution is different, with all of the transfer to the (300) state, where the values are (n_2, n_1, m), the parabolic quantum numbers. This distribution, shown in the second column of Table 2-4, is one of the two allowed in the Gershtein calculation but interestingly is not the larger of the two. The different initial angular

momentum distribution of course leads to a different cascade and x-ray spectrum from that of the Gershtein distribution.

F. Transfer from Excited States

In addition to transfer from the ground state of the μp system, transfer may also take place during the cascade process. Collisions with methane molecules can also occur during the de-excitation process. Because methane makes up 5% of the gas, there is a significant probability of this encounter occuring. During one of these collisions the muon may transfer while it is still in an excited μd state. This process has been observed for the case of pions[21], for which transfer can only occur from highly excited states of pionic hydrogen due to the rapid nuclear absorption of the pions from lower π^-p states. The absorption times for pions leave little time for transfer from these lower level states. Excited state transfer changes the muon cascade of the μd atom formation, and is expected to show up as a difference in the yields of the μd x-rays.

G. Cascade in Muonic Carbon

Two types of cascade in muonic carbon were studied in this experiment. In the first, muons are brought to a stop in pure methane, which results in direct capture of the muon on the carbon in a manner similar to the capture on deuterium. The muon is therefore captured in a high n state with a statistically populated angular momentum distribution. The resulting cascade will be dominated by the circular transitions, since a large fraction of the muons start out at high L-values and therefore continue down the cascade at the outer edge of the level scheme. The direct capture is thought to eject all the bound electrons early in the cascade[43], so by the time the muon has reached the n=4 state the only electrons accessible are those involved in external Auger transitions from neighboring molecules.

The circular cascade is the major difference between deuterium (or other Z=1) and the higher Z muonic atoms. Since the latter are not neutral, they cannot move easily through or deeply into the electron clouds of neighboring molecules. The amount of Stark mixing that occurs is therefore insignificant, so few low L states are populated during the cascade.

The second type of cascade in carbon occurs after transfer, when the muon finds itself in an excited state, that from the Gershtein theory, will be mostly n=4 with an angular momentum distribution as specified in Table 2-4. Since this angular momentum distribution is different from that of the circular cascade at the n =4 level, the resulting spectrum will show a significant amount of non-circular transition events which are not seen in the direct capture spectrum. Another difference from direct capture is that the carbon atom still has electrons in its shell after the transfer, because no internal Auger process has occured during transfer to eject them.

Of the six carbon electrons, only the two 1S-state electrons overlap the nucleus enough to affect the cascade following transfer. The muon is much closer to the nucleus in the n=4 state then the electrons, so the higher level electron wave functions have little overlap. The possible Auger transitions which eject the 1S electrons during the muonic cascade leave the μC in the n=2 state, which has a lifetime (See Eq. 2.2) of 5 x 10^{-12} sec. This is more then two orders of magnitude faster than the refilling time of the 1S state from the 2P electrons. The muonic 3-1 radiative transition is also about an order of magnitude faster then the electronic 2-1 transition, so even if only one electron is ejected the refilling rate is still not fast enough to alter the muonic cascade. Including only the two 1S electrons in the calculation therefore appears to be a good assumption in the calculation of cascade after transfer.

There was nonetheless some concern about the assumption of two K-shell electrons being in the carbon atom after transfer. Fortunately, in Landau and Lifshitz[34] the authors do two problems that are related to this assumption. The first (p. 150 #4) is a

calculation of the probability that a K-shell electron will be ejected after a beta decay of the nucleus. This is related to the transfer problem, since the muon transfer process lowers the effective charge Z by one, as with negative beta decay. The probability was calculated for the case of carbon to be 1.8%, small enough to be ignored in this analysis.

The second problem (p. 150 #5)[34] is a calculation of the alpha particle from a nuclear alpha decay ejecting a K-shell electron. This is related to the deuteron that is freed after transfer and passes near the nucleus in a similar fashion to the alpha particle. The probability for the deuteron to eject a K-shell electron was found to be $\approx 10^{-11}$, an insignificant effect. Both of these calculations support the assumption that two K-shell electrons are present after transfer.

Table 2-5 μC Cascade Yields after Transfer to n=4 states, Individual initial angular momentum states.

	Initial State before cascade			
Transition	4s	4p	4d	4f
2p-1s	.113	.374	.213	1.00
3p-1s	.768	0	.681	0
4p-1s	0	.563	0	0
3s-2p	0	.264	0	0
3p-2s	.100	0	.089	0
3d-2p	0	.0309	0	.840
4s-2p	.0993	0	0	0
4p-2s	0	.0804	0	0
4d-2p	0	0	.186	0
4s-3p	.0726	0	0	0
4p-3s	0	.0278	0	0
4p-3d	0	.0034	0	0
4d-3p	0	0	.061	0
4f-3d	0	0	0	.086

A monte-carlo simulation was done by V. Markushin of the cascade in carbon following transfer. The first set started with 100% population in each of the four individual initial angular momentum states of the n=4 level, which are shown in Table 2-5. These results were combined into the two main n=4 parabolic states and finally into the Gershtein predicted initial state distribution[22] (See Table 2-6). All of these cascade simulations used the above assumptions about electron populations and internal Auger effect.

These tables also provide a prediction of the yield for the 2S state after transfer. Using the Gershtein initial angular momentum state population, Table 2-6, gives a 7.2%

Table 2-6 μC Cascade Yields after Transfer to n=4 state, Individual parabolic and Gershtein Initial Population states.

	Initial Parabolic states (n_1, n_2, m)		Initial Gershtein Predicted state
Transition	(210)	(300)	74% (210) + 26% (300)
2p-1s	.559	.286	.487
3p-1s	.351	.365	.355
4p-1s	.0277	.250	.0862
3s-2p	.0117	.118	.0397
3p-2s	.0478	.0492	.0482
3d-2p	.386	.0545	.299
4s-2p	.0207	.0247	.0218
4p-2s	.004	.0366	.0126
4d-2p	.0513	.0463	.0500
4s-3p	.0172	.0171	.0172
4p-3s	.0016	.0099	.0038
4p-3d	3×10^{-4}	.0012	5×10^{-4}
4d-3p	.0159	.0151	.0157
4f-3d	.0351	.0048	.0271

yield. This is somewhat higher than the predicted 2S yield for direct capture of about 3%.[16] The yields predicted from Gershtein's initial angular momentum population will be compared with the experimental results in section V.

The cascade for the initial angular dimension distribution of Holzwarth and Pfeiffer was calculated by F. Mulhauser for the case of muon transfer from deuterium to carbon[42] and is listed in Table 2-7. In principle the cascade is already given in Table 2-6 for the (300) state from the Markushin program, and a comparison to that of Mulhauser shows a significant discrepancy only for the 2-1 transition. This difference is due to the Markushin program not including a 2-1 transition is its scheme, because it was assumed the 2-1 radiative rate dominates all competitive rates. The cascade from Mulhauser was used to successfully fit the Lyman series from high pressure transfer data of deuterium and methane, so it will continue to be used for comparison in this analysis.

Table 2-7 μC Cascade Yields after Transfer to n=4 state, angular momentum distribution from Holtzwarth and Pfeiffer and cascade by F. Mulhauser.

Transition	Parabolic state (300)
2p-1s	.436
3p-1s	.350
4p-1s	.222
3s-2p	.124
3p-2s	.0458
3d-2p	.0498
4s-2p	.0178
4p-2s	.0316
4d-2p	.0367
4s-3p	.0127
4p-3s	.0100
4p-3d	.0011
4d-3p	.0125
4f-3d	.0031

III
EXPERIMENTAL METHOD

A. Accelerator and Beam

The experiment was conducted at the Paul Scherrer Institut in Villigen, Switzerland using the πE1 beam line of the Main Cyclotron. The cyclotron provides pulsed proton bunches at 50 MHz to a carbon target with a nominal current of 500 μA. Unfortunately during this run a beam current of 120 μA was typical due to problems in the Main Cyclotron ring. The low current limited the amount of data taken and perhaps more significantly caused a loss of signal to noise ratio in the data.

The proton-target collisions create pions, which pass down a drift tube where they decay into muons and electrons. The negative muons are selected, focused and guided down a beam line to the experimental area providing approximately 10^4 muons/sec. Most of the negative electrons resulting from muon decay in the beamline also come down the beam line with the muons, and it will be shown later that they greatly affect the experiment. The cyclotron trap is positioned at the end of the beam line in the πE1 area with its beam entrance channel flanged to the beam line.

B. Cyclotron Trap

Advances in physics and the ability to do new and novel experiments are often the result of a new technology or a new use of an old technology. Such is the case for this experiment. The Cyclotron Trap of Leo Simons is a new use of an old idea that makes it possible to do exotic atom experiments at low gas pressure with the present accelerator

technology. The Trap is an integral part of this experiment and so will be described in detail below.

The major problem in doing muonic atom experiments in low pressure gases is stopping the muon beam in the gas. The beams finite momentum spread causes the muons to stop over a distance in the gas that can be large compared to the size of the detectors used to observe the resulting muonic atoms. Even with the low momentum spread of modern accelerators stopping distances can still be large for very low pressure gases. In such a large spread of stopped muons the resulting muonic atoms are difficult to observe with a detector that is typically only a few square centimeters in size. The effective event rate as seen by the detectors decreases with decreasing gas pressure. Clearly the low event rate from such a setup would make most experiments unfeasible. Some solution is needed therefore required to cause the muons to stop in a smaller volume of gas, which would present a better source for the detectors to observe.

The Cyclotron Trap offers just such a solution. It basically acts as a cyclotron run backwards. The muon beam is injected into the outer edge of the magnet, it decelerates as it circulates moving progressively inward and stops at the center of the trap. The result is a small beam spot in front of the bore holes of the trap that is more easily observed by the detectors.

B. 1. Description of Trap

The cyclotron trap is a dipole magnet in the shape of a right cylinder with a "cyclotron" field in the gap. It is constructed with a yoke of galvanized soft iron with a radius of 315 mm and a gap of 150 mm between the pole faces (See Fig. 3-1). Through the axis of the poles (in the Z direction) are circular holes (boreholes) 100mm in diameter that lead into the gap from each end of the magnet. These provide access to the muon stop region for the detectors.. The distance from the center to the outer pole face is 380 mm.

The field is created by super conducting coils behind the pole faces, which are cooled with liquid helium and are surrounded by a liquid nitrogen jacket, the attached reservoirs need refilling about twice a day with the field turned on. The pole faces are connected by soft iron pillars which are just large enough to field saturate at the nominal operating field strength (about 1 Tesla). These pillars also obstruct the access to the central stop region and are a limitation to the type of setup that can be employed for experiments.

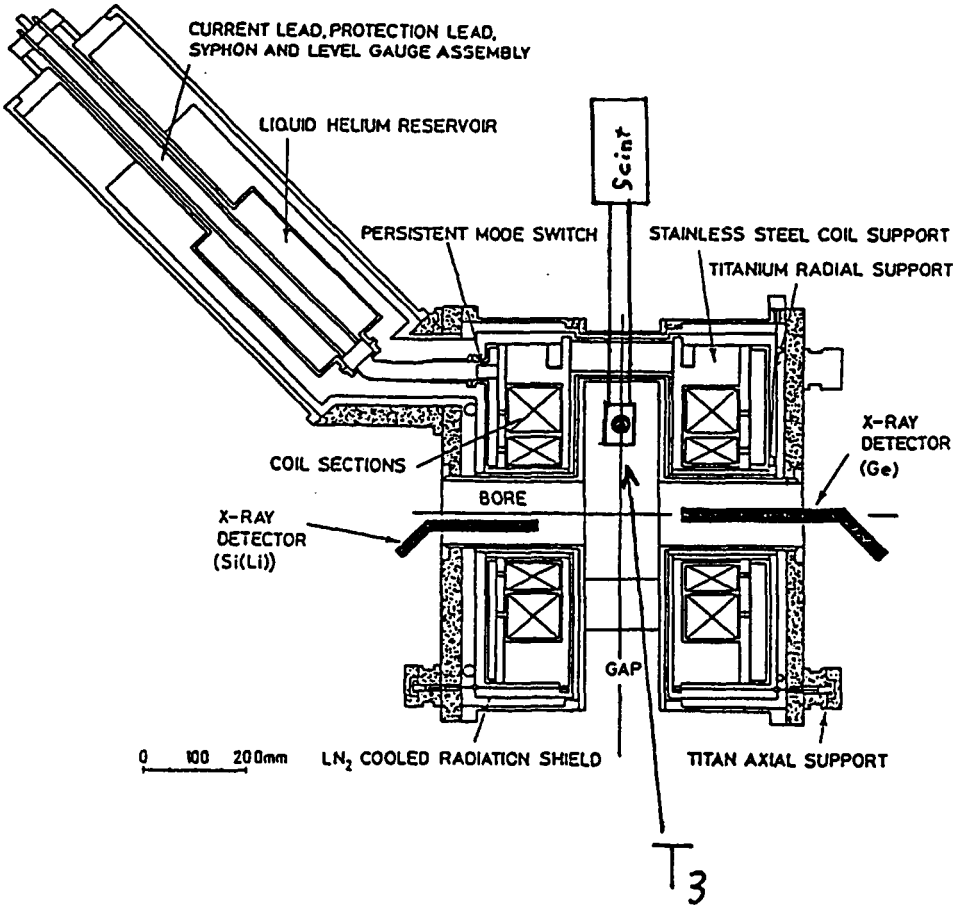

Figure 3-1 Cyclotron Trap with scintillator T_3.

A cylindrical gas chamber, constructed of aluminum and stainless steel, is placed between the pole faces and positioned concentric with the bore holes. Around the circumference of the chamber are windows that provide access for the incoming beam, the T_3 scintillator, vacuum, gas and other uses. Attached to one of the widows is the beam entrance channel to admit the muons to the chamber. The entrance channel has an iron shield that guides the beam from the beam pipe into the trap by blocking the magnetic field until the beam reaches the injection radius of about 11 cm (See next section). Separation of the trap from the beam line is done using a mylar window at the beginning of the entrance channel which can hold up to one atmosphere of pressure. A chamber window downstream of the entrance channel holds the T_3 scintillator, which is the beam counter for the data acquisition and signals the entrance of a muon into the chamber.

The whole trap assembly sits on a table that is adjustable in both height and attitude to a fraction of a millimeter using hydraulic lifts. This allows accurate attachment to the beam line and subsequent beam tuning. The detectors, electronics and anything else that must move with the trap are also mounted on this table.

B. 2. Theory of Operation

The paths of charged particles that move in a magnetic field curve due to the Lorentz force.

$$F_B = \frac{evB}{c} \tag{3.1}$$

In the radially symmetric field of the cyclotron trap this leads to circular orbits with the resulting force on the particle given by the equations of motion.

$$F_c = \frac{mv^2}{r} \tag{3.2}$$

Equating the two gives the equation of motion for the particle orbits.

$$p = mv = \frac{eBr}{c} \tag{3.3}$$

From this a new quantity is defined, the angular frequency of the orbits, ω, called the cyclotron frequency.

$$\omega = \frac{eB}{mc} \tag{3.4}$$

This is nearly constant in a typical cyclotron because the field falls off slowly with increasing radius and the mass is constant for non-relativistic particles. The decrease in the field strength at the circumference is mainly due to the bulging out of the field lines at the edge. Typically the field strength drops monotonically by a few percent from the center of the gap to its outer edge. This monotonic change is critical to the operation of the cyclotron by preventing particles from being trapped in orbits where the field change creates a potential minumum.

Stability and guidance of the beam (muons in this case) is the key factor in designing any accelerator (or decelerator). In a cyclotron there are two directions where stability must be maintained the radial and the axial (Z direction parallel to the dipole axis). It is convenient to define the field index

$$n = -\frac{dB}{dr}\frac{r}{B} \tag{3.5}$$

which is related to beam stability. A calculation of a perturbation of the muon orbit in the axial direction leads to the equation[23]

$$\ddot{z} + \omega^2 nz = 0 \tag{3.6}$$

where z=0 is the median plane where no radial component of the field exists and in which the equilibrium orbit lies. If $n > 0$ sinusoidal solutions are found. Hence, the beam

oscillates about the median plane. In the radial direction the equation of perturbed motion is

$$\ddot{x} + \omega^2(1-n)x = 0 \tag{3.7}$$

where x is the radial distance from the equilibrium radius. This also has sinusoidal solutions for the condition $n < 1$. The condition for stability in a cyclotron in both radial and axial directions therefore requires $0 \leq n \leq 1$, for which the beam will oscillate around the equilibrium orbit in what are called betatron oscillations.

The region of stability can be found by looking at the quantity Br, which is zero at the origin and increases monotonically toward the circumference. Near the edge of the magnet however, the field falls off more rapidly than the radius grows, so the function Br passes through a maximum close to the edge. Differentiating Br and substituting the relation 3.5 for n gives, $B\text{-}nB = 0$, so $n=1$ at the maximum of Br. The field index n, is zero at the origin from relation 3.5, therefore the region of stability is from the origin to the radius where Br is maximum. The maximum stable radius for the cyclotron trap is 143 mm with an initial maximum momentum[24] of 123 MeV/c.

The magnitude of the betatron oscillations contributes to the size of the final stop region in the gas, with the initial amplitude determined by the emittance of the incoming muon beam. Calculations[24] using a modified form of Liouville's theorem show that the radial width of the stop region is the same as the beam width at the injection point of the trap. However, the axial width of the stop region was calculated to be almost twice as large as the incoming beam width.

A second factor that increases the width of the final stop distribution is that axial betatron oscillations are intentionally excited to prevent multiple passes through scintilator T_3 by injecting the beam at an angle of 110 mRad. Unfortunately, if the beam is injected in the direction parallel to the median plane, orbits subsequent to the first one passing through the scintillator T_3 are still large enough in radius to pass through T_3

again and cause multiple counts of the muon. The injection at an angle causes the beam to miss the scintillator T_3 on orbits after the first pass, thus insuring that each muon entering the trap is counted only once.

The ultimate goal is to stop muons in the center of the trap. To do this the muons must loose energy while orbiting in the trap. This is accomplished by collisions with the target gas that fills the chamber or by plastic foils inserted in the median plane of the chamber. However, the muons must loose energy slowly through this process so that the change in orbits does not alter the position of the orbital center. The slow energy loss allows each orbit to be considered adiabatic, which allows the use of Liouville's theorem for calculation of the phase space as the muon travels toward the center. A larger energy loss per circulation would induce non-circular orbits and increase the stop distribution size. A gradual energy loss therefore is equivalent to stepping down a series of concentric equilibrium orbits to yield the smallest possible stop distribution at the center of the trap given the initial emittance of the beam.

C. Gas and Vacuum System

The gas system (See Fig. 3-2) consisted of a manifold connecting several gas cylinders. The manifold led to a precision needle valve which allowed accurate adjustment of gas pressure in the target chamber with use of a high precision pressure gauge connected just after the needle valve. The gas entered the chamber via the vacuum system, which was connected to one of the windows of the target chamber. The vacuum system consisted of a large tube from the target chamber to a turbo-molecular pump. A roughing pump was connected with a valve to the turbo-pump. Attached to the tube from the target chamber to the turbo-pump were a high accuracy vacuum gauge (accurate to 10^{-9} torr), the gas inlet, and a venting valve. A valve was also located in front of the turbo-pump to isolate it from the target chamber.

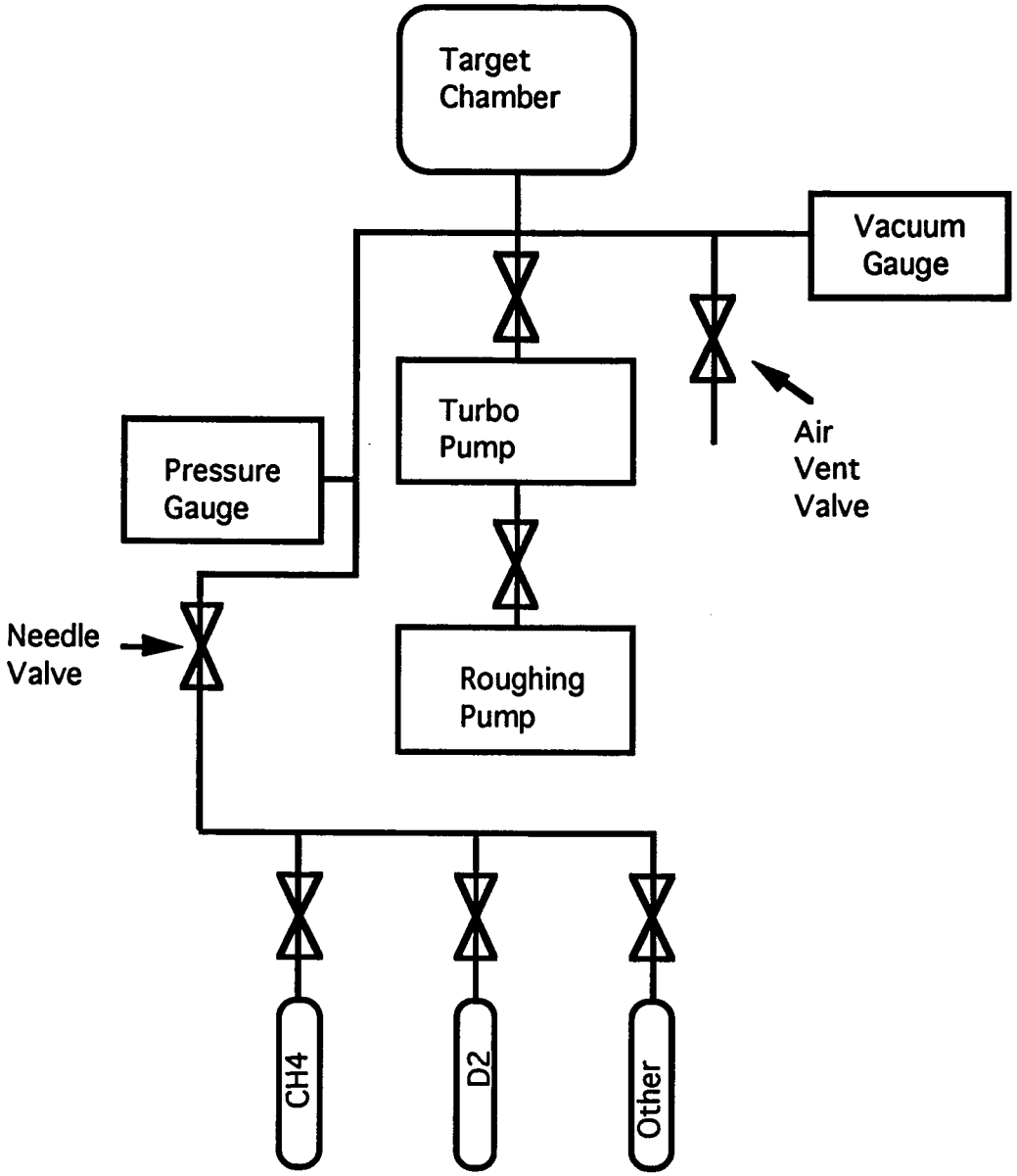

Fig. 3-2 Gas/Vacuum system

D. Detectors

Two detectors were used for observing μ atom x-rays. Both were placed in gas tight plastic sleeves that allowed them to be flanged to the gas chamber through the bore holes of the trap. The first, Silgard, was a silicon detector with two active regions positoned coaxially one inside the other. The two regions are referred to as inner and outer with active areas of $30mm^2$ and $200mm^2$ respectively. The inner area has a resolution of 267 eV at 6.4 KeV and 291 eV at 14.4 KeV. Both had a depletion layer of 6mm. Each active area is connected to an optical feedback preamp that provides both timing and energy pulses to the data acquisition system. The second detector, W&M, was an intrinsic planar germanium detector with an active area of $2000mm^2$ and an active depth of 13mm. The crystal is connected to a resistive feedback preamp and the assembly has a specified resolution of 640 eV at 122 KeV. This also provides timing and energy outputs for data acquisition.

Both detectors were mounted coaxially, one in each of the bore holes of the trap facing the muon stop area in the gas, with the W&M on the side named bottom and the Silgard on the side named top (the trap was originally intended to be rotated 90^o from its present upright position). The distances of the detectors from the center of the trap were determined during the tuning process to optimize the μatom x-ray signal to total rate ratio and to keep the μ-atom x-ray count rate at an acceptable level. These distances from the center were 165mm for the W&M and 70mm for the Silgard (See Fig. 3-3). It was also necessary to put collimators in front of the detectors to keep the rate low enough to prevent the detectors from being overloaded, but keep them close enough to the muon stop region to still to collect data at an acceptable rate. The collimators are copper rings of about 30mm thickness with 55mm holes inside that were placed in the bore holes at the entrance to the gas chamber. The effect of this is to limit the view of the detectors to just the stop region of the muons but not the rest of the inside of the chamber where much of the electron generated x-ray background originates.

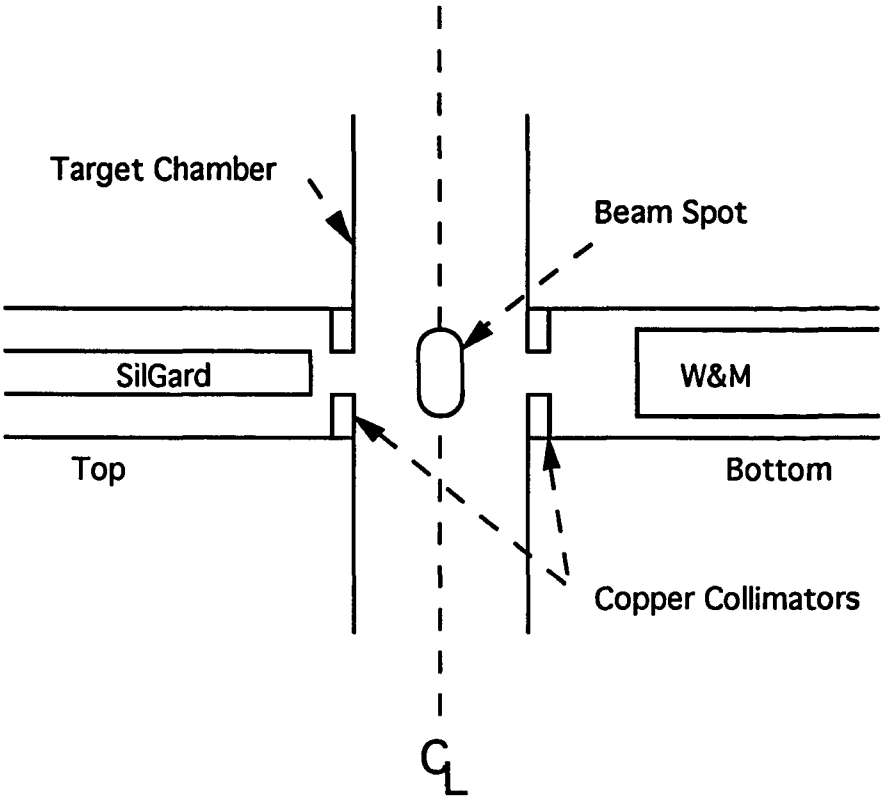

Fig. 3-3 Detector Setup in trap

E. Electronics and Data Acquisition

A system of nuclear electronic moduals were used to process the signals produced by the detectors into a form that the data acqusition system can use and to separate as much of the background from the desired signals as possible to keep the amount of data recorded to a minimum. The elimination of unwanted background increases the time the system is active to accept real events and reduces the amount of time required for off-line data processing.

Both detectors have two outputs from their preamps: the energy signal and the timing signal. The preamp timing output of the Silgard detector was first sent to a fast

Timing Filter Amplifier (TFA) to amplify the weak detector signal and to minimally shape it. The signal was then split and sent to two Constant Fraction Discriminators (CFD), one an upper level and one a lower level, which provided a rough energy window about the muonic x-rays of interest. The output of the lower level CFD was therefore the time signal for the silgard detector, since the desired signals were all process by this CFD.

Occasinal "junk" signals, that were determined to be interference, were observed in the timing signals from the Silgard detector. These signals had a positive component to their pulses, which was used to differentiate them from desired μ-atom x-ray signals. The junk signals were vetoed by branching off a signal from the preamp timing signal, inverted it and sending it to a TFA and CFD. The CFD then produced a signal only on what was originally the positive part of the junk signals and this output was put in anti-coincidence with the lower level signal.

The optical preamp's inhibit was delayed and placed in anti-coincidence with the time signal to prevent data from being taken during preamp resets. A signal from the outer ring detector sent through a TFA and CFD was also placed in anti-coincidence to prevent photons, that crossed both the inner and outer ring of the Silgard detector and deposited an amount of energy equal to a real event in the inner crystal, from being counted as real events.

The RF signal from the main cyclotron was used to create a gate signal during the time that muons could arrive in the trap. The accelerator produces a signal when each bunch of protons is extracted from the main cyclotron. This extraction occurs at a precise rate of 50 MHz for the PSI machine. The arrival time of a muon in the trap is directly related to the time of the proton extraction, so a gate was constructed around the muon arival time using the accelorator signal from the previous proton bunch as the start signal. Additionally, the momentum of the muons was chosen so they arrive at the trap halfway between the electron pulses due to the difference in velocities of the muons and electrons in the beam pipe.

A gate was also created from the T_3 scintillator signal which indicates the possible presence of a muon in the trap and was placed in coincidence with the RF signal gate to form the gate $T_3 \cdot RF$. This combined gate was delayed by ≈100ns and placed in coincidence with the timing signal and a measuring time gate used to fix counting times. This total coincidence formed the gate for the MCA. This final gate then, combines a signal indicating an event took place during the muon arival time, with a signal in scintillator T_3 and a signal in the detector of approximately the right energy, but not junk or a crossing event (See Fig. 4-3). A Macintosh computer (Mac) was used in parallel with the MCA to collect data. A similar coincidence was set up for the Mac which had the timing signal combined with a $T_3 \cdot RF$ signal that was stretched to 4μsecs, but did not include the measuring time coincidence.

A similar upper and lower level timing signal gate was created for the W&M detector. This signal was also placed in coincidence with the delayed $T_3 \cdot RF$ signal and the measuring time gate to create the W&M MCA gate (See Fig. 4-4a).

The energy preamp outputs for the detectors were sent to spectroscopy amplifiers, the outputs of which were then sent to ADC's for the MCA and Macintosh.

To record event time data a start -- a zero point to measure from -- and a stop -- indicated by the Silgard time signal -- are needed. Temporally the start is the $T_3 \cdot RF$ signal indicating a muon has crossed the scintilator in the enterance channel during the expected muon arival time and begun its journey to the center of the trap. However, in practice the rate of $T_3 \cdot RF$ is almost an order of magnitude higher than the Silgard time signal, so it was chosen to reverse the order for recording purposes to keep the number of false events recorded low. The higher rate in T_3 is mainly due to the large number of

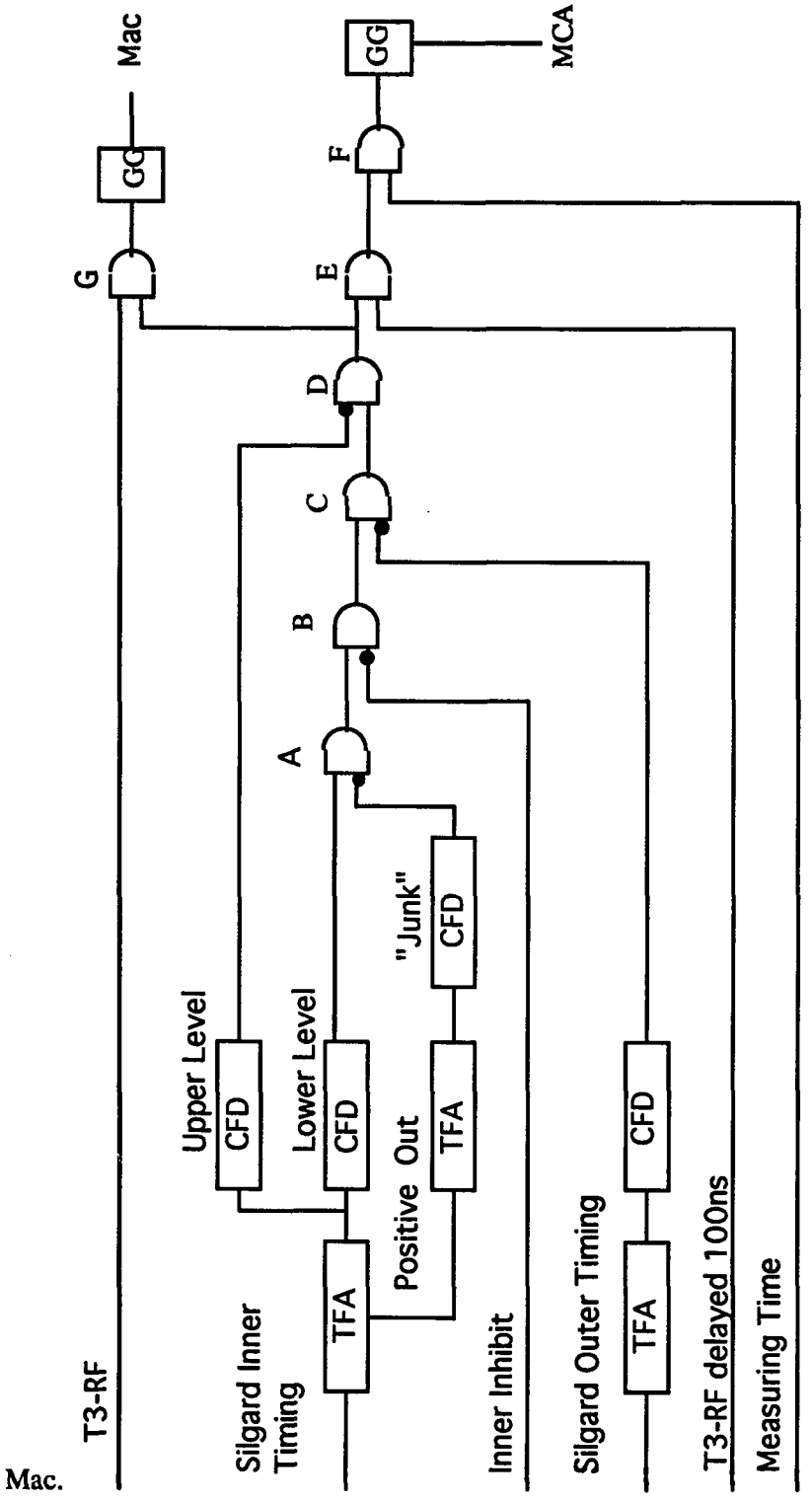

Figure 4-3 Silgard detector gates for the Macintosh and MCA.

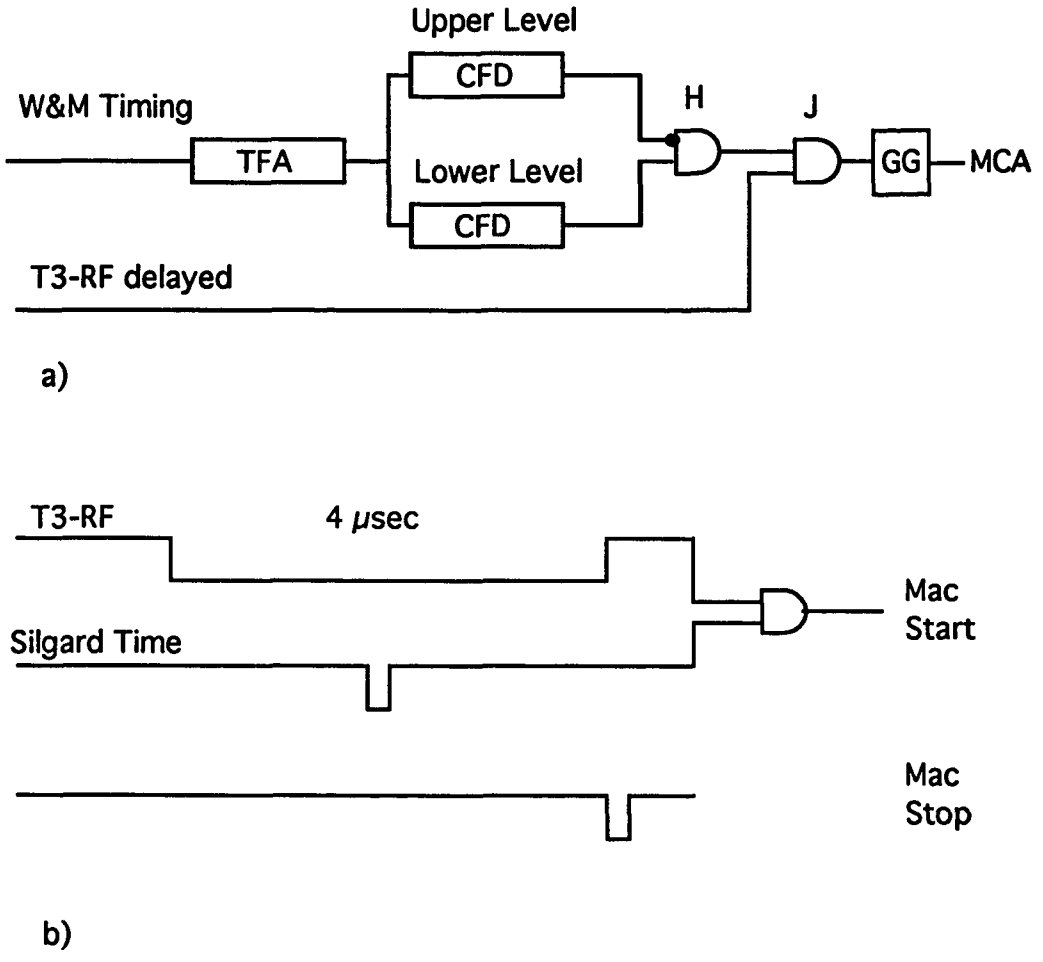

Figure 4-4 a) W&M detector gate for MCA, b) Timing logic for Silgard detector to Macintosh.

electrons in the beam. Although most of the electrons are cut out by the RF gate there are still approximately as many electrons as muons during the muon gate, RF.

Start signals were created for the Mac by stretching the T_3·RF signal to 4μsec and placing this in coincidence with the Silgard time signal, which was subsequently sent to a time to amplitude converter (TAC). The pulse stretcher provides an end marker pulse which was used for the stop signal for the TAC (See Fig. 4-4b). The output from this TAC was sent to a second ADC to be digitized and recording by the Macintosh. With

this method all the stop signals come at the same time after a T_3·RF and the time of the start signal compared to T_3·RF varies.

Events were recorded in parallel and independently with a Macintosh computer and a multi-input multi-channel analyzer (MCA). The Macintosh controlled the CAMAC crate which contained a four input 8000 channel spectroscopy ADC. One ADC input was used to digitize energies from the spectroscopy amplifier and a second to digitize times from the TAC for events from the Silgard detector. An event was indicated (a LAM issued by the ADC unit) when the time ADC digitized a signal. This occured with a rate of a few a second during this run. The commercial data acquisition software Kmax[45] was run on the Macintosh to record the data. Kmax is a complete data acquisition system, which controls the CAMAC crate, sorts events and creates 1D and 2D histograms. Kmax also saves data in individual record event format files which can be played back and the data sorted after the data have been collected. This setup was capable of recording event rates of up to ≈100/sec. The MCA had four built in 2000 channel ADC units which recorded 1D energy spectra from both the Silgard and W&M detectors that were subsequently saved on tape. The MCA recorded an event when it received a gate signal from the timing electronics.

F. Data Runs

Running began with the tuning process to maximize the number of muons stopping in the center of the trap. This was accomplished by filling the gas chamber with Ne to 150 Torr, a pressure with comparable stopping power to the other gases and mixtures planned for use. Ne was also used for tuning in previous runs with the trap, so this was a familiar process with a relatively standard procedure. The W&M detector was inserted in the bore holes of the trap to the desired position and used to count μNe x-rays. A series of tuning steps was then followed to maximize the number of μNe x-rays, and

hence the event rate for all subsequent runs. These steps included adjusting the position of the trap, the beam momentum spread, trap angle and the detector position.

The large number of electrons entering the trap between the muon pulses caused a large background rate in the detectors that threatened to overwhelm the preamps of the detectors. Overloading could have been prevented by withdrawing the detectors to a larger distance from the trap center, but this would have had the adverse effect of also decreasing the effective solid angle, and hence decreasing the event rate to an unacceptable level. However, it was reasoned that the electron produced interference originated away from the beam spot at the center of the trap. Instead of moving the detectors, collimators were placed around the detector windows to reduce their view to only the beam spot region. This allowed W&M to operate below 50KHz, which was found to be the maximum usable rate.

Table 3-1 Conditions run in experiment with data file names for Macintosh and MCA, listed in order run.

Condition	Mac file Silgard	MCA file Silgard	MCA file W&M
CH_4 150 Torr	CH4-150Trans%	85.002, 87.002	84.002, 86.002
"	CH4-150TransB%	89.002	88.002
D_2 697 Torr	D2-697Tran%	91.002, 93.002	90.002, 92.002
D_2 349 Torr	D2-349Tran%	95.002	94.002
D_2 345 Torr	D2-345Tran%	99.002	98.002
D_2 695 Torr	No File	02.003	03.003
CH_4 8 Torr + D_2 570 Torr	TransEvt1%	05.003, 07.003, 08.003	04.003, 06.003, 09.003
CH_4 30 Torr + D_2 570 Torr	TransEvt2%	11.003, 14.003, 15.003	10.003, 12.003, 13.003, 16.003
CH_4 71 Torr	CH4-70Torr%	18.003, 21.003, 22.003	17.003, 19.003, 20.003

Data runs related to the transfer experiment were taken with a number of pressures for deuterium and methane and mixtures thereof. The runs and conditions are listed in Table 3-1. The gas chamber was pumped to vacuum between each change of condition and flushed twice with the new gas. These data were taken sequentially in the order listed in Table 3-1 over a period of three days. The average run time for each MCA file was about three hours

IV
DATA ANALYSIS

A. Introduction

The paucity of data obtained in the run, readily seen from a time vs. energy plot of the transfer data, (See Figs. 4-2) suggested that a significant amount of analysis would be required to extract the desired information from the data. Also, a number of corrections for such effects as time slewing and efficiency drop-off at low energies had to be made to the data before any fitting could be done. This section describes the analysis procedure used to extract the desired information.

B. Software

The majority of the analysis was done using two pieces of software, Kmax (the same application that was used to record the data) and a spectral fitting program called ROBFIT[25] that fits one dimensional peak spectra. Kmax is capable of doing a limited amount of data analysis, such as generating sorts of the data into various one and two dimensional histograms and displaying them as plots. Kmax can also perform mathematical operations on the data before sorting, which was helpful in doing the time slew correction (described later) and other data manipulation.

ROBFIT is a spectral fitting program developed at the University of Florida by a group of astro-physicists to make fits of the low statistics data that is normally acquired in astronomical observations. It is this ability to fit low statistics data accurately and quickly that led to the choice of ROBFIT for this analysis. ROBFIT represents a different philosophy in fitting from that used in standard fitting routines, and so deserves some detailed explanation.

Normally, energy spectra are fitted one peak at a time, using a small section of the spectrum immediately surrounding the peak. A background function, usually a polynomial, is selected for the background, and a peak function, usually a Gaussian or variant thereof, is used to fit the peak. Both functions require user supplied initial parameters, and then the program optimizes the fit, usually using a least squares method to find the best fit parameters. Notice that the existence of the peak and the adequacy of using a small section of background is assumed by this method. The existence of a peak is not always a certainty with low statistics and the shape of a small section of background often does not agree with the actual background derived from the entire spectrum.

ROBFIT overcomes this need for a priori information by fitting the entire spectrum at once, and not assuming that any peaks exist. The spectrum is assumed to be composed of two parts, the background and the peaks. The background is assumed to be a slowly varying function (i.e., has only low frequency components) while the peaks are thought to vary quickly, thus being a high frequency function which sits on the background. The fitting is done using a string of cubic splines to represent the background, and by constructing reference peak shapes from cubic splines to fit the peaks. The reference peak shapes are derived from high-statistics peaks in a calibration run or known peaks in a spectrum. The peak shape is often assumed to be Gaussian if no high-statistics reference peak is available, since for few enough events any peak can be adequately fitted with a Gaussian.

First, the entire spectrum is fitted with a background function which varies slowly compared to the expected peak width. The fitting of data to the functions is done, as with most other fitting routines, using a least squares method. The true peaks, of course, will not be fitted well since they vary rapidly and will deviate greatly from the background function in this first fit. ROBFIT then checks for these places where the data is significantly above this background function, and assigns them to be peak regions. The

peak regions are next fitted with the peak shape function to find the best position, width, and height for each peak. The background is then refitted, taking into account the presence of the peaks, and the process of looking for peaks begins again.

The whole process is repeated until a satisfactory fit is found and then a file is generated with all the peak parameters. What is considered "satisfactory" is determined by the user, but this is not as arbitrary at it might seem, since this mainly comes down to a choice of peak sensitivity. In ROBFIT this is called the cutoff level. In principle the cutoff level is lowered during the fitting process until ROBFIT starts fitting random fluctuations in the background as peaks. At this point all the real peaks will have been found, since fittable real peaks are assumed to be bigger than noise fluctuations, and further lowering will only result in more background fluctuations being fitted as peaks.

C. Calibration - Silgard Detector

A time calibration spectrum: 40nsCalTra%0. (Such designations are used below to identify particular runs.) was used to calculate the time calibration. This spectrum was generated using a pulser whiched produced a sting of starts and stops increasing in difference by 40ns into the TAC. The time pulses were accurate to about a nanosecond, since they created peaks only one channel wide in the 2048 ch spectra. The timing resolution of the data was expected to be about 100ns, so simply choosing two lines and taking their difference gave adequate accuracy for a calibration. Two lines were chosen which are widely separated: channels 111 and 1628, that are 1517 channels apart, a difference of 72 pulses. The time between each line was 40ns, so the difference between the chosen channels was 2880ns. This led to a timing calibration of 1.898ns/ch for 2048 channels and 15.18ns/ch for the 256 channel binning used in the 2-D plots.

Two energy calibrations were done for the Silgard detector, one at the end of the pure gas runs and one at the end of the experiment, CO-57Cal%0 and CO-57Cal3%0 respectively, using a cobalt-57 calibrated source(See Table 4-1)[26].

Table 4-1 Co-57 calibration source data

Half-life	271.79 days	
Photon type	Photon Energy (KeV)	Emission Probability (%)
X	6.391	16.6
X	6.404	32.8
X	7.06	6.63
γ	14.413	9.14
γ	122.0614	85.68
γ	136.4743	10.67

The spectra were initially fitted with ROBFIT using Gaussian peak shapes, fits G2 and G1 respectively (See Table 4-2). Both calibrations are within uncertainty of each other, so no significant drift occurred during the run. These two runs were added together to create one spectrum of better statistics, named Co-57CalT, which was also fitted using Gaussians, fit G3. The quality of this fit was not as good as the fits of the individual runs, but was still at an acceptable level of >1%. The worsening of the fit could be due to the inadequacy of the Gaussian peak shape for fitting higher statistics peaks.

The Gaussians gave acceptable quality of fits for both of the calibration spectra, but only by producing some unknown peaks next to the known peaks. Initially these were thought to be low yield x-rays of the Co-57 or daughters, but lines at these positions could not be found in gamma and x-ray tables. A closer examination showed that all the peaks had the small side peaks next to them. This suggested that they were actually low end tails of the larger peaks and not peaks of separate identity.

A peak shape which included the tails was created from the calibration spectra for use by ROBFIT. Several attempts were made to create an acceptable peak standard, and one, Silgard3.ST, was finally chosen (See Fig. 4-1). This was created from the 6.40 KeV peak of the summed calibration spectrum, which was subsequently refitted as fit ST5, with this peak shape (See Table 4-2). The resulting fit was as good as the fit done with the Gaussian peak shape, and no side peaks appeared next to the known peaks.

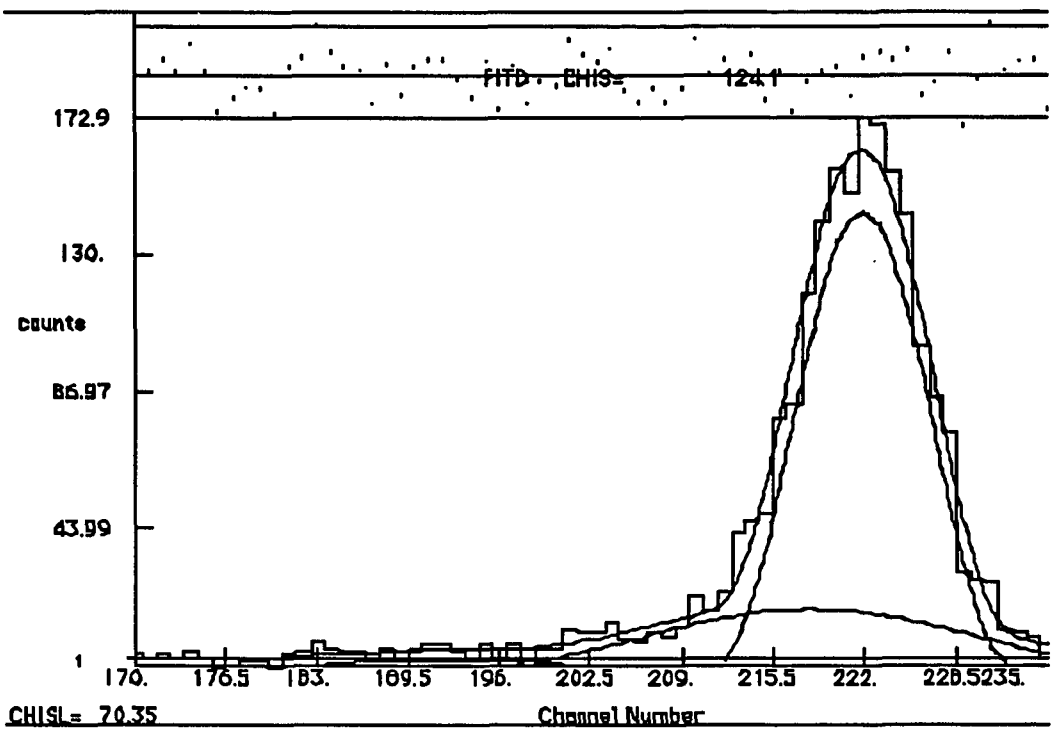

Figure 4-1 Silgard3.ST peakshape standard used by ROBFT to fit all energy spectra.

Table 4-2 Calibration fits Silgard detector, Co-57 source.

		Calibration Line Channel		
Fit	Spectrum	6.40 KeV	14.41 KeV	Goodness of Fit
G1	Co-57Cal3	221.762 ± .172	496.748 ± .332	0.104
G2	Co-57Cal	221.653 ± .301	496.166 ± .623	1.00
G3	Co-57CalT	221.835 ± .190	496.783 ± .310	0.015
ST5	Co-57CalT	221.719 ± .126	496.763 ± .300	0.0118

Obviously if the peak shape is generated from a particular spectrum a good fit is expected from fitting that spectrum.

A comparison of all the calibration fits showed that all fits regardless of run or peak shape were consistent with each other, which gave confidence in the quality of the calibration. Use of the Silgard3.ST shape was nevertheless preferable to using the Gaussian, since its shape more accurately represented the peak shape produced by the detector and electronics. Also, the large tail at the low end significantly affected the number of events fitted in a peak if two peaks were close together. The lower energy

Table 4-3 Calibrated positions of muonic x-ray lines for carbon, deuterium and hydrogen in the Silgard detector spectra (1024 ch).

μC transition	E (KeV)	Channel
6-5	1.29	46.2
6-4	3.48	121
6-3	8.36	289
6-2	22.3	768
6-1	97.6	-
5-4	2.26	79.5
5-3	7.16	248
5-2	21.07	725.5
5-1	96.4	-
4-3	4.88	169.5
4-2	18.81	647.9
4-1	94.1	-
3-2	13.94	480.6
3-1	89.23	-
2-1	75.29	-
μD transition		
2-1	2.00	70.6
∞-1	2.66	93.3
μH transition		
2-1	1.90	67.0
∞-1	2.53	88.8

peak which sat on the tail of the higher peak was fitted by fewer events using Silgard3.ST than if fitted using Gaussians. ST5, the calibration using the peak shape Silgard3.ST, was therefore chosen for the peak shape to do the energy fitting in this analysis.

A linear fit of the form ch= m*E + b was made with the 6.40 and 14.41 KeV lines to create a calibration function.

$$ch = mE + b\ ;\ m = 34.34 \pm 0.04,\ b = 1.96 \pm 0.66 \qquad (4.1)$$

This was used to calculate the channel positions of the carbon, deuterium, and hydrogen muonic x-ray lines (See Table 4-3) that were expected in the data spectra.

D. Data - Silgard Detector

D. 1. Pure Gases

The data set from the Silgard detector was composed of two fields, the energy and time values for each event. The data acquired during the runs were played back and binned into 2-D energy vs. time histograms of 256 by 256 channels using Kmax. Viewing the 2-D spectra gave an estimate of the time structure for the individual spectral lines and an estimate of the time scales involved for stopping of the muons in the gas.

X-rays from the pure gasses, deuterium and methane, were produced by muons stopping in these gases directly. That is the muons were captured by the same atom that produced the subsequent x-rays seen in the spectra. Events produced by this mechanism were called "prompt" events regardless of how spread out in time they occurred. This was to distinguish them from "delayed" events which were the result of transfer that follows prompt events in deuterium.

The first plot, Fig. 4-2a, shows the energy vs. time spectrum of pure deuterium at 697 torr pressure. In the lower left corner are the μd K-line events. They are spread in time over about 300ns, which is therefore approximately the time scale of prompt events for this condition. The trail of events that lies in the time direction at approximately 7.4 KeV is composed of electronic Cu x-rays, which were most likely caused by the large number of electrons in the beam. The muon beam was, in practice, mainly an electron beam contaminated by a few muons (electron / muon ratio ≈ 1000), so large numbers of electronic x-rays are expected. The electrons are the result of pions decaying upstream in the beamline. Notice also the large number of low energy noise events below the μd peaks. This plot also shows that the event data included few μd cascade events, and that the background is sparsely populated. Along both the time and energy axes are found a large number of events. These are referred to as "zeros", which are produced when there is either a signal in the time ADC but not in the Energy ADC or the reverse. Zeros do not correspond to real events, and care must be taken to eliminate them from data subsets while doing analysis.

The next plot, Fig. 4-2b, is of the 150 torr methane data, which was made by combining the two data sets, CH4-150trans% and CH4-150transB%. Four muonic carbon lines can readily be seen, the 5-4, 4-3, 3-2 and 4-2 in increasing energy order. There is also a muonic Al 4-3 line at 23 KeV, and some electronic Cu events are also visible. The scale of the carbon peak time widths is about 100-150ns for this pressure. The background is also sparsely populated for these data. The abrupt change in the background density of events at ~ch 130 is due to the two data sets having different time gates, where one data set goes further in time then the other.

Fig 4-2a

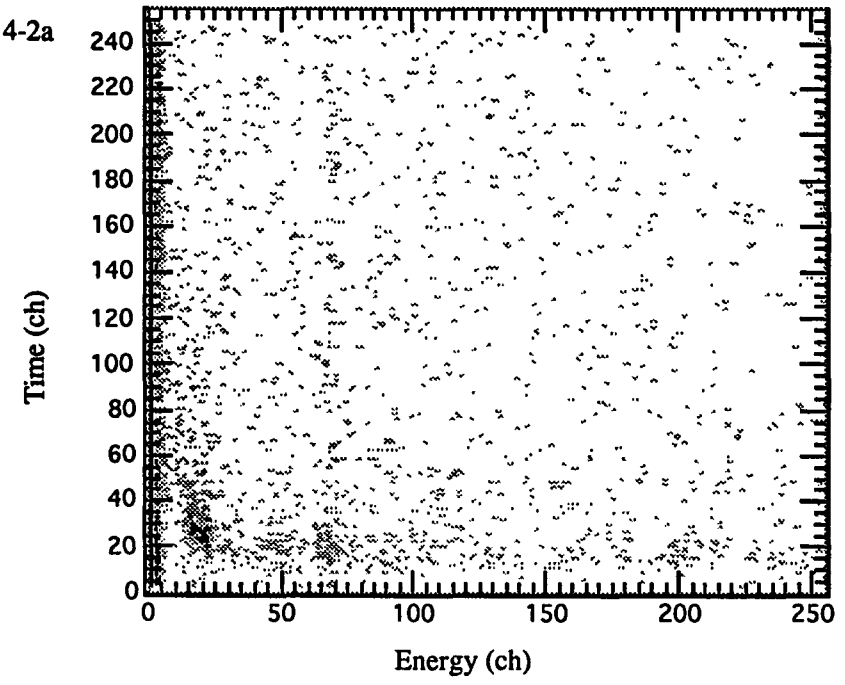

Fig 4-2b

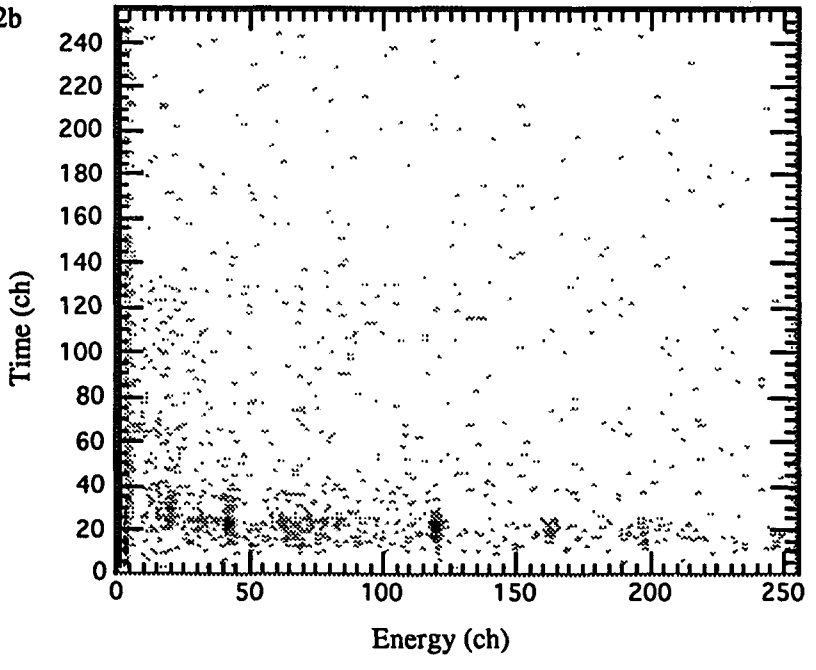

Figure 4-2 Energy vs. Time spectrum Silgard detector for
a) 697 Torr D2 and b) 150 Torr CH4

The previous plots are both for pure gas targets, so all of the muonic x-ray events are prompt. Both of these pressures were chosen because they had approximately the same stopping power for muons as the mixture, therefore the prompt stopping times should be approximately the same as for the mixture. The difference between the time widths in the two gasses (~300ns compared to ~150ns) was found to be mainly due to time slewing, which will be described later.

Looking at the 2-D spectra was useful for learning which major lines were in the data and their relationship to each other, but a more accurate method of peak identification was needed. This was done by summing over time the data that occurs later than time channel 13 (256 channel scale) into 1-D energy spectra and then fitting these spectra to find the peak values. The times of included events were from approximately 200ns to the end of the time scale. The initial cut point was chosen to eliminate the zero's at the bottom of the time scale without cutting into those events which included the peaks to be fitted. (Cuts over this time range are referred to as Total-E cuts.)

The energy spectra were then fitted with ROBFIT using the Silgard3.ST peak standard. Fitting was repeated with progressively lower cutoffs until random background fluctuations started to become peaks. In practice real peaks were found to be detectable to a level where the ratio of peak area to its uncertainty ($A/\Delta A$) was approximately 2 to 1.

All spectra were fitted using channel numbers for convenience, rather than a calibrated energy scale. The positions of peaks are therefore given in channel numbers, and the corresponding energy can be found in the calibration Table (4-3) or by means of the calibration function, Eq. 4-1.

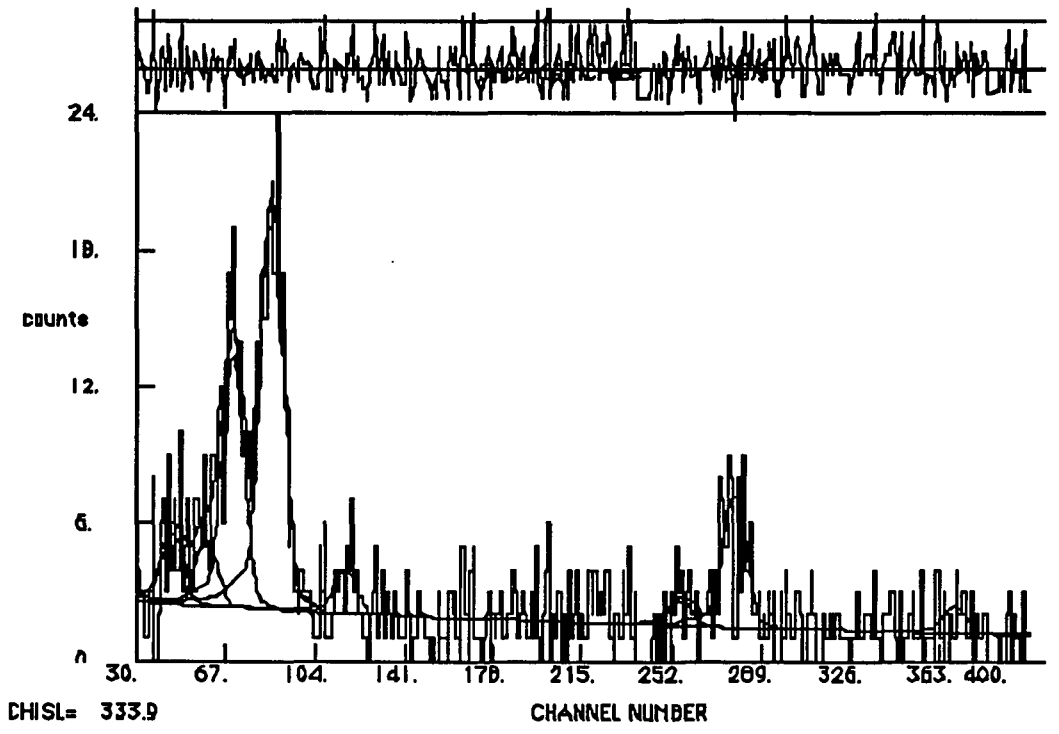

Figure 4-3 Spectrum of energy fit, 697 Torr D2

The peak file from the fit of deuterium 697torr data is shown in Table 4-4 and a plot of the lower part of the spectrum in Fig. 4-3. Two deuterium peaks were fitted. The peak at channel 69.7 is the 2-1 transition while the other, at channel 85.9, includes all the higher K lines, because the detector resolution was insufficient to separate them. The electronic Cu is seen in channel 277.8. Two other peaks are fitted above the noise level, at ch 44.9 and ch 58.7, since they have ≈35 events in each they are clearly not random fluctuations, but neither of these peaks corresponds to any known line. Both of these were determined to be noise, since the energy efficiency of the detector goes to zero at ≈ ch 50 (window 40μ Be) and the energy threshold of the constant fraction discriminator is set approximately at this level. Also low energy noise around these channels was noted during the run when CFD thresholds were being set. The small peak at ch 116 (3.32

KeV) was never identified, but did not correspond to any muonic x-rays of any of the gasses or materials in the trap. All the other peaks listed are of low signal to noise and do not correspond to known lines. These were therefore most likely to be peaks due to "fitting down to the noise level." No events of muonic carbon were found, so no carbon background exists to obscure the events from the methane gas.

The Total-E fit of the summed methane 150 torr runs is in Table 4-5, and a plot of the low end of the spectrum is shown in Fig. 4-4. Starting from the low end are the two "low end noise" peaks described previously. Then at ch 77.6 is the μC 5-4 line, at ch

Table 4-4 D_2 697 torr, Total-E fit, ROBFIT peak file.

17 PEAKS	979 CHAN	CHIS= 882.9	NITB= 4	CUTOFF= 2.00	
Position (ch)	Position Err. (ch)	Width (ch)	Width Err. (ch)	Area	Area Err.
44.892	1.780	10.934	1.014	37.7479	10.87
58.675	3.136	10.903	1.015	34.5911	15.12
69.748	.906	10.994	1.172	136.842	21.08
85.949	.462	11.531	1.007	233.854	19.77
116.331	2.021	10.770	1.000	22.9423	8.009
255.915	3.288	10.850	1.058	13.2929	7.314
277.813	.869	11.845	1.063	76.5455	11.62
369.152	2.667	11.070	1.005	13.8725	6.187
419.682	2.703	10.827	1.006	13.4743	6.170
435.717	3.026	11.011	1.006	11.9799	6.036
471.486	3.813	10.899	1.005	8.74393	5.575
488.749	4.238	10.774	1.005	7.44446	5.302
516.654	4.243	10.888	1.005	7.27055	5.149
667.072	2.745	10.782	1.017	11.1676	5.310
720.680	3.621	10.808	1.017	8.17301	5.037
801.718	2.400	11.318	1.000	13.4781	5.389
854.340	2.335	11.002	1.000	13.2326	5.322

126.4 some μC 6-4 events and the μC 4-3 peak at ch 170.8. Next come a group of closely bunched peaks, which include the electronic Cu peak seen at ch 275.0 and other peaks that were not readily identified. These are thought to be a combination of some non-circular μC events, 5-3, 6-3, 7-3, and other electronic x-rays from stainless steel parts inside the gas chamber. Stainless steel contains iron, nickel, cobalt and other close atomic number elements which have electronic x-rays in this region. Interestingly, these other peaks are not seen in the D_2 spectrum, with the exception of what may be the beginning of a peak in ch 255.9. The combination of both the electronic and μC events could be enough to be fitted as peaks, while in pure D_2 the presence of only the electronic x-rays may not be enough to rise above the background to a level where ROBFIT can discern them. The μC 3-2 and 4-2 peaks were also found. No significant numbers of events were recorded at the locations where muonic hydrogen x-rays were expected, channels 67.0 and 88.8, suggesting that all muons which interact with a methane molecule capture directly on the carbon nucleus.

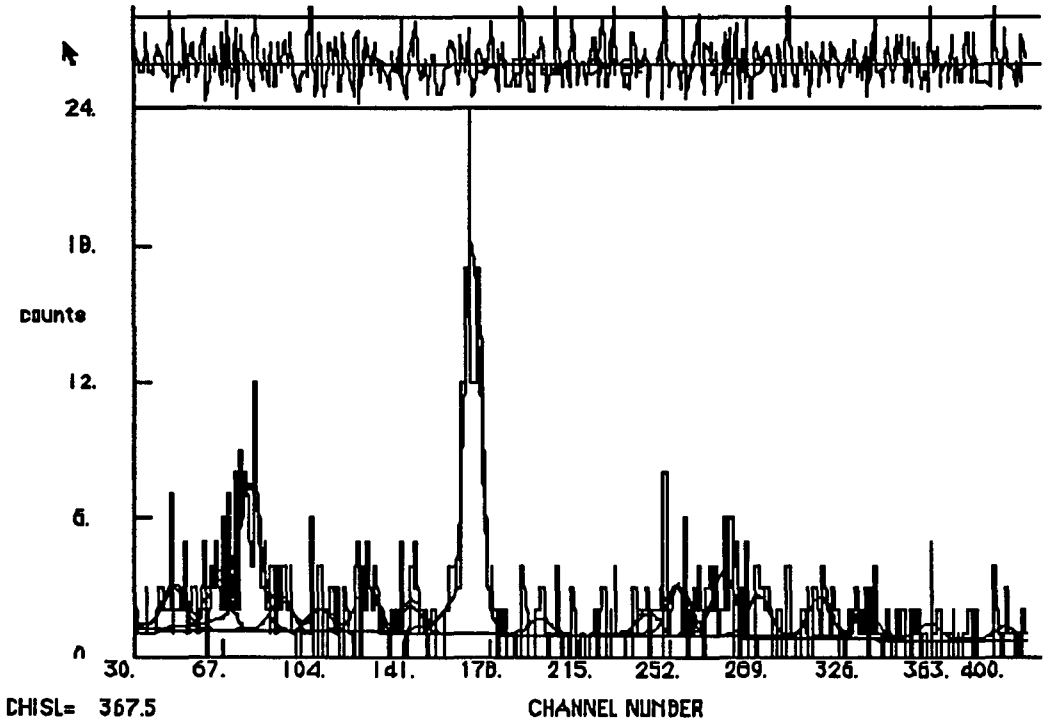

Figure 4-4 Spectrum of energy fit, CH4 150 Torr

D. 2. Gas Mixture

The single gas runs showed the structure of pure gas muonic event data, which had only prompt event peaks. Together, the deuterium 697 torr and methane 150 torr runs comprised the control run for the transfer data. That is, if no transfer took place then the 2-D plot of the gas mixture data would look like a sum of the two individual gas data sets properly scaled for the relative stopping powers of each gas in the mixture. This would in principle be a spectrum only of deuterium and carbon prompt x-rays all coming in the first few hundred ns (about 20 ch on the 2-D time axis).

Two mixtures of methane and deuterium were used for the transfer study. The first was 8 torr of methane with 690 torr of deuterium, a slightly greater than one percent concentration of carbon. Data from this mixture, TransEvt%, collected over eight hours

Table 4-5 CH_4 150 torr, Total-E fit, ROBFIT peak file.

20 PEAKS	979 CHAN	CHIS= 741.5		NITB= 4	CUTOFF= 2.00	
Position (ch)	Position Err. (ch)	Width (ch)	Width Err. (ch)	Area	Area Err.	Name
46.506	2.143	11.146	1.081	21.4636	7.796	noise
64.795	2.418	11.058	1.092	25.6635	9.904	noise
77.560	1.041	10.796	1.174	75.3235	13.48	μC 5-4
90.584	3.323	10.731	1.086	15.3138	8.077	-
107.235	3.534	10.959	1.080	11.1356	6.511	-
126.408	1.752	10.768	1.082	24.2032	7.640	μC 6-4
144.558	2.811	10.823	1.080	14.0944	6.852	-
170.769	.351	8.177	.736	157.293	14.80	μC 4-3
198.624	4.123	11.104	1.080	8.34641	5.659	-
243.539	3.756	11.071	1.044	12.2959	7.157	-
255.782	1.988	11.314	1.054	26.7118	8.453	μC 5-3 $+e^-$
274.980	1.492	11.386	1.053	33.9560	8.449	e^- Cu
289.453	1.974	10.933	1.047	21.6650	7.239	μC 6-3 $+e^-$
314.889	1.736	10.908	1.041	21.5817	6.710	μC 7-3 $+e^-$
333.753	2.236	11.026	1.040	15.4873	6.019	μC 8-3 $+e^-$
390.991	4.243	10.926	1.040	6.91869	4.834	-
481.664	.342	9.737	.699	189.307	14.62	μC 3-2
648.857	1.631	11.136	1.000	19.8722	5.743	μC 4-2
765.352	3.166	10.991	1.000	8.81329	4.482	-
791.674	1.635	10.427	1.000	17.2924	5.296	μAl 4-3

of run time showed no clear evidence of transfer, so the run was suspended and another combination tried. Next was a mix of 30 torr methane and 570 torr deuterium, which is about five percent carbon. This was more successful, and was used for the rest of the transfer data run. The data set for this mix is TransEvt2%.

The time vs. energy plot for the transfer data, TransEvt2%, is shown in Fig. 4-2c. In the lower left corner are the deuterium K-series x-rays, which may also include some

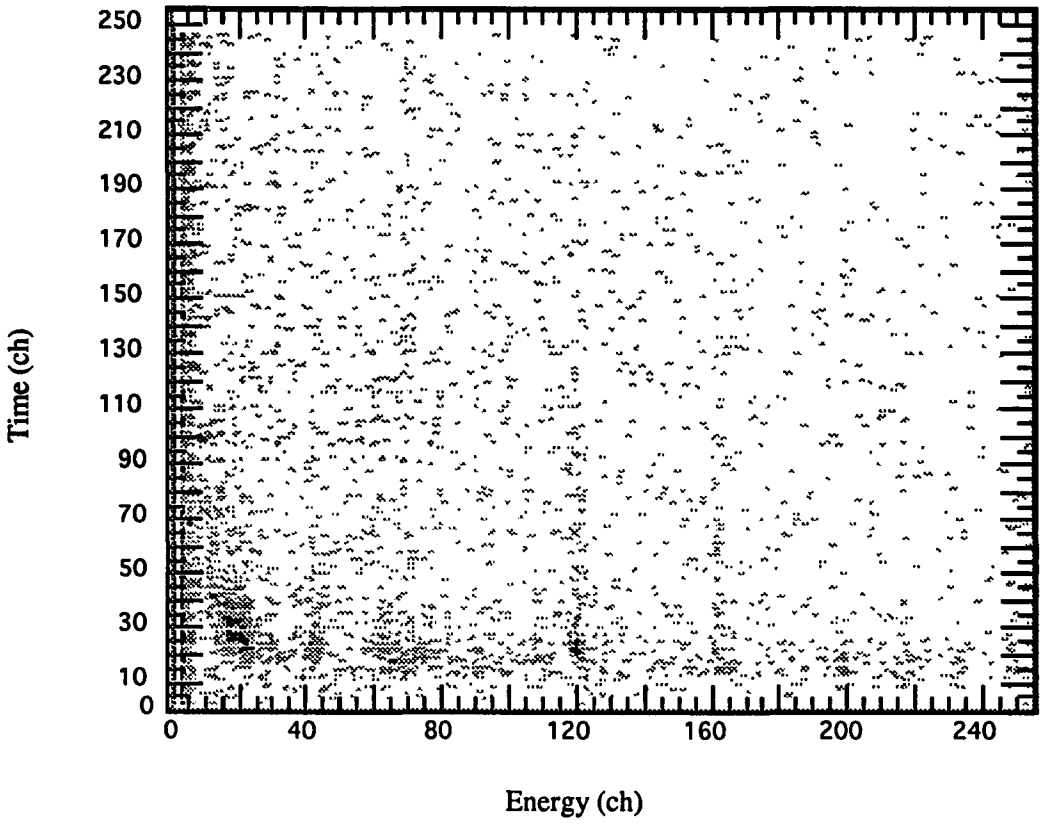

Figure 4-2c Energy vs. Time spectrum Silgard detector for TEvt2 mixture, 30 Torr CH4 and 570 Torr D2.

μC 5-4 events, since they overlap in energy. The electronic Cu x-rays are the same as in the pure gas data. Muonic carbon events are also present, specifically the 4-3, 3-2, and 4-2 transitions, some of which appear as prompt peak events. But now a major difference is visible. The carbon lines not only have the prompt peak events, but also trails of events starting at the prompt peaks and going out to later times. This can be seen very clearly for the μC 3-2 peak and for the 4-2, and close inspection will also reveal a trail coming from the 4-3 line.

In the mixture data, the prompt peaks of carbon should have the same time structure as those of deuterium. Both types of molecules are involved in the muon

slowing down process, and the muon can capture on either a deuterium or methane molecule. The distribution of prompt capture times is therefore the same for both types of molecules. This allows the time distribution of the carbon prompt peak, which is merged with delayed events, to be determined by comparing the μC peak times to the deuterium prompt peak times. The equivalence of the stop time distribution implies that the trails cannot be formed by prompt stops, since the μd prompt peaks occur in the first few hundred ns, whereas the trails continue later. The trails must therefore be x-rays resulting from muon transfer from muonic deuterium to methane after the μd has spent time diffusing through the gas.

A 1-D Total-E spectrum was created from the transfer data to do a proper peak identification. The peak file is in Table 4-6 and a plot of the lower end of the spectrum is

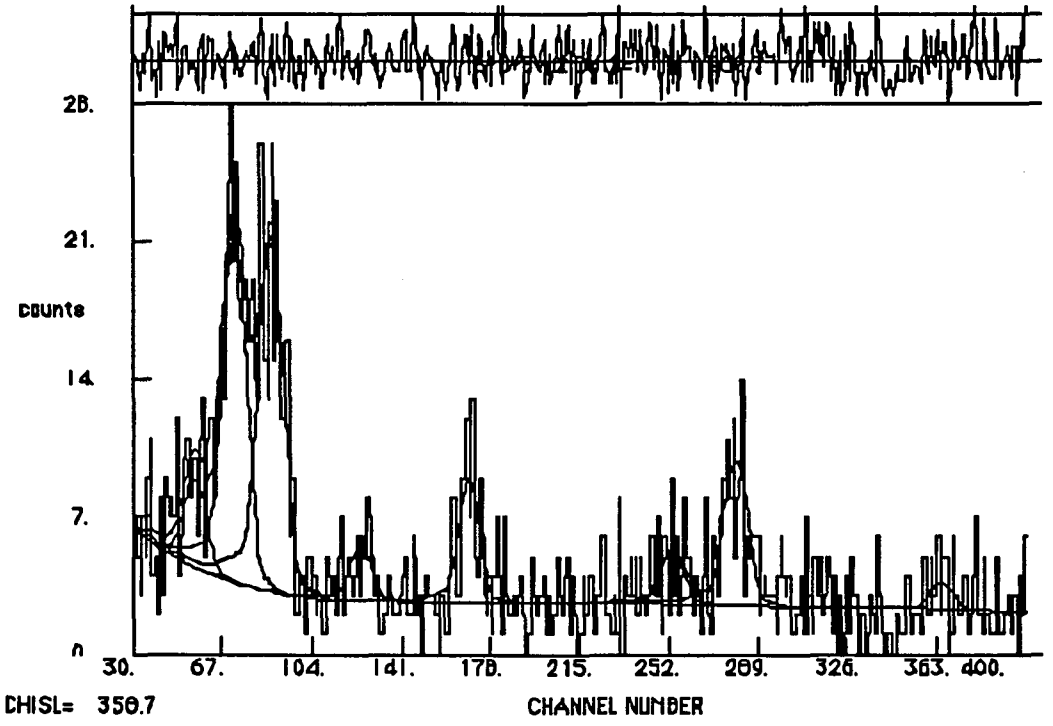

Figure 4-5 Spectrum of energy fit, 30 Torr CH4 + 570 Torr D2

in Fig. 4-5. At the low energy end are again the noise peaks. Next are the μd peaks, and although there are some μC 5-4 prompt and possibly some delayed events mixed in, ROBFIT was not able to resolve them into a separate peak. An attempt was made to find a μC 5-4 peak, by editing the peak file to include a small peak at the μC 5-4 location. The edited peak file was used for the initial parameters for the fit (ROBFIT has an option to do this). As the fit progressed, ROBFIT found it preferable to eliminate this additional peak and return a peak fit file that was the same as the previous fit. The presence of prompt μC 5-4 events in the μd peaks is accounted for later. The 4-3, 3-2 and 4-2 μC lines are also present in the total energy spectrum. The only other μC lines found were the possible prompt non-circular events mixed in with the electronic x-rays, and no unexpected peaks were found.

Table 4-6 30 torr methane + 570 torr deuterium mixture, Total-E fit, ROBFIT peak file.

13 PEAKS	971 CHAN	CHIS= 968.7		NITB= 6	CUTOFF= 2.50	
Position (ch)	Position Err. (ch)	Width (ch)	Width Err. (ch)	Area	Area Err.	Name
55.612	1.581	11.324	1.011	57.6489	14.56	noise
71.904	.709	12.121	1.284	238.415	29.30	μd 2-1
86.926	.729	12.980	1.337	258.319	28.82	μd n-1
124.134	1.600	10.968	1.000	34.4867	9.429	μC 6-4
169.427	.811	10.236	1.001	72.8782	11.60	μC 4-3
254.055	1.828	11.470	1.055	34.6378	10.30	μC 5-3 +e^-
279.918	.811	11.849	1.059	99.1330	13.83	e^- Cu
364.974	3.188	10.991	1.102	16.5285	8.726	-
481.760	.508	10.306	1.065	143.844	15.16	μC 3-2
648.567	1.001	11.182	1.001	51.0286	9.244	μC 4-2
795.848	1.361	10.730	1.041	30.3489	7.654	μAl 4-3
827.283	3.336	10.809	1.041	9.92377	5.666	-
869.074	2.930	10.935	1.041	11.6850	5.849	-

E. Time Slewing

The 2-D energy vs. time plots also show an effect that distorts the data. At the low end of the energy scale (< 4 KeV), the event peaks are pushed to later times than the higher energy peaks. This is called time slew, and is an effect of the of the constant fraction discriminator (CFD) in which the CFD tends to delay the output timing signal it produces when it processes a low energy signal. Slewing is a function of the pulse height only, and therefore will be the same in all spectra, so only one correction function needs to be created for correcting all the data. The elimination of time slew is necessary before any study of the time structure can be done.

The positions and shapes of the prompt peaks in time are due to three factors: 1) the slowing down and capture time distribution in the gas, 2) the time resolution of the detector - electronics setup, 3) added effects of changing detector response and resolution with energy, and time slew caused by the electronics. Since the factors listed in 3), are expected at low energies, the shape of the time distribution will change asymptotically with increasing energy into that of the stop-capture distribution with the resolution folded in.

If muon slowing and stopping were the only mechanism involved in determining the timing of x-ray events, all peaks would have the same time distribution. The cascade time[22] is much quicker than the prompt stop time resolution of the detector (which was measured during setup and calibration) so it will not significantly affect the event timing. The total cascade time is less than the time of one channel in the 2-D plots, so all the prompt peaks also should be centered about the same time channel. However, the prompt peak centroids shift toward later times with decreasing energy. This is visible in all of the 2-D spectra. In the CH4 150 torr plot, where the μC 5-4 peak is time shifted slightly from the rest of the μC peaks, the Compton events from the prompt peaks fall between the peaks forming an easily visible curve showing the slew. Also, slewing can be seen in the D2 697 torr plot where the μd peaks are apparently broadened and the 2-1 peak

appears to be smeared out in time. The time smearing of the deuterium lines is also seen in the plot of the mixture data. Slewing of the μC peaks and their relation to the μd peaks is harder to see in the mixture 2-D plot, because of the trails which obscure the positions of the prompt peaks.

Correcting for the time slew first requires that the slew function be determined across the energy range of interest, which includes both the μC peaks and the μd peaks. These two sections of the slew function overlap between the μd n-1 and μC 5-4 line, so they can be combined to create the entire slew function, by either interpolating between them, or by finding a relation between two peaks of deuterium and carbon, from the mixture data prompt peaks.

E. 1. Time peak centers

Two methods were tried for finding the centroids of the time peaks since the low statistics of the data did not suggest an obvious best method.

The first method for finding the peak centers was to integrate through the peaks in increasing steps of time, and then find the midpoint of the integral. The integration was done by making time cuts through the 2-D data and compressing the cuts into 1-D energy spectra which were then fitted using ROBFIT. The number of events in a peak is equivalent to the value of the integral through the peak up to the time of the cut. A series of energy spectra was created by making time cuts starting at the same initial value, channel 13 on the 256 ch scale, and ending in channels that were progressively later through the peaks. Additional cuts were made until the peak was passed, at which point the entire peak was integrated over and the integral reached its maximum. These are called "prompt" energy spectra, the remainder of the data, from the time cut points to the end of the time channels, were also projected into energy spectra and are called "delayed" spectra. The entire data set is therefore separated into two parts, prompt and delayed, by

each time cut. (The sum of both prompt and delayed energy spectra is equivalent to the Total-E spectra used to do the peak identification in section D.)

The integral values provided by the prompt fits for each peak of interest were plotted as a function of time (channels) and fitted using a non-linear least squares routine (from the commercial application Kaleidagraph[30]). Since the peaks are assumed to be approximately Gaussian in shape, the integral through the peak should be the equivalent to the definite integral of a Gaussian from zero up to the cutoff. Unfortunately the integral of a Gaussian does not have a simple closed form, so it would be difficult to use. A similar function was used instead, that of an approximation to a step function[29], which has the form

$$I = \frac{1}{2}a(1 + \tanh(n(t - b))) \tag{4.2}$$

where a is the amplitude, b is the time offset, and n is a parameter to control the sharpness of the step. This function is a good approximation since it starts at zero, climbs over a finite width, and then reaches a maximum. It also has the added benefit of being able to interpret the parameter b, with its associated uncertainty, as a measure of the peak position. Integrating through the time peaks was done for both of the deuterium peaks and for the μC 5-4 peak. The fit parameters are shown in Table 4-7 and an example of a plot for deuterium is shown in Fig. 4-6.

The second method was to create one dimensional time spectra for each peak from the 2-D spectra, again using Kmax. Cuts were made three standard deviations (3σ) wide around the peaks in the energy direction to create time lanes that contain the muonic x-ray data. This is wide enough to include most of the peak events while keeping background and interference from other peaks minimal. Creating the 3σ cut was no problem for the carbon peaks, but for deuterium the two peaks overlap and are too close together to make such a wide cut. For deuterium the outer sides of the two peaks were

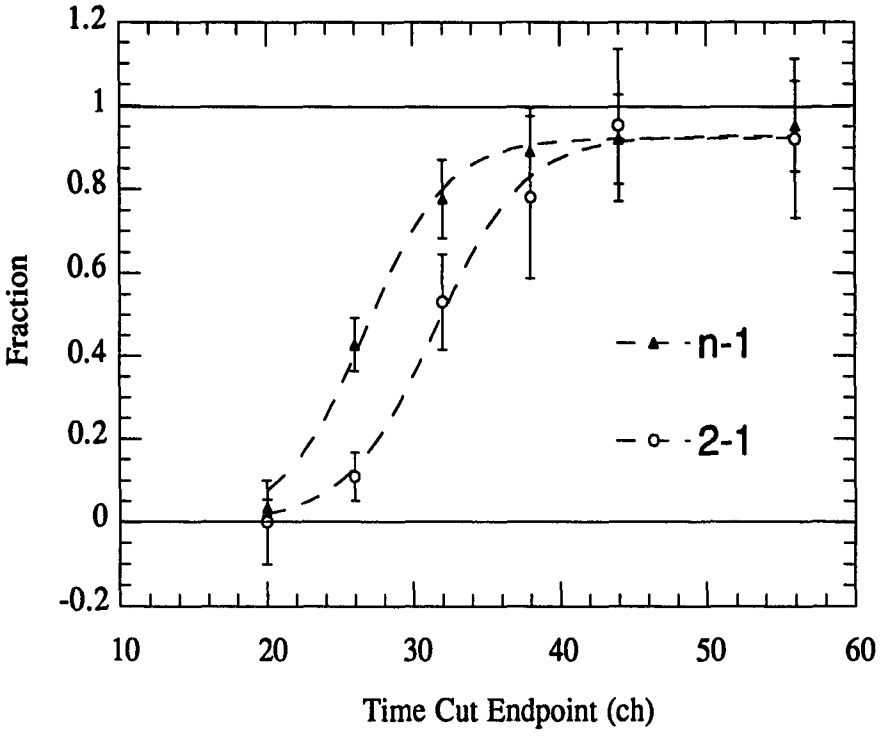

Figure 4-6 Fits of integrated time cuts to find midpoints of D2 697 torr 2-1 and n-1 prompt peaks.

Table 4-7 Fits parameters for slew correction using the integral method on prompt peaks. R is a measure of goodness of fit, where a value of R=1 indicates a perfect fit.

Peak	a	b	n	R
μd 2-1	0.928 ± .032	31.5 ± .6	0.16 ± .03	.9966
μd n-1	0.922 ± .023	26.7 ± .4	0.18 ± .03	.9970
μC 5-4	0.809 ± .040	29.1 ± .6	0.168 ± .03	.9973

taken 1.5σ wide and the cut between was made where the fit of the two peaks intersected. The values of the peak centroids and widths were taken from the Total-E fits to determine the energy cut parameters.

The time distributions were then fitted using a program named FIT created by DeLatt.[27] This is a traditional fitting program which uses peak functions and background functions in a small area around the peak to be fitted. Fits were done using Gaussians for the prompt peaks on a linear background. Fitted centroids were used for the time peak location. Although the peaks did not appear to be perfectly Gaussian in shape, the low statistics allowed for good fits anyway. This was considered acceptable since goodness

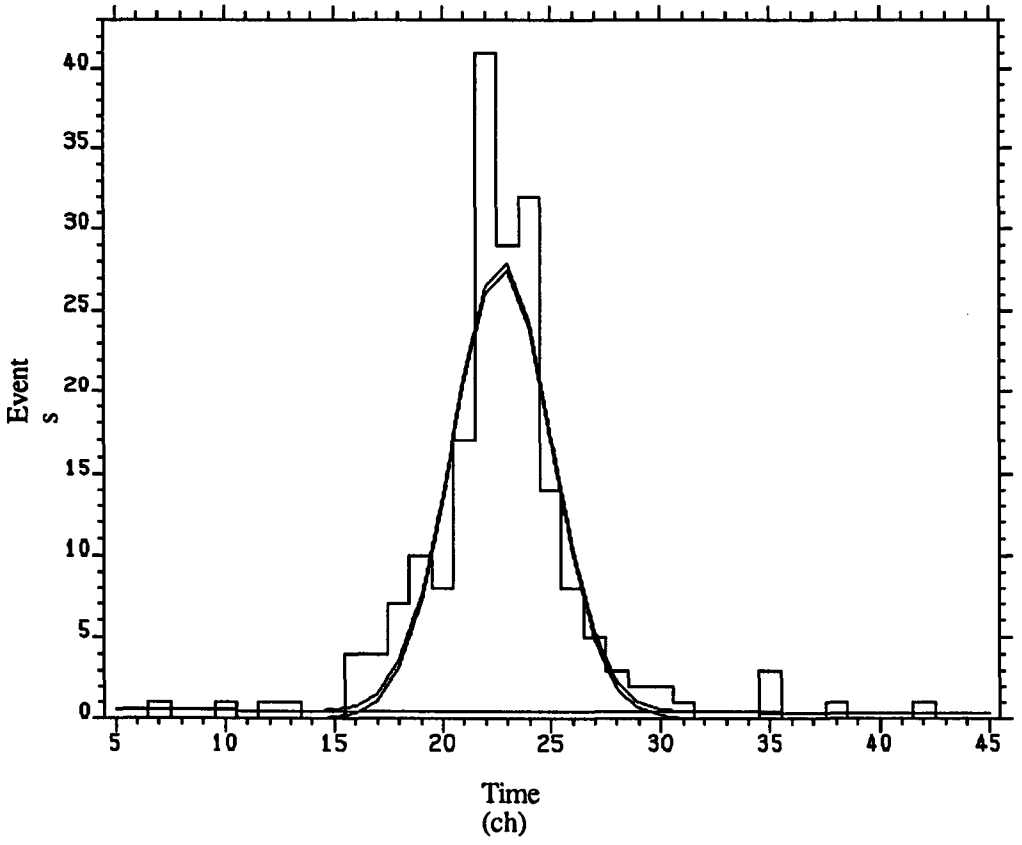

Figure 4-7 Fit of μC 3-2 prompt peak time spectra for finding time slew values.

Table 4-8 Fit parameters for time spectra of deuterium and carbon for slew correction.

Line	Energy (ch)	Position (ch)	FWHM (ch)	χ^2_ν
μC 4-2	648	22.0 ± .7	6.8 ± 1.7	0.22
μC 3-2	481	22.8 ± .2	5.4 ± .4	0.81
μC 4-3	170	23.6 ± .2	5.4 ± .4	0.86
μC 5-4	80	27.6 ± .8	10.3 ± 1.9	0.78
μd 2-1	69.7	31.5 ± 1.0	15.4 ± 2.3	0.84
μd n-1	85.9	26.2 ± .3	7.2 ± .5	0.70

of fit is the determining factor in the fitting process. The results of the fits are listed in Table 4-8, and an example of a fit is shown in Fig. 4-7. (A bug was found in FIT that causes it to improperly weight the channels that have no counts in them. This was not considered a problem since the fits were good, few channels had zero counts, and the peaks had many events.)

The time centroids from the peak fit and the center values (parameter b) from the integral fits are in good agreement. This gives a high degree of confidence in the determination of the peak time locations and indicates that either method may be used. The use of Gaussians for fitting of time spectra was chosen to do the slew correction however, because it is much simpler, and it gives the peak width as an added bonus.

The next step was to determine the prompt time values of the deuterium and carbon x-rays in the gas mixture data (TransEvt2%). This was done using the fitting procedure used for the pure gas cases. Although there was interference between the carbon and deuterium peaks and the carbon prompt peaks had trails, the clearest peaks from each gas were extracted and found to be suitable for this purpose. These were the μC 3-2, since it had the largest statistics, and the μd n-1 because it had less distortion than the 2-1 and was farther from the μC 5-4 peak, which caused some contamination.

In making the μd n-1 time peak sort it was not possible to use the same energy cut used in the pure gas case because the close location of the μC 5-4 line made it necessary to have a tighter cut around the μd n-1 peak. The fit of the transfer data (See Table 4-6 and Fig. 4-5) had only the two deuterium lines, but they were not as neatly separated as in the pure gas case (See Table 4-4 and Fig. 4-3). This may be due to some μC 5-4 events occurring in between, at channel 80 (1024). The high side of the μd n-1 peak had no interference, so the same 1.5σ cut could be used as in the pure gas. For the low energy side however, something closer to the peak centroid had to be used.

If it is assumed that x-rays from prompt stops in the methane of the mixture occurred with the same relative intensities as they did in the pure methane, then an estimate of the number of μC 5-4 prompt events in the transfer data can be made. The fit for the Total-E spectrum for pure methane (See Table 4-5) gives the ratio of 5-4/4-3 x-ray intensities as 0.48. For the transfer data the number of μC 4-3 events, including delayed, is 71. This leads to a maximum expected amount of prompt μC 5-4 events of 71 x .48 = 34. The number of μd n-1 events is 242 ± 22, so the contributed contamination ,if all the μC events were in the μd peak, would be about 50% more than the uncertainty in the measured value. The position of the μd n-1 is 87.1 with a FWHM of 11. If the same width is assumed for the μC 5-4 peak and the low energy side of the μd n-1 is taken to be the center of the expected μC 5-4 peak, then this cuts out half of these events and reduces the contamination to ≈17 events. This level of contamination was less than the uncertainty and therefore thought to be negligible.

The fit of the μC 3-2 peak was not difficult because the delayed trail simply appeared as a higher background on the later time side of a clear prompt peak.

The fit time positions of 23.6 ± .4 for the μC 3-2 and 27.5 ± .3 for the μd n-1, differ by 3.9 ± .5 channels for the mixture data. In the pure gas case the time difference was 3.4 ± .4 channels. The time difference between the two pure gas data sets was therefore offset by 0.5 ± 0.6 channels from what actually occured. To correct for this

Table 4-9 Slew values for fitting the slew function of the Silgard detector.

Line	Energy (ch) (1024)	Time (ch) (256)
μd 2-1	69.7 ± .9	32.0 ± 1.2
μC 5-4	77.6 ± 1.0	27.6 ± .8
μd n-1	85.9 ± .5	26.7 ± .7
μC 4-3	169.5 ± .9	23.6 ± .2
μC 3-2	481.9 ± .5	22.8 ± .2
μC 4-2	648.1 ± .9	22.0 ± .7

offset 0.5 ± 0.6 was added to the μd peak times. This insured the effects of the associated uncertainty due to this offset were included in the final values. Combined with the μC peak time values, these new deuterium values made up the values for finding the slew function (See Table 4-9).

The slew values were fitted with a function of the form,

$$t = \frac{b}{(E-a)} + c \qquad (4.3)$$

which gave a good quality of fit (goodness of fit = 0.16) with only three parameters, a = 57.0, b =116, and c = 22.5 where both energy and time are given in channels. Notice that this equation has an asymptotic form, t --> c, which corresponds with the expectation that the slew will decrease asymptotically with increasing energy.

The event data were replayed and the Silgard timming was corrected for slew. This was done by subtracting b/(E-a) from the raw times. The constant (c) only represents the displacement of the peak centers from zero, so it need not be included in the correction. This new instrument was used to create time histograms of peaks for the pure gas data to see what effects slew correcting produces on the peak shape and distribution. These slew corrected time peaks were then refitted in the same manner as the uncorrected peaks. The results are listed in Table 4-10.

Table 4-10 Fit parameters for time spectra of deuterium and carbon after slew correction.

Line	Energy (ch)	Position (ch)	FWHM (ch)	χ^2_ν
μC 4-2	648	22.2 ± .9	7.6 ± 2.2	0.30
μC 3-2	481	22.9 ± .2	4.9± .4	0.84
μC 4-3	170	23.3 ±.2	5.4 ± .4	0.78
μC 5-4	80	22.9 ± .9	8.4 ± 1.9	0..65
μd 2-1	69.7	21.8 ± .6	9.2 ± 1.4	0.88
μd n-1	85.9	22.6 ± .3	7.1 ± .6	0.94

Comparing the widths after slew correction with the corresponding peak widths before correction shows that the widths of the peaks from μd n-1 and above in energy, did not change significantly. The widths of the lower energy peaks are now much less than before correction and match those of the higher energy peaks more closely. So time slew did contribute to the broadening of these widths. The corrected time widths of the lower energy peaks are not exactly the same as the higher ones however, so another factor, probably intrinsic detector response, is responsible for the remaining difference.

Two other parameters of interest were determined using the time peak fits. They are the intrinsic detector time resolution and the μ stop time distribution in the gas. The time widths of the high energy prompt peaks, after slew correction, should only be a function of these two factors, since the detector response changes happen only at low energies. The slowing down process happens through collisions with individual molecules in the gas, so there is a certain average number of collisions before capture occurs. The time for these collisions therefore depends on the density of the gas, with the stop time and the stop distribution time both being inversely proportional to gas density. A comparison of the time peaks from two different pressures of gas, CH_4 70 torr and CH_4 150 torr, was made to measure this effect.

After slew correction, the CH_4 70 torr data were binned into time spectra around the μC peaks and fitted in the same manner, as were the CH_4 150 torr data (See Table 4-11). The time widths of the high energy peaks have values of ~5 channels for 70 torr and ≈ 6 channels for the 150 torr, which is not significantly different. This suggests that the time width is due almost entirely to the time resolution of the detector and electronics setup, which for 150 torr is 6.0 ± .8 ch or 90 ± 12 ns, measured from the average for the high energy peaks. Had the width been due mainly to μ stop times, the 70 torr peaks would have been about twice as wide as the 150 torr peaks.

The zero time of muons passing through scintillator T3 was found using the two CH_4 time peak positions, and,the relation of the stop time being inversely related to the gas pressure. The actual pressures for the nominal 150 torr measurements are 149 and 145 torr, with about an equal amount of data coming from each of these pressures, averaged this gives 147 torr. The actual pressure of the 70 torr run was 71 torr. If the stopping time is inversely proportional to the pressure then,

$$T = \frac{K}{P} \tag{4.4}$$

so,

$$\frac{T_{71}}{T_{147}} = \frac{P_{147}}{P_{71}} \tag{4.5}$$

There is an arbitrary offset T_0 included in the measurement times T, $T=T_0+T'$. With Eq 4.5 this leads to,

$$T_0 = \frac{T'_{71}P_{71} - T'_{147}P_{147}}{P_{71} - P_{147}} \tag{4.6}$$

so $T_0 = 14.3 \pm .7$ ch. The average stop times for the two pressures are therefore, $9.3 \pm .8$ ch and $18.3 \pm .8$ ch, which are 140 ± 10 ns and 280 ± 10 ns for 147 and 71 torr respectively. Both are consistent with what is expected for stop times from monte-carlo simulations of the cyclotron trap[31].

F. Fitting of μC Transfer Data

In section D, evidence for muon transfer in the deuterium - methane mixture is visible in the form of trails of μC x-ray events following the prompt event peaks. More quantitative information can be found by fitting the time structure of the μC trails, including 1) the transfer rate, 2) the relative yields of the μC cascade x-rays after transfer, and 3) the initial population of the μC after transfer. The paucity of data makes fitting the 2-D spectra as a whole with a combination of peak, trail and background functions, impracticable. Instead it was decided to first fit the background events separately, then make energy cuts in the 2-D data around the μC events -- similar to what was done with the prompt peak fits -- producing time spectra of all the μC events, including the prompt, delayed and background events. The 2-D background function resulting from the background fit was then used to calculate the 1-D backgrounds in these time spectra. The 1-D backgrounds were then were subtracted from the time spectra, leaving prompt and delayed events only. These were fitted, and the resulting parameters used to calculate the values of the transfer rate and cascade populations.

F. 1. Fitting the Background

The background of the transfer data is sparsely populated with events (See Fig. 5-2c), which makes it difficult to use the least squares method for fitting. The use of the least squares method requires that the data be sorted into bins with no fewer than five events[32]. This would roughly require bins 15 x15 (256 x 256) channels in size, which would be considerably larger then the width of the trails, which on this scale are about three channels wide. Such a large binning size would include great numbers of background events in the same bins as the muonic x-ray events, and yield relatively large fit parameter uncertainties because of the low statistics. A different method was therefore used, that of the maximum likelihood method[33], which is specifically designed to be used with sparse data.

The maximum likelihood method does not require binning of the data. Instead, it is a method of fitting a previously known probability distribution function (pdf) to a continuous set of data. The pdf, as its name implies, is a function which describes the probability of finding an event at a specified set of coordinates, in this case the energy and time of the background events. The pdf can therefore be thought of as a surface over the energy vs time plane, with the height of the surface (the value of the pdf) at a point representing the probability for an event at that point. The pdf involves a number of parameters, which are adjusted to find the best fit of a function to the data. Therefore, the pdf can conversely be thought of as a function of the parameters at fixed coordinates of energy and time, for which the probability now forms a surface in parameter space. This surface will have a maximum at the values of the parameters for which the probability to produce the measured event is greatest. Each event in the data set therefore has a corresponding pdf as a function of parameter space, and for that pdf a best set of parameters that maximizes the probability of producing the event.

In the maximum likelihood method a Likelihood Function is constructed by multiplying all the pdfs for the data together, thus creating the probability for generating the entire data set as a function of the parameters. The logarithm of this product is then calculated, and the result is the likelihood function in parameter space. In practice this is done by taking the logarithm of each individual pdf and summing them. The Likelihood Function is assumed to be well behaved, and has an absolute maximum as a function of the parameters for a fixed data point value. Since the Likelihood Function is the logarithm of a function, its maximum occurs at the same point as for the total probability function itself. This maximum represents the combination of parameter values that produces the greatest probability of generating the given data set using the specified pdf. Therefore these values are taken to be the best for the parameters, hence the name maximum likelihood method.

The transfer data set (See again Fig. 4-2c) is not composed only of background events, but also includes the desired μC and μd events and other identifiable event peaks, for example the electronic Cu x-rays. Fitting of the background required first separating the background events from the identifiable peaks, to leave a pure background data set. The identifiable peaks were eliminated by making energy-time cuts, which are simple rectangular regions, around the identified peaks. The cuts in energy were centered on the peak centers and had widths of $\pm 2\sigma$, which were taken from the 1-D energy spectrum fits. The time cut for the μC events covers all time from channels 0 - 8192 (8192), to eliminate all possible prompt and delayed events. The μd and μC 5-4 events were eliminated by cutting all events below energy channel 887 (8192). The prompt peak at channel 795.8 (1024), which is most likely the μAl 4-3, was removed by cutting in time from 0 to channel 1024 (8192). The time limit for this cut was determined by choosing the delayed energy spectra time cut for which the signal to noise for this peak fell to below 2/1. The prompt electronic x-rays were eliminated in a similar way, with a cut in time ch 0 -1408 (8192) and energy ch 1762 - 2690. There is also a trail of electronic copper events and this was covered by cutting all events with that energy, ch 2056 - 2421. A plot of the data with the cuts made is shown in Fig. 4-8.

The fitting of the pdf to the background data, was done by means of the CERN Library program MINUIT[44], which is a non-linear parameter search routine to find the minimum (or maximum) of a user specified function. MINUIT requires the user to write a functional subroutine that will accept parameter values from MINUIT and return the function value, the likelihood function in this case, back to MINUIT. It also requires an initial guess of values for the parameters to begin the fitting process.

Before the fitting of the real background data was done, several test cases were run to see if the maximum likelihood method worked well when applied to this situation and to compare the results of a MINUIT fit to a known analytical fit.

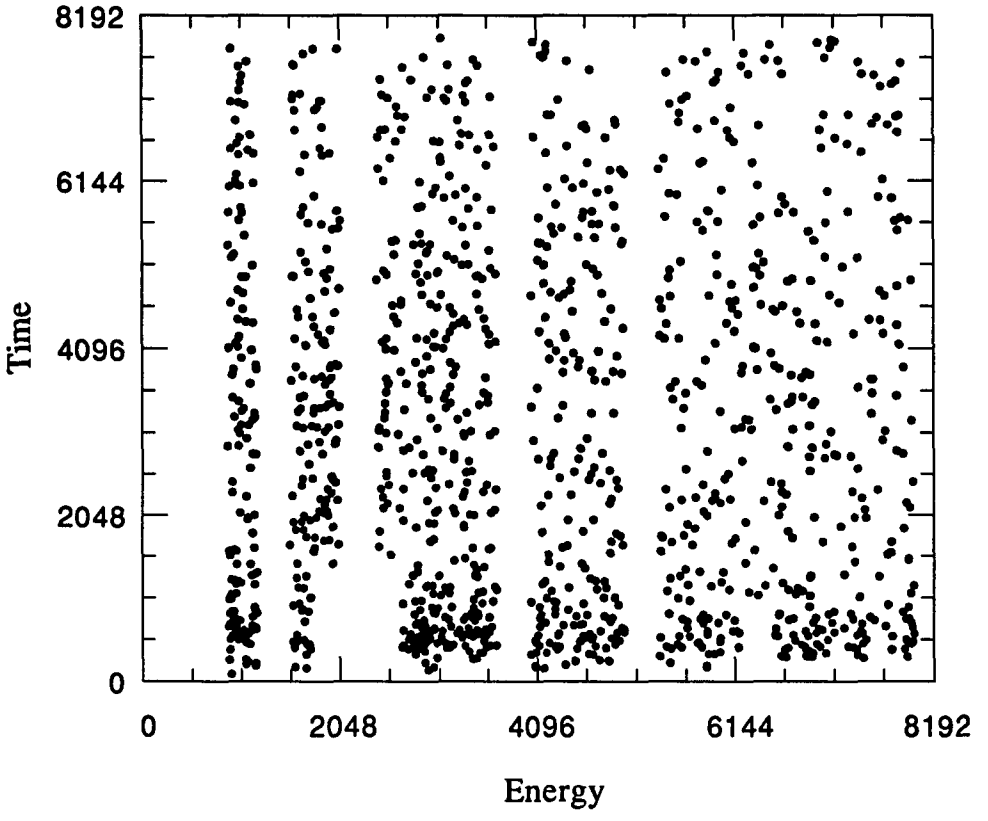

Figure 4-8 Background used to find fitted parametersfor tevt2 background

The known test function was a 2-D exponential decay over a finite region, which was normalized over several regions -- several regions will eventually be produced by the exclusion of the known peak regions -- which gives,

$$f(t,E|\tau,\varepsilon)=\frac{\frac{1}{\tau\varepsilon}\,e^{\frac{-t}{\tau}}\,e^{\frac{-E}{\varepsilon}}}{\sum_{j=1}^{n}\left(e^{\frac{-T_{Uj}}{\tau}}-e^{\frac{-T_{Lj}}{\tau}}\right)\left(e^{\frac{-E_{Uj}}{\varepsilon}}-e^{\frac{E_{Lj}}{\varepsilon}}\right)} \quad (4.7)$$

where E_U, E_L, T_U, T_L are the upper and lower limits of the n rectangular energy vs time regions of the fit. There are two independent exponential decays, one for time and one for energy, creating a decreasing event density with both increasing time and energy. this function is roughly similar to the real background.

A program, (Synexp.f) was written to create simulated data for this pdf. Four sets of simulated data were created of 2000 points each, which is approximately the number of points in the background of the real data. The best parameters are solved for by taking the logarithm of the function and then setting the partial derivatives with respect to τ and ε equal to 0, giving

$$\hat{\tau}=\bar{t}-\frac{\sum_{j=1}^{n}\left(T_{Uj}e^{\frac{-T_{Uj}}{\tau}}-T_{Lj}e^{\frac{-T_{Lj}}{\tau}}\right)\left(e^{\frac{-E_{Uj}}{\varepsilon}}-e^{\frac{E_{Lj}}{\varepsilon}}\right)}{\sum_{j=1}^{n}\left(e^{\frac{-T_{Uj}}{\tau}}-e^{\frac{-T_{Lj}}{\tau}}\right)\left(e^{\frac{-E_{Uj}}{\varepsilon}}-e^{\frac{E_{Lj}}{\varepsilon}}\right)} \quad (4.8)$$

$$\hat{\varepsilon} = \bar{E} - \frac{\sum_{j=1}^{n} \left(e^{\frac{-T_{Uj}}{\tau}} - e^{\frac{-T_{Lj}}{\tau}} \right) \left(E_{Uj} e^{\frac{-E_{Uj}}{\varepsilon}} - E_{Lj} e^{\frac{E_{Lj}}{\varepsilon}} \right)}{\sum_{j=1}^{n} \left(e^{\frac{-T_{Uj}}{\tau}} - e^{\frac{-T_{Lj}}{\tau}} \right) \left(e^{\frac{-E_{Uj}}{\varepsilon}} - e^{\frac{E_{Lj}}{\varepsilon}} \right)} \qquad (4.9)$$

where

$$\bar{t} = \frac{1}{n} \sum_{i=1}^{n} t_i \qquad \bar{E} = \frac{1}{n} \sum_{i=1}^{n} t_i \qquad (4.10)$$

Notice that both τ and ε appear on the right hand side of the equations, so these are coupled equations that need to be solved iteratively. A program (Iterate.f) was written to do the iteration steps for this Likelihood function, and with this program the parameters for the four simulated data sets were found (See Table 4-11).

All the fitted parameters are lower than the actual values from the simulated data, but may still be acceptable values once the uncertainties for these values are found numerically using MINUIT. This bias is caused by the data ranges being cut off at 8192 channels, since the same pdf, with the upper limit allowed to go to infinity, has values

Table 4-11 Fits of synthetic test data using iterative analytical method.

Test Set	Input τ	Input ε	Fitted τ	Fitted ε	Number of Iterations
1	3400	2900	3255.1	2736.7	100
2	6800	5800	6275.7	5203.6	200
3	13600	11600	11663.0	9461.7	500
4	1000	500	975.64	485.88	100

generated by the fit that are unbiased estimators of its parameters[33]. This is seen in the better accuracy of the fits for the smaller parameter values.

A subroutine, mlfcn.f, was written to calculate the above Likelihood function for MINUIT to use in its parameter search, and was then run on the same four simulated data sets that were fitted with the iterative analytical routine. The parameters resulting from this fit (See Table 4-12) show excellent agreement with those from the iterative analytic method, demonstrating that MINUIT works well for fitting these slowly varying backgrounds. MINUIT also produces the uncertainties for the parameter values, which are equivalent to a $\pm 1\sigma$ range, where σ, the standard deviation, is defined in the usual way. The actual values don't quite fall into these ranges, but rather are all slightly above, at approximately + 1.3 σ, which is due to the bias mentioned above. The real data set however, has many excluded regions that will alter the fit and change the direction of the bias.

To test for a change in bias due to the excluded regions, the simulated data were sorted to eliminate the excluded regions, and were fitted as above using MINUIT (See Table 4-12). The true values were now covered much better by the range of uncertainties, but the fitted values were still biased slightly low. Although they were not Table 4-12 Fits of synthetic test data using MINUIT, with and without excluded regions.

Test Set	Input		Fit with Excluded Regions		Fit without Excluded Regions	
	τ	ε	τ	ε	τ	ε
1	3400	2900	3255.1 ± 86.3	2736 ± 115.8	3202.7 ± 156.0	2792.6 ± 127.3
2	6800	5800	6275.5 ± 388.2	5203.3 ± 271.8	6199.2 ± 487.0	5394.1 ± 396.7
3	13600	11600	11664 ± 1302	9463.7 ± 862.8	11383 ± 1534	9087.5 ± 1057.3
4	1000	500	975.6 ± 22.0	485.9 ± 10.9	974.4 ± 67.6	526.7 ± 35.1

completely within the range of the uncertainties, the true and fitted values agreed well enough for the purpose of finding the background function for this analysis. In principle no bias is desired in the parameters; however, when the background subtraction was finally done the uncertainties in the background values were almost an order of magnitude smaller then the data uncertainties, so the bias contributed trivially to the uncertainties of the final data values. The maximum likelihood method was therefore deemed acceptable for this analysis, with the bias considered, for use in fitting the real data.

In the maximum likelihood method, the pdf function is assumed to be known apriori for the data to be fitted, and the parameters of that function are then determined by the optimal fit. In this case, the background function is completely unknown, so a function to model the background must be carefully chosen. The exponential shape can reasonably model the change of the background in the energy direction, because it is a slowly decreasing function of energy. The background in the time direction is much more complicated due to the prompt event structure. A time spectrum of the background was created by making an energy cut through a section from ch 78 -116 (256) between the electronic x-rays and the μC 3-2 line, which showed approximately the shape of the

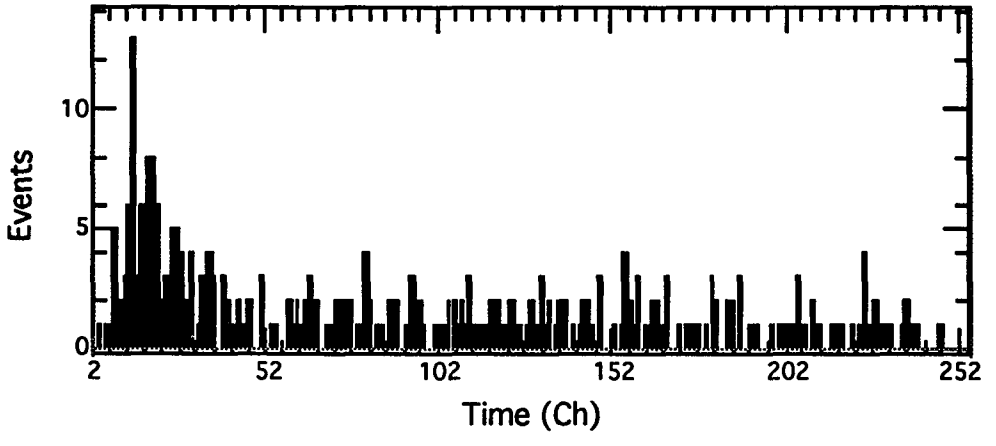

Figure 4-9 Time spectrum of section of bacground from mixture data

background in the time direction. The background has a peak at early times, due to Compton and random prompt events, and a broad base which slowly decreases with time (See Fig. 4-9). This suggested using a Gaussian on top of an exponential to fit the time structure of the background.

A normalized pdf containing an exponential and a Gaussian was created,

$$f(t,E|t,e,A,t_0,a) = \frac{\left(\frac{1-A}{\tau}\, e^{-t/\tau} + A\, e^{\frac{-(t-t_0)^2}{2a^2}}\right)\frac{1}{e}e^{-E/\varepsilon}}{\sum_j \left\{ \begin{array}{l} (e^{-E_{Lj}/\varepsilon} - e^{-E_{Uj}/\varepsilon}) \bullet \\ \left[(1-A)(e^{-T_{Lj}/\tau} - e^{-T_{Uj}/\tau}) + \sqrt{2\pi}\,\alpha\left(\mathrm{erf}\left(\frac{T_{Uj}-t_0}{\sqrt{2}\alpha}\right) - \mathrm{erf}\left(\frac{T_{Lj}-t_0}{\sqrt{2}\alpha}\right)\right)\right] \end{array} \right\}} \qquad (4.11)$$

where erf is the error function and E_U, E_L, T_U, and T_L are the upper and lower limits of the energy and time regions of the fit. t_0 is the mean, α is the width of the Gaussian, and A is the proportion of Gaussian component in the time structure, which is a fraction between 0 and 1. A new subroutine, mlexpg.f, was created with this pdf for MINUIT to use in fitting.

The synthetic data program was also modified to generate data with the above pdf (Eq 4.11), to test the fitting, and four sets of synthetic data were created using various values of ε, τ, and A. The synthetic data were fitted using the new Likelihood routine with the excluded regions, and once again the fitted parameters for the exponentials were found to be slightly, but not unacceptably, low. The other parameters were fitted nicely, so overall the fit was found to be acceptable. The true and fitted parameters for one of the sets are shown in Table 4-13.

Table 4-13 Fit of synthetic test data including a Gaussian, using MINUIT without excluded regions.

	τ	ε	α	t_0	A
Input Values	8000	6000	125	600	.50
Fitted Values	7060.3 ± 841.77	5440.1 ± 419.34	125.03 ± 9.28	600.22 ± 10.01	.4869 ± .0169

The background data, with the excluded regions removed, were fitted with a likelihood function constructed of the above pdf (Eq. 4.11). The results for the fitted values of parameters are listed in Table 4-14. The pdf, using these parameter values, was therefore the best representation of the background in the fitted region. Although the background was fitted only over partial regions of its domain (excluding regions where known lines occur) the fitted function is assumed to be valid over the entire region within the energy and time range. This continuation of the pdf from the fitted regions through the excluded regions was the method used to find the values of the background in the excluded regions. The background function in the excluded regions was then used to calculate the background under the μC lines.

After fitting the background data, a test was performed to see if this fit was statistically acceptable. The Kolmagorov - Smirnov test in two dimensions, which is the most commonly used test of goodness of fit for continuous variables, was used to calculate the probability of the background pdf adequately fitting the data. More specifically this test determines the probability that the specified pdf produced the given

Table 4-14 Fit of transfer data background from run transEvt2, using MINUIT with function mlfuncg, without excluded regions.

	τ	ε	α	t_0	A
Fitted Values	9825.1 ± 1484.1	6615.7 ± 573.2	174.46 ± 16.09	590.26 ± 18.66	.40714 ± .0190

data set. A high probability indicates good likelihood that the model produced the data being fitted, and this is interpreted to mean the model fitted the experimental data well.

The Kolmogorov - Smirnov (KS) test in one dimension[33] is relatively well known, and its properties, such as the KS statistic D for one dimensional spectra being independent of distribution shape, are well defined. Its extension to 2-D is a relatively recent aceivement[36], and the properties of the 2-D version are not rigorously defined.

In 1-D case, The KS statistic D is the maximum of the differences calculated by subtracting the model's cumulative probability of an event occurring in the region greater than a point specified by a data value, from the fraction of data events in that region, where this difference is calculated for all data events. The cumulative probability is calculated by integrating the model pdf from the specified point to the maximum of the domain of the variable. In 2-D, this cumulative probability is not well defined, since unlike the 1-D case, where the integral is completely specified by the starting point, the integral through the 2-D region depends arbitrarily on the path of integration. Instead, the cumulative probability is taken to be the integrated probability in each of the four quadrants around a given data point. This method assumes that the domain of the pdf is a rectangle, therefore any specified point separates the region into four quadrants, with the point being at the intersection of the dividing lines parallel to each of the axes. The KS statistic D, is then defined as the maximum of the differences of total integrated probability in a quadrant and the total fraction of data points occurring in a that quadrant, where the differences for all data events are calculated. Often in practice two distributions of events are compared to see if they are produced from the same parent distribution (pdf) rather than comparing one distribution of data to a known pdf. In this case the statistic D is the maximum difference in the number of events in all possible quadrants for the two data sets being compared.

From this value of D, a probability of obtaining these data from the pdf is calculated from the distribution function of D, and this is interpreted as the probability

that the two data sets came from the same parent distribution. Unfortunately, in the case of a 2-D pdf the distribution of D is not independent of the shape of the pdf, therefore the probability is not uniquely defined. However, extensive monte-carlo tests have shown that the distributions of D were nearly identical if both data sets being compared had the same correlation coefficient r. This correlation coefficient is the commonly used linear correlation coefficient, sometimes known as Pearson's r.

The real background data and the synthetic background data generated from the pdf were compared using the KS 2-D test. The region for this comparison is the rectangular energy vs. time range of the ADCs with the excluded regions taken out. Although the region fitted needs to be a continuous rectangle for this method to work, these excluded regions were not a problem, since this was equivilent to having the probabilities in the excluded regions defined to be zero. The rectangle is therefore a continuous region with probability well defined throughout, which can be used by the KS 2-D method.

The need to cut the excluded regions from the total range of the background made it very dificult to compare the actual pdf to the background data. Integrations of the pdf through regions that included part of an excluded region would have been difficult and taken much time computationally. Instead synthesized data created from the fitted background pdf were used for the KS 2-D test. This comparison of real data to synthesized data was much simpler than a real data to model comparison, and was made just as accurate by increasing the number of synthetic data points generated to be much greater than the number of points in the background data. In this way the statistical uncertainty is mainly from the real data, while the uncertainty of the synthesized data becomes insignificant.

A synthetic data set was generated from the background function with two thousand points (See Fig. 4-10) in the fitted regions for visual comparison with the real background. The synthetic data appears very similar to the real background (See Fig. 4-

8). A second set of 32,000 points, which is more than eight times the number of real data background events, was generated for comparison to the real data background using the KS 2-D test. A K-S 2-D test was run with the data and synthetic data resulting in linear correlation coefficients that were the same for both of the data sets, so this test should be accurate for these data. The quality of fit at 4.6% while not great, was considered acceptable for the purpose of generating background values for this analysis.

F. 2. Fitting the μC Trails

With the background fitted, the next step of the analysis was to fit the time structure of the trails of the μC lines. Time spectra were first constructed from the μC events by making energy cuts around the μC x-ray events in the 2-D energy - time spectrum of the transfer data. These cuts extended from the peak centers, which were determined from the energy spectrum fit (See Table 5-6), up to $+2\sigma$ and down to -3σ of the peak widths. The high side limit was chosen because at this value a Gaussian, for which the Silgard3.ST peak shape is a good approximation on the high side, has ≈ 90% of its area enclosed. Also, the background and the peak became comparable at this distance from the peak centroid. The -3σ cut ensured that the low end tail of the peak shape was included in the cut, which was desirable since the tail contains ≈ 10 % of the peak events. The background also became comparable to the peak tail at this lower limit. The regions of the cuts were then projected onto the time axix to create 1-D time spectra.

Fitting the time structure of the trails once again came down to a choice of fitting continuous data using the maximum likelihood method or binning the data and using the least squares method. In this case it was decided that there were enough events in the trails to be successfully binned and fitted by the least squares method. With 16 bins it was estimated from the time spectra that the average bin would contain about 7 events, which given the previous arguments about binning should be adequate. Also, if there

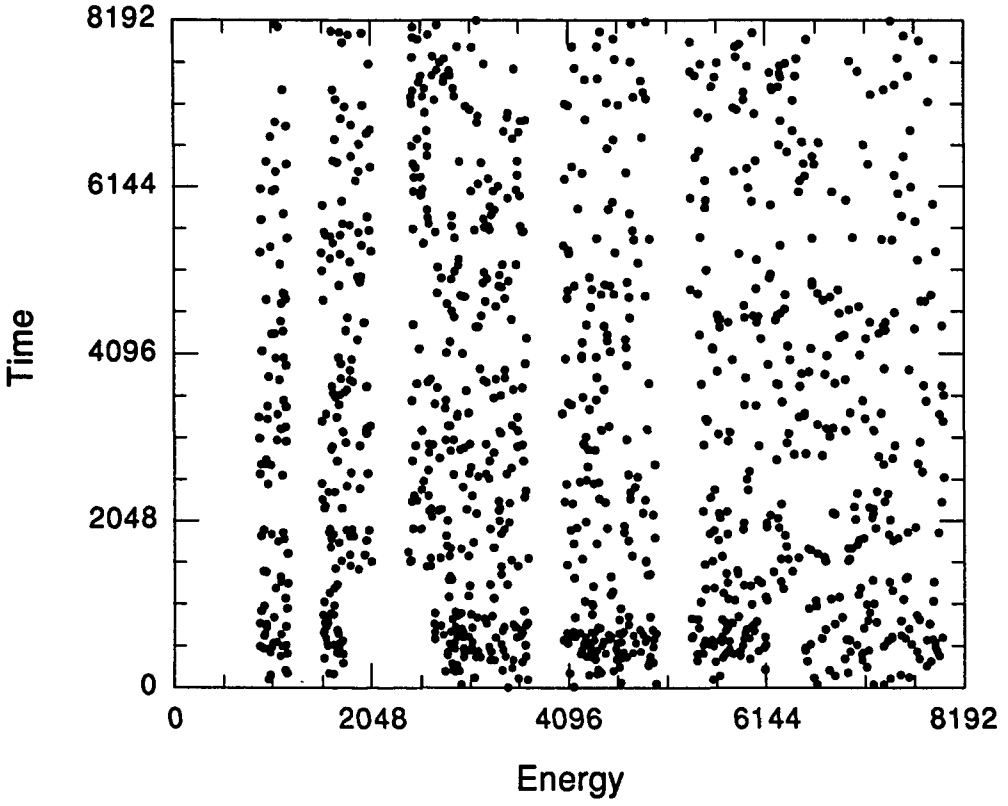

Figure 4-10 Synthesized background from fitted background model.

were so few events in the trails that the maximum likelihood method was necessary, no meaningful information could likely be extracted from this data.

The backgrounds under the μC trail time spectra were calculated using the background pdf fitted previously. The pdf was integrated in energy and time over the rectangular regions of the bins to find the total probability of a background event in each of the bins. The integrated probability function is,

$$f = (1-A)\, f_1 + A\, f_2 \tag{4.12}$$

where f is the probability of finding an event in a given bin and f_1 and f_2 are,

$$f_1 = \frac{\left(e^{\frac{-a}{\varepsilon}} - e^{\frac{-b}{\varepsilon}}\right)\left(e^{\frac{-c}{\tau}} - e^{\frac{-d}{\tau}}\right)}{\sum_j \left\{ \begin{array}{l} (e^{-E_{Lj}/\varepsilon} - e^{-E_{Uj}/\varepsilon}) \bullet \\ \left[(1-A)(e^{-T_{Lj}/\tau} - e^{-T_{Uj}/\tau}) + \sqrt{2\pi}\,\alpha(\mathrm{erf}(\frac{T_{Uj}-t_0}{\sqrt{2}\alpha}) - \mathrm{erf}(\frac{T_{Lj}-t_0}{\sqrt{2}\alpha}))\right] \end{array} \right\}} \tag{4.13}$$

$$f2 = \frac{\left(e^{\frac{-a}{\varepsilon}} - e^{\frac{-b}{\varepsilon}}\right)\left(\mathrm{erf}\left(\frac{d-t_0}{\sqrt{2}\,\alpha}\right) - \mathrm{erf}\left(\frac{c-t_0}{\sqrt{2}\,\alpha}\right)\right)}{\sum_j \left\{ \begin{array}{l} (e^{-E_{Lj}/\varepsilon} - e^{-E_{Uj}/\varepsilon}) \bullet \\ \left[(1-A)(e^{-T_{Lj}/\tau} - e^{-T_{Uj}/\tau}) + \sqrt{2\pi}\,\alpha(\mathrm{erf}(\frac{T_{Uj}-t_0}{\sqrt{2}\alpha}) - \mathrm{erf}(\frac{T_{Lj}-t_0}{\sqrt{2}\alpha}))\right] \end{array} \right\}} \tag{4.14}$$

with variables defined as in Eq 4.11. The uncertainties for the background values were also calculated using the propagation of uncertainties equation[37],

$$\sigma_f^2 \approx \sigma_\varepsilon^2\left(\frac{df}{d\varepsilon}\right)+\sigma_\tau^2\left(\frac{df}{d\tau}\right)+\sigma_\alpha^2\left(\frac{df}{d\alpha}\right)+\sigma_{t_0}^2\left(\frac{df}{dt_0}\right)+\sigma_A^2\left(\frac{df}{dA}\right) \tag{4.15}$$

The pdf integrated over a bin gives the probability of finding a background event in that bin for only one event generated in the entire data set. Since many more background events occur expectation values for the bins must be calculated by scaling probability to the actual number of events fitted in the background, in this case 1243 ± 35 events. The expectation values then become the total number of background events expected in each bin.

In light of the somewhat poor quality of fit of the background function, with a goodness of fit 4.6%, it was decided to make a test by fitting a section of data that contained only background events in hopes of finding where the fit was poor. The energy cut for this time spectrum was made from ch 78 to 116 (256) in the region between the electronic copper x-rays and the μC 3-2 events (this is the same region used to estimate the shape of the background time structure). This was compressed into a 1-D time spectrum and binned into 16 channels. Background values were then calculated for these bins and the values compared to the data (See Table 4-15). All the values, except that of the second bin, were in good agreement with the data. The range of the data does not extend to the full range of the ADC channels causing the last bin to not be completely determined, so it is ignored. The second bin is at the location of the prompt events peak, thus suggesting that the difficulty with the fit is that the pdf's Gaussian function does not represent the prompt background well. Fortunately, the background in the region of the delayed trail events is fitted well, so this difference in agreement of the prompt events did not affect the fitting of the trails and therefore the transfer data. Since fitting of the delayed trail events was the purpose of finding the background no improvement of the background function was deemed necessary.

Table 4-15 Data of test fit of background function to section of background data, uncertainties of background data equal the square root of the value.

Bin	Background Data	Generated Background Values	Uncertainties of Generated Values
1	36	46.9	3.7
2	71	38.3	3.3
3	26	22.8	1.2
4	11	21.7	1.0
5	21	20.6	0.9
6	19	19.6	0.8
7	18	18.6	0.7
8	14	17.6	0.6
9	20	16.7	0.6
10	18	15.9	0.7
11	16	15.0	0.7
12	14	14.3	0.7
13	12	13.6	0.8
14	10	12.9	0.8
15	15	12.2	0.8
16	2	11.6	0.9

The 1-D time spectra of the μC trails were binned into 16 bins each and the background values for these bins calculated using the normalized background pdf. These background values were then subtracted from the time data to find the μC event time spectra values.

F. 3. Transfer Rate

The transfer rate is simply considered another disappearance rate for the μds. The total disappearance rate is given by,

$$\frac{dN_{\mu}}{dt} = Ae^{-(\lambda_{,}+\lambda_{0}+\lambda_{,})t} \tag{4.16}$$

where λ_t is the transfer rate from deuterium to carbon, λ_0 is the muon decay rate, which is accurately known, and λ_τ is the disappearance rate due to the remaining competing processes described in the theory section. The competing rates, which are all less than $\approx 10^3$/sec for the conditions of this experiment, are much less than the anticipated rate of $\approx 10^6$/sec for the transfer rate. Also, the uncertainties of the data were much greater than the differences due to the competing disappearance effects, so they were ignored in the fitting of the transfer data. This leaves only the transfer and muon decay rates to describe the data.

It is convenient to first remove the effect of muon decay from the data before further analysis is done, since the decay rate is a known constant for all the data. The muons after this are conventionally known as "non-decaying muons" since the data appears as it would if muons were stable particles.

First a test to see if the midpoint of the bins can be used to calculate the decay factor was made. The mean decay factor calculated over the bin length is 243ns

$$d_{\text{mean}} = \frac{-\tau\int_a^b -\frac{1}{\tau}e^{\frac{-t}{\tau}}dt}{b-a} = 0.9467 \tag{4.17}$$

for a =0, b= 243ns and τ = 2197ns, the lifetime of the muon, and compared to the midpoint value,

$$d_{\text{mid}} = e^{\frac{-(b-a)}{2\tau}} = 0.9462 \tag{4.18}$$

The difference is only in the fourth decimal place, so the midpoint method is acceptable.

The μC event data were then corrected for decay by dividing the data values in each bin by the decay factor, $decay_k$, calculated from the midpoint of the bin.

$$decay_k = \exp(-(243\,k - 121.5)/2197), \quad k = 1,\ldots,16 \tag{4.19}$$

Table 4-17 Muon decay corrected transfer trails data for the three μC lines and their sum.

Time (ns)	Bin	4-3	3-2	4-2	sum
121.4	1	-2.79 ± 5.16	1.40 ± 4.69	-5.93 ± 3.20	-7.32 ± 7.67
364.3	2	59.6 ± 10.0	85.4 ± 11.0	29.4 ± 7.17	174.5 ± 16.5
607.2	3	23.7 ± 7.16	31.5 ± 7.48	1.81 ± 3.76	57.0 ± 11.0
850.1	4	12.6 ± 6.5	15.1 ± 6.3	15.8 ± 6.1	43.5 ± 10.9
1093	5	-3.19 ± 4.71	20.8 ± 7.4	6.62 ± 5.22	24.3 ± 10.2
1335	6	4.72 ± 6.43	14.8 ± 7.1	6.11 ± 5.52	25.6 ± 11.1
1578	7	2.15 ± 6.55	15.2 ± 7.7	3.32 ± 5.44	20.7 ± 11.5
1821	8	12.6 ± 8.6	6.28 ± 6.89	-0.25 ± 5.14	18.6 ± 12.2
2064	9	2.38 ± 7.75	7.83 ± 7.70	13.2 ± 8.1	23.4 ± 13.6
2307	10	-7.60 ± 6.50	1.03 ± 7.03	3.99 ± 7.02	-2.58 ±11.87
2550	11	2.33 ± 9.13	8.45 ± 9.06	5.21 ± 7.84	16.0 ± 15.0
2793	12	-3.21 ± 8.86	6.84 ± 9.48	-11.2 ± 3.6	-7.60 ±13.48
3036	13	5.78 ± 11.40	24.6 ± 13.2	20.2 ± 12.0	50.5 ± 21.2
3279	14	3.48 ± 11.93	6.32 ± 10.97	-3.28 ± 7.77	6.53 ± 18.0
3522	15	10.4 ± 14.2	-1.72 ± 10.04	-2.72 ± 8.70	5.99 ± 19.46
3764	16	-14.4 ± 10.0	-17.3 ± 5.8	-13.1 ± 5.7	-44.9 ± 12.9

The data of the μC trails before and after muon decay corrections are listed in Table 4-17 for the three sets.

With the decay rate removed the data are now described solely by the transfer rate λ_t,

$$\frac{dN_\mu}{dt} = Ae^{-\lambda_t t} \tag{4.20}$$

where N_μ is the number of "non-decaying" μds remaining, λ_t is the transfer rate and A is a constant.

The data from the three trails were summed to form one set of transfer data to be fitted. This improved the statistics and therefore led to a more accurate fit than if the trails were fitted separately. Summing the data was appropriate for determining the transfer rate since all the trails were assumed to have the same time structure, and because the μC events that were produced in the cascade depended only on the probability for that transition, which is independent of the transfer process itself.

The summed data were then fitted (See Table 4-18 and Fig. 4-11) using a Gaussian function to represent the prompt peak, a Heavyside step function to represent the initial time rise of the transfer curve, and an exponential decay as given in Eq. 4.20 above, which is,

$$N = B\exp\left(-\frac{1}{2}\left(\frac{t}{38}\right)^2\right) + A\exp(-\lambda_t t)(1+\tanh(st)) \tag{4.21}$$

where the prompt peak was centered at t=0, and the width, 38ns, was taken from the prompt peak fit done for the slew data. The value A is the amplitude of the exponential, B is the amplitude of the prompt peak, s is the step parameter that determines how sharp the rise is, and λ_t is the transfer rate. The step function is the same as used in the initial fit of the prompt peaks for finding the time slewing, which was again chosen because it is a good approximation to the integral through a Gaussian. An initial rise of this form is expected for the transfer rate, since the rate is proportional to the number of μds, and the number of μds is proportional to the integral through the prompt peak. This integral is similar for both the μd and μC prompt peaks, since they both have the same time structure. The parameters, B, which represents the height of the prompt peak and s, which is the steepness of the step function have large uncertainties, suggesting that they are of little significance in the fit.

Table 4-18 Parameters from fit of summed μC trails data.

A	B	λ_t (1/sec)	s
35.6 ± 7.6	145 ± 7 x 10^5	(1.03 ± .40) x 10^6	0.036 ± 1400

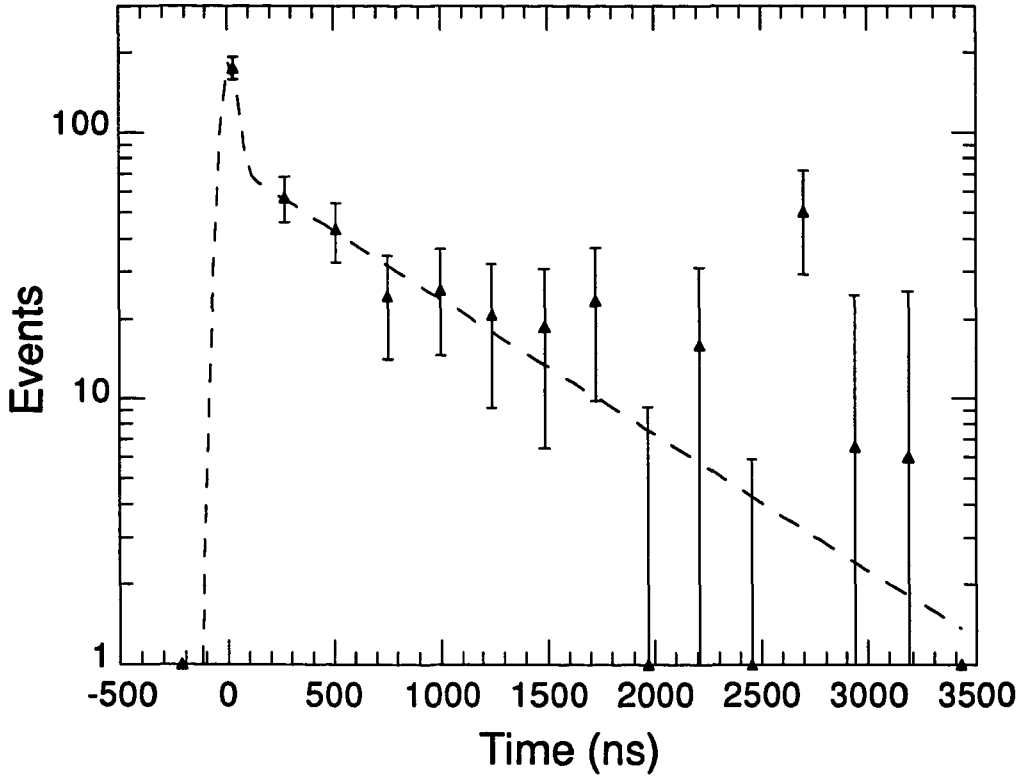

Figure 4-11 Fit of the summed μC trail data.

The transfer rate was then normalized to liquid hydrogen density as is traditional with rates that are proportional to the density. The atomic density of carbon in the gas mixture is, $N_C = 9.65 \times 10^{17}$ atoms/cm^3, so the ratio of liquid hydrogen to carbon density is,

$$R = 4.25 \times 10^{22} / 9.65 \times 10^{17} = 4.40 \times 10^4 \tag{4.22}$$

which leads to a rate at LH_2 density of,

$$\Lambda_t = R \cdot \lambda_t = (4.5 \pm 1.8) \times 10^{10}/\text{sec} \tag{4.23}$$

This is in agreement with a similar measurement[38] made at 50 times greater pressure and a carbon concentration of ≈0.1%, where a LH_2 normalized rate of $(5.1 \pm 1.0) \times 10^{10}$/sec was measured.

A fit of the summed data from the three μC trails provided the transfer rate, but yields of the individual trails were also desired. The three trails were fitted individually using the same function as the summed data, only for these fits the transfer rate, λ_t, and the step factor, s, are fixed to the values from the summed data fit, since these should be the same for all the data and are therefore best determined from the higher statistic summed data fit. Two parameters were left to be fitted, the height of the prompt peak, B, which was not a meaningful value since the background function is a poor representation of the background under the prompt peaks, and the amplitude of the transfer curve, A, which gave the relative yields of the lines. The yields of the trails are proportional to the total number of events in the trails, and the number of events are proportional to the A's, which can be seen from the integral,

$$\int_0^\infty A e^{-\lambda t} dt = \frac{A}{\lambda} \tag{4.24}$$

It was not possible to calculate absolute yields for these lines, because the solid angle between the detector and the events was not known.

It was first necessary to find the relative energy efficiencies among the μC lines before the relative yields among the three lines were calculated. An accurate relative efficiency plot does exist for the Silgard detector from a previous experiment[39]. This is unfortunately a plot of efficiency values of various calibration source lines and not a function or even a table of efficiency values, so the values had to be graphically extracted

from the plot. The source line efficiencies were successfully extracted along with the associated uncertainties. These values were then fitted with a function created for this purpose, which was adapted from similar efficiency functions used in reference 26, of the form,

$$\varepsilon = a\ln\left(\frac{E}{b}\right)\left(1-\exp\left(cE^{d}\right)\right)+f\cdot E \qquad (4.25)$$

where ε is the efficiency, E the energy and a, b, and c are parameters of the fit. From this function, the relative efficiencies and their uncertainties for each μC x-ray energy were calculated.

A related factor affecting the relative yield is self absorption of the x-rays in the target gas, which was calculated and found to be insignificant even for the low energies of the μd x-rays.

The ratios of yields are found by,

$$R_{\frac{1}{2}} = \frac{A_1}{A_2}\cdot\frac{\varepsilon_2}{\varepsilon_1} \qquad (4.26)$$

where A is the raw yield amplitude and ε is the energy efficiency for that line. These are shown in Table 4-20.

Table 4-20 Yield ratios for μC lines from Silgard detector.

Ratios
$\frac{4-3}{3-2}=\frac{7.6}{18.8}\cdot\frac{63.0}{59.0}=0.43\pm0.16$
$\frac{4-2}{3-2}=\frac{4.0}{18.8}\cdot\frac{63.0}{67.4}=0.20\pm0.14$
$\frac{4-2}{4-3}=\frac{4.0}{7.6}\cdot\frac{59.0}{67.4}=0.46\pm0.35$

F. 4. W&M Detector Data

While the Silgard detector covered the energy range from ≈2 to ≈30 KeV, and included the major μC transitions 4-2, 4-3, and 3-2, the μC K-series lines were out of reach of this detector. Additional data were acquired using the germanium detector (W&M) opposite to the Silgard detector, which covered a complementary energy region, from ≈30 to ≈120 KeV, including the K-series lines. The data from this detector were recorded on the MCA as 1-D energy spectra only, so no timing information is available for the individual events, and 2-D energy vs. time plots and cuts cannot be made.

Two different gates were used in collecting transfer data on the MCA, 0.5 and 2 μsec long starting from a time before the prompt peaks begin. This choice of gates allowed transfer yields to be calculated from these data when combined with information from the Silgard data. Both data sets using the two time gates were taken with identical conditions, so these data represent two views of the same transfer interactions. Additionally, a proper number of μ-stops was recorded for each set in the form of the scalar $T_3 \cdot RF$ values, which is the number of muons that entered the gas chamber during the run, so a comparison between the two time gate data sets could be made.

These two gate conditions were used to separate the prompt from the delayed events for the W&M data. The first gate started before the prompt events and ended 500ns later, thus completely covering the time region of the prompt peaks. The second gate started at the same time but continued for 2 μsec, thus including the prompt peaks and most of the delayed transfer events. Scaling the two sets of data to equate the number of $T_3 \cdot RF$ counts, and subtracting the data for the first 0.5 μsec gate from the data for the 2 μsec data, resulted in a data set of events between 0.5 and 2 μsec. If the 0.5 μsec gate included all the prompt events then this subtracted set must have contained only delayed

transfer events. The exact position of the prompt peaks had to be found before this was known for certain.

The T_3·RF gate that was used as part of the event trigger for both the Mac and the MCA should, in principle, have started at the same time in both systems, but additional electronics included in the gates for each of these data acquisition systems may have delayed the signal in one with respect to the other. The beginning of the gates for the MCA therefore, may not correspond to the same beginning time shown in the Silgard 2-D plots. However, another fortunate occurrence happened, which showed the time range of the MCA gate in the Silgard data, and allowed an accurate comparison of the two system gates to be made. The 2 μsec MCA gate was used on the Mac during the CH4150Trans% data run while the time gate for the Mac was being constructed. This provided a Mac data set showing the extent of the MCA gate.

The CH4-150Trans% data was resorted into 8192 time channels and projected into a 1-D time spectrum in which the large number of zero energy events provided a sharp marker of the beginning and end of the 2 μsec gate. Events started in time channel 96 and ended in channel 4382 (8192), which corresponds to a time gate of 2034 ns, almost exactly as advertised, and on the scale of the 2-D Silgard data plots ranges from channel 3 to 137 (256). The 0.5 μsec gate was not used in a similar manner on the Mac, so no direct measurement of its position could be made. Instead the width of the gate was assumed to be exactly 1/4 as long as the 2 μsec gate, which was thought acceptable since the delay length was set using a face plate switch, with the time length selected from among discreet values, not a continuous range.

The K-series transitions are due to the same cascade mechanisms as the μC lines measured in the Silgard detector, so the K events should occur at the same time as the lower energy events. The prompt peak centers for the lower energy peaks from the Silgard detector occur 296ns after the start of the MCA gates, so the K-series prompt

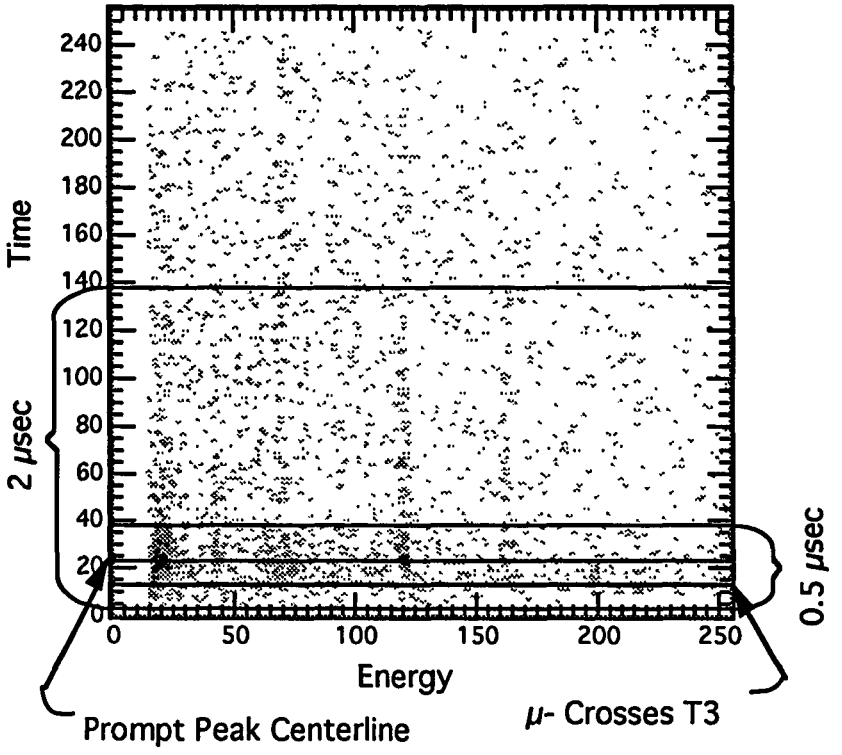

Figure 4-12 MCA Time gates compared to Silgard data.

peaks would therefore also be centered at the same time, and the 0.5 μsec gate continued 213ns later then the peak centers. The resolution of the W&M measured during setup tests was at worst ≈100ns. Therefore, as previously thought, the entire prompt peak should be covered by the 0.5 μsec gate, and only delayed transfer events appeared in the difference set. A plot of the Silgard transfer data, with the MCA gates inserted for comparison, is shown in Fig. 4-12.

F. 5. W&M Calibration

Two energy calibration runs, one using a Co-57 and one a Ba-133 source, were done for the W&M detector when it was first inserted into the cyclotron trap. The major

lines from these two sources covered the range of the μC K-series, which provided an accurate calibration over the whole range of the series. Both calibration spectra were fitted with Gaussian peak shapes using ROBFIT, which produced acceptable fits for the purpose of creating calibration and efficiency functions. The fitted lines and their positions, areas, and probabilities for emission are listed in Table 4-21. The four major gamma ray lines of the two sources were then fitted with a linear function to produce an energy calibration for this detector,

$$E = (ch - b)/m; \quad m = 5.9639 \pm 0.0007, \quad b = -23.01 \pm 0.06 \tag{4.27}$$

where energy E is given in KeV. A plot of this fit is shown in Fig 4-13. The lower energy x-ray lines were not used for the energy calibration since they are below the energy range needed, and their positions were not accurately fitted.

The absolute efficiencies were also calculated for the W&M detector (See Table 4-22), although it was shown later that only a relative efficiency was needed. These values were unusually low for a detector of this type, which normally has a maximum efficiency of over 90% in the 50 to 100 KeV range. The low efficiency may be due to the presence of the magnetic field from the trap. Regardless of this change in total

Table 4-21 Fits of energy calibration peaks of Co-57 and Ba-133 source spectra for the W&M detector.

Source		Energy (KeV)	Position (1024ch)	Area (events)	Probability of emission (%)
Ba-133	x	30.625 + 30.973	-	81181	33.5 + 62.0 = 95.5
	x	35.2	-	40545	22.2
	γ	53.161	294.087 ± .030	10317 ± 118	2.20
	γ	80.998	460.036 ± .013	161181 ± 3620	34.1
Co-57	γ	122.061	704.958 ± .020	35230 ± 276	85.68
	γ	136.474	790.895 ± .049	4062 ± 72	10.67

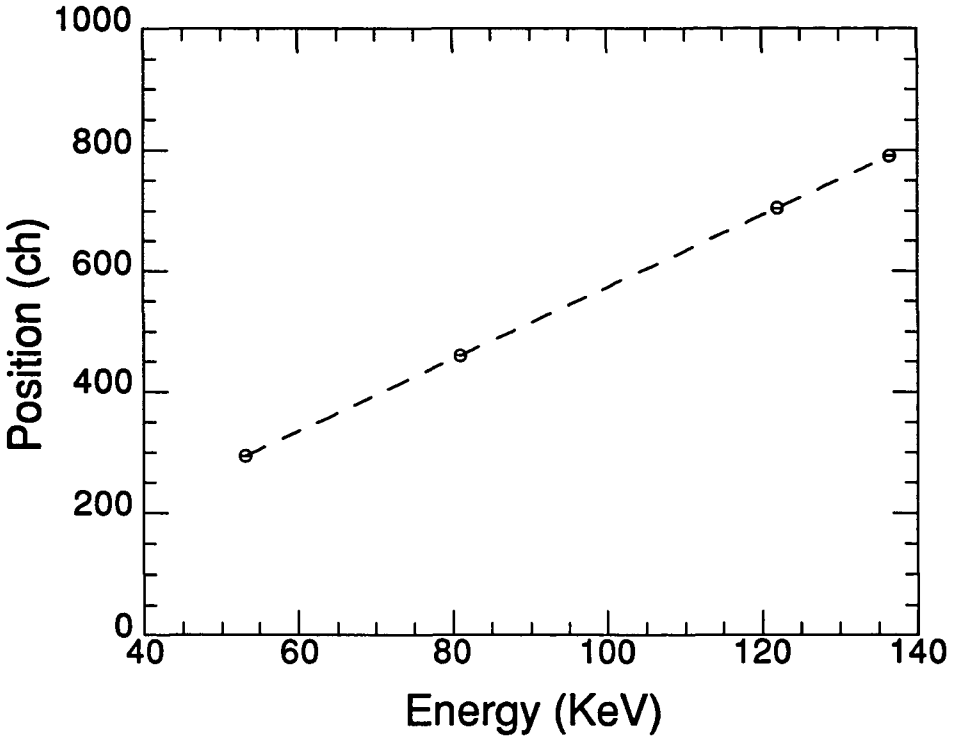

Figure 4-13 Energy calibration for W+M detector.

efficiency, the relative efficiencies were still expected to be accurate since the shape of the efficiency function was as expected.

A suitable function to fit the efficiency values was not found after some effort. Instead, the values of the efficiencies at the μC line energies were extracted graphically from a plot (See Fig. 4-14). This should be accurate, since the slope of the efficiency curve is small in that energy region, and uncertainties of the calibration points are about as large as the variation of efficiency values among the μC lines. The uncertainties of the extracted values derived from the uncertainties of the plotted points were larger then the

Table 4-22 Efficiency values for W&M detector, using Co-57 and Ba-133 sources.

Energy (KeV)	30.85	35.2	53.16	81.00	122.06	136.47
Efficiency	0.0403 ± .0001	0.0866 ± .0004	0.222 ± .002	0.224 ± .005	0.199 ± .002	0.184 ± .003

differences in the extracted values. The difference in detector efficiency among the μC lines was therefore insignificant and was not included in the relative yield ratio calculations.

The energy spectra for the 0.5 and 2.0 μsec time gates were fitted using the same Gaussian peak shape standard that was used for the calibration runs. The scalars T_3·RF were 16573 ± 129 and 30844 ± 176, for the 0.5 and 2 μsec data respectively, where the uncertainties are the square roots of the values. A scaling factor, R = 0.537 ± .005, was created from the ratio of the two T_3·RF scalar values, and was used to normalize the peak

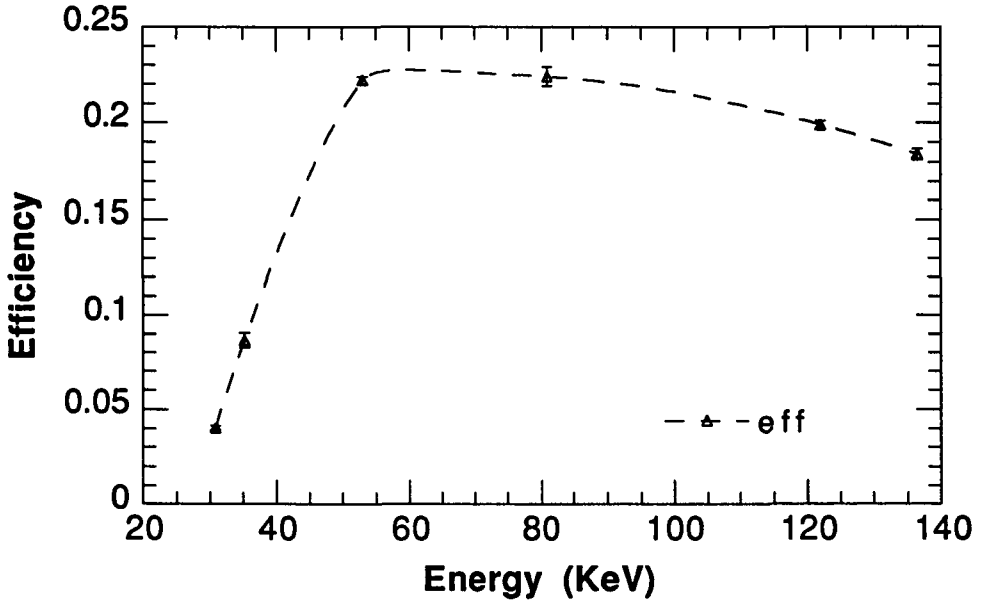

Figure 4-14 Absolute efficiency plot for W+M detector in magnetic field.

Table 4-23 W&M data for 0.5 μsec gate, 2 μsec gate, scaled 2 μsec gate and difference.

R = (T_3·RF 0.5 μsec) / (T_3·RF 2 μsec) = 0.537 ± .005

μC Transition	0.5 μsec Gate	2 μsec Gate	Scaled 2 μsec Gate	Difference, Scaled 2 μsec - 0.5 μsec Gate
2-1	1000 ± 44	4209 ± 96	2262 ± 56	1262 ± 71
3-1	161 ± 24	1319 ± 54	709 ± 30	548 ± 38
4-1	84 ± 20	942 ± 78	506 ± 42	422 ± 46
5-1, etc.	43 ± 19	75 ± 35	40 ± 19	-3 ± 27

areas of the 2μsec data to match the 0.5 μsec data. The peak areas from the 0.5 μsec data were then subtracted from the 2 μsec areas, thus producing the areas of delayed event peaks in the 0.5 to 2 μsec range. The peak areas, scaled peak areas and differences for the two data sets are shown in Table 4-23.

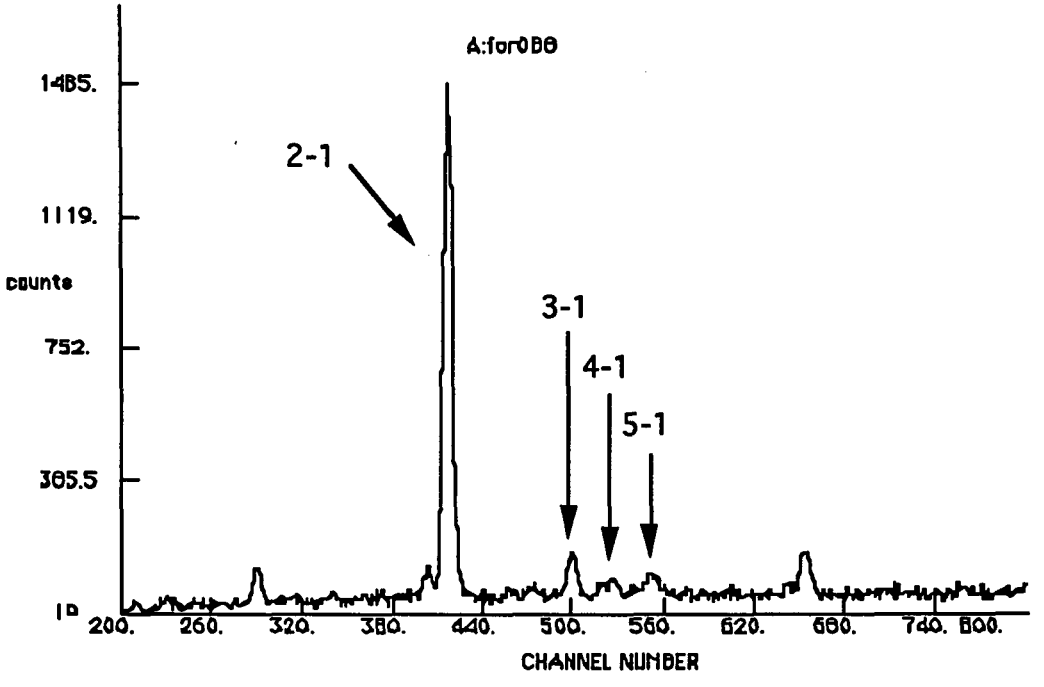

Figure 4-15a μC K-series CH4 150Torr, W&M detector

The delayed events column shows no μC 5-1 or higher transitions, demonstrating that no significant transfer occurred to the n=5 or higher state. A comparison of two plots shows this graphically, one of a pure 150 torr CH4 spectrum (See Fig. 4-15a), which has only prompt μC events, and the other of the 2 μsec gate transfer data fitted above (See Fig. 4-15b). In the first plot most of the events occur in the 2-1 peak with small numbers of 3-1, 4-1, and 5-1 and higher events. The second plot shows a significant number of 3-1 and 4-1 events compared to the 2-1 peak, but no significant number of 5-1 and higher events. These additional 3-1 and 4-1 events are attributed to transfer, since they do not occur in the prompt energy spectrum. Thus no evidence for transfer to states higher than n=4 occurred in the transfer process.

The relative yields of the K-series lines were calculated using the subtracted values of the 0.5 to 2 μsec range data, and are shown in Table 4-24. These ratios have

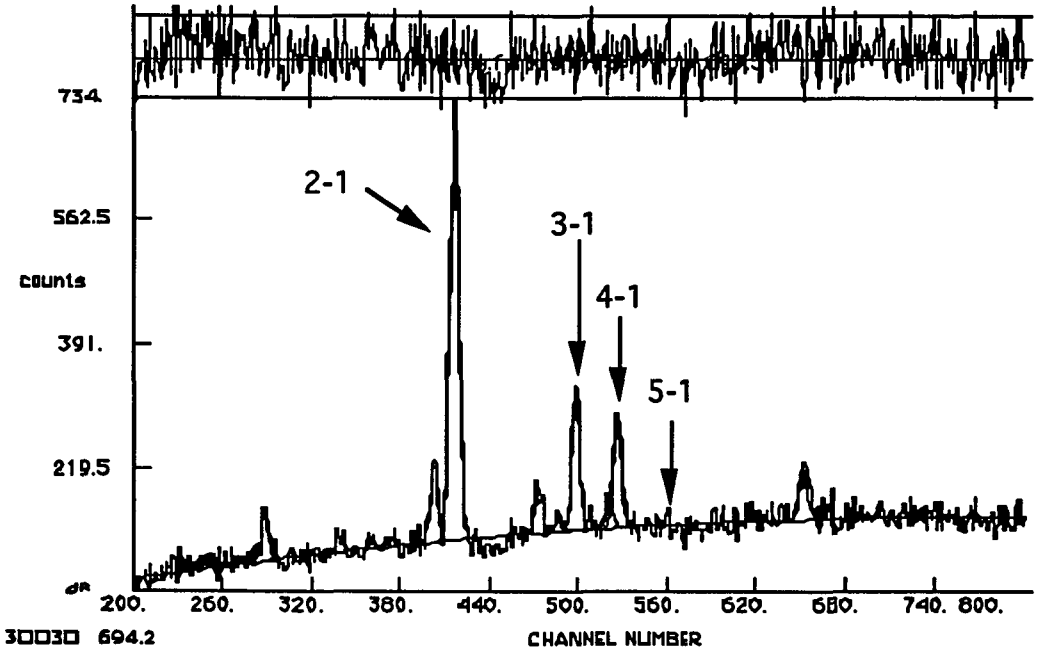

Figure 4-15b μC K-series Tevt2 promp + delayed, W&M detector.

Table 4-24 Yield ratios among μC K lines.

Ratios	
$\frac{3-1}{2-1} = 0.442 \pm 0.042$	
$\frac{4-1}{2-1} = 0.344 \pm 0.043$	$\frac{4-1}{3-1} = 0.777 \pm 0.103$
$\frac{5-1}{2-1} < 0.02$	

much smaller uncertainties than those constructed from the Silgard detector data 4-2, 4-3, and 3-2 lines, due to the much higher statistics produced in this detector. The K-series ratios therefore will be most significant in later determining the cascade after transfer. Unfortunately the energy range of the two detectors did not overlap, so no lines were in common between the spectra, which prevented comparison of data between the two detectors. Therefore, no yield ratios were calculated between the lines of different detectors. This made determining the subsequent cascade sequence less certain.

G. μC Cascade after Transfer

The Gershtein ratio values were calculated from the cascade values in Table 2-6, and both the experimental and theoretical values are shown in Table 4-25. There are significant disagreements between the two sets of values, specifically the 3-1/2-1 and 4-3/3-2 ratios. The 3-1/2-1 ratio is many standard deviations higher for the theory than experiment, and the 4-3/3-2 is almost two standard deviations smaller.

Cascade calculations and programs to simulate cascades have been around for many years, and are based on well accepted transition rates. Both of the cascade programs mentioned here, that of Markushin and of Mulhauser agree well with each other, and agree well with data from previous experiments[7, 15]. This suggests that the

Table 4-25 Yield ratios from experimental data and theoretical values constructed using the Gershtein initial state population and the Holtzwarth and Pfeiffer population, for muon cascade after transfer from deuterium to the n=4 state of carbon.

Yield Ratio	Experimental Values	H&P Population	Gershtein Population
$\frac{3-1}{2-1}$	0.442 ± .042	0.782	0.798
$\frac{4-1}{2-1}$	0.344 ± .043	0.510	0.266
$\frac{4-3}{3-2}$	0.43 ± .16	0.179	0.173
$\frac{4-2}{3-2}$	0.20 ± .14	0.391	0.253

initial population may not be accurately described by the Gershtein theory since many approximations are made in the Gershtein calculation.

The ratios using the H&P population were calculated from the values in Table 2-7 and are also shown in Table 4-25. These ratios also significantly disagree with the experimental data.

Both the Gershtein and the Holtzwarth and Pfeiffer calculations correctly predict that transfer occurs into the n=4 state. Therefore, the method of calculating crossing terms of the energy levels, which both of these calculations use, appears to work well for finding the energy state after transfer.

If the cascade program is taken to be accurate, then in principle the experimental relative yield ratios provide enough information to calculate the initial state into which the muon is transferred. In the theory section, the cascade yields were calculated for each of the four angular momentum states of the n=4 state using the cascade program of Markushin (See Table 2-5). Because the K-line values are more accurately known compared to the remaining ratios from the Silgard detector, two possible initial

distributions were constructed from these four initial angular momentum states (See Table 4-26), using the two K-line ratios, .

The fraction of 4f and 4p component is about the same in both of these distributions, and includes a contribution of either the 4s or 4d state to complete the composite state. The resulting yields for the remaining lines from the Silgard detector constructed for the two composite states are shown in Table 4-27. The two sets of yields are nearly identical, with only an ≈50% greater 4-2 component for the second composite state. An attempt was made to construct the remaining two Silgard yield ratios from these two state combinations. Unfortunately, the uncertainties in the remaining ratios did not allow a single combination of the two composite states to be made, since the differences between them were too small. Therefore, the best that can be said, is the initial state needed to produce the observed data has a 4p and 4f component as given in the composite states, and some proportional contribution of 4s and 4d to complete the initial state. Either of initial state distributions or any combination of the two is still incompatible with the Gershtein predicted population and that of Holtzwarth and Pfeiffer.

Table 4-26 Two possible initial states created using the μC K-line yield ratios.

I	0.252 (4s) + 0.409 (4f) + 0.339 (4p)
II	0.284 (4d) + 0.377 (4f) + 0.339 (4p)
Gershtein	0.246 (4s) + 0.153 (4p) + 0.248 (4d) + 0.353 (4f)

Table 4-27 Cascade yields for remaining lines from two initial composite states.

I	0.469 (3-2) + 0.052 (4-2) + 0.064 (4-3)
II	0.442 (3-2) + 0.080 (4-2) + 0.060 (4-3)

H. μd Yields and Transfer from Excited States

An interesting question to ask is whether transfer takes place from excited states. This phenomonon has been observed in pionic atoms, but never in muonic atoms. This process of muon transfer while the muon is still cascading in the μd atom, and has not yet reached the ground state, was described previously in the theory section II.F. One possible sign of this occurring is a difference between the μd cascade yield ratios observed in pure deuterium, and ratios observed in the mixture. In this experiment only the μd K- series μd lines were observed, and they were divided into two resolvable peaks, that of the 2-1 and n-1 (n>1).

The fitting of the deuterium peaks was difficult due to their position at the low end of the energy spectrum. There the efficiency drop-off, time slew, and the effects of the constant fraction discriminator threshold occur, creating distortions that must first be accounted for before final values can be found. The effect of time slew was not a problem, since large time cuts were used to ensure that all relevant events were included in the resulting 1-D energy spectrum. The energy efficiency curve was also relatively well known, and was used to calculate the corrected yield ratios after the peaks were fitted. Removal of the detector efficiency effect could not be done to the data before fitting because in general it is not possible to deconvolute the detector resolution from the energy efficiency function.

The effect of the threshold setting was not as easily determined. In principle, if the threshold had stayed the same throughout the experiment a comparison of yield ratios could have been done rigorously, even if the threshold had cut into some of the low energy events. If the threshold had drifted, however, the number of events in the peak just above the threshold would increase or decrease depending on the direction of drift. This change in the number of events in the lower peak would change the ratio of lower energy to higher energy events, the 2-1/n-1 ratio in this case, and might give a false indication of transfer from excited states.

The proximity of the threshold to the μd 2-1 line in the energy spectrum also made it difficult to get a good fit to the background below the μd 2-1 peak. In many cases the fits of the background at low energy varied considerably among data sets from the various conditions, and even among fittings of the same spectrum. These low energy background fits produced by ROBFIT were often sensitive to the initial values assigned in the fitting procedure. This instability in turn affected the area of the μd 2-1 peak. Whenever several fits of the same spectrum produced varied results, a background position between the extremes was taken.

Table 4-28 lists all the relevant data yield ratios, listed in the order that the data were taken. The ratios measured from data recorded on the Macintosh and from the MCA agree within the stated uncertainties, showing no inconsistency between the two recording devices. However, the dead time of the Macintosh was found to be high, around 50%, so total numbers of events were about half that recorded in the MCA, which had a dead time of a few percent. Because the ratios agree, the dead time effects did not appear to affect the quality of the data.

A cascade calculation of the 2-1/n-1 yield ratio in D_2 was done using the Markushin model, which predicts a ratio of 1.02 for deuterium at 697 Torr and 1.12 for

Table 4-28 Raw and energy efficiency corrected 2-1/n-1 (n>2) yield ratios for deuterium and transfer data runs listed in time order of data runs recorded.

	Macintosh		MCA	
2-1/n-1 Yield Ratios	Raw	Efficiency Corrected	Raw	Efficiency Corrected
D_2 697 Torr	0.57 ± .09	0.90 ± .18	0.77 ± .09	1.22 ± .21
D_2 350 Torr	1.25 ± .29	1.98 ± .52	1.18 ± .24	1.86 ± .44
D_2 694 Torr	-	-	1.21 ± .26	1.91 ± .48
Tevt1	0.90 ± .10	1.42 ± .24	1.09 ± .18	1.72 ± .36
Tevt2	0.98 ± .13	1.55 ± .28	0.84 ± .12	1.32 ± .25

350 Torr. The measured ratio for 697 Torr is in agreement with the predicted value, but the 350 Torr ratio is significantly larger. The ratio for the D_2 694 Torr is also significantly higher then predicted, and is inconsistent with the previous 697 Torr measurement. The Markushin cascade model showed excellent agreement with previous experiments done over a wide range of pressures[40], which lends support to the model's accuracy.

Both the 350 and 697 Torr data were taken in a series of runs where only the gas pressure was changed. The 694 data was taken after the last of the 350 data and after a change was made in the ADC gate on the MCA to eliminate a peak assumed to be noise at the extreme low end of the spectrum. No other adjustments were made during the remaining run time, including the time when the transfer data were taken. In principle this change in ADC gate should not effect which events are recorded, since that is a function of the timing circuit, but rather the change affects which region of the energy pulse was sampled for digitizing by the ADC. This could possibly have caused some change in the conversion of pulses that were not well shaped. However, since the ADC is a peak height converting unit and as long as the gate meets the requirement that it start 100ns before the peak maximum the position and width of the gate should not affect the converted value. A gate change for the Macintosh was also attempted at the same time, but no reduction in noise was observed, so the gate was changed back to its original setting.

The 2-1/n-1 ratio for the Tevt2 data constructed from the deuterium peak areas may have included some μC 5-4 events which fall in this energy region. The number of possible carbon events mixed in with the deuterium was estimated from the number of prompt μC 3-2 events in Tevt2 using the ratio of μC 5-4/ 3-2 found from pure methane. The number of μC 5-4 events was estimated to be about 22, a number which is comparable to the uncertainty in the μd fitted peak values. The position of the μC 5-4 peak is approximately in the middle, between the two μd peaks, so the contamination

from the μC 5-4 events was expected to contribute about equally to both μd peaks. This level of contamination was thought to be low enough for its effect to be ignored.

A comparison of the 697 Torr deuterium μd 2-1/n-1 ratio with the Tevt2 transfer data ratio from the Macintosh data shows a change in the ratio, but the MCA data show no such change. This, and the other inconsistancies in Table 4-28, indicate that the μd intensity ratios in mixtures where transfer occured were not measured accurately or reliably enough to permit any conclusion about possible transfer from excited states.

V
CONCLUSION

The transfer of muons from deuterium to carbon was measured in this experiment at a total pressure of 600 torr. In spite of the low-statistics data and the need to do extensive analysis of the data, some significant results were found.

A transfer rate of $(4.5 \pm 1.8) \times 10^{10}$ /sec was found for transfer in a mixture of 30 torr CH_4 and 570 torr D_2. This value is in agreement with a previous high pressure measurement of $(5.1 \pm 1.0) \times 10^{10}$ /sec in a mix of 0.1% CH_4 in D_2 at 50 Bar total pressure. The transfer rate, therefore, does not appear to vary significantly over range of pressures from 1 to 50 Bar.

The initial energy state after transfer was found to be predominantly to the n=4 μC state, which agrees with the predictions of both the Gershtein and the Holtzwarth and Pfeiffer models of transfer. This indicates that the general method used in both of these calculations, that of calculating transfer probabilities at the energy curve crossing points, is an accurate method to use in this pressure region.

Using the cascade calculations of Markushin, the initial angular momentum distribution after transfer was determined from the relative yield ratios obtained from the measured x-ray intensities. Two possible distributions were consistent with the data (See Table 4-26). The low energy line yields (4-2, 3-2, 4-3) were not measured accurately enough to differentiate between these two distributions. Neither angular momentum distribution agrees with those models of Gershtein or of Holtzwarth and Pfeiffer. This may be due to some approximations made in the models in calculating the probability for transfer at the crossing points.

Convincing evidence regarding transfer from excited states (See Table 4-28) could not be developed due to poor statistics, and inconsistent results of analysis of the μd x-ray yields. Hints of such transfer effects appeared in the Macintosh data as a change of x-ray yields in the μd cascade between pure D_2 at 697 torr and the mixture of 570 torr D_2 + 30 torr CH_4. The results were not conclusive, however, due to the unexpected difference of the μd 2-1/n-1 yield ratio in the D_2 350 torr data from that of the 697 torr data. The ratio was expected to be about 10% lower for the lower pressure but instead was found to be almost half as great. The possibility of transfer, and the unexpected cascade results for D_2 at 350 torr suggests another transfer experiment to look specifically for transfer from excited states using methods similar to those described in this work.

Using the cascade model of Markushin and the initial angular momentum distribution determined from the data in this analysis, the population of the 2S state was calculated, and was found to be 5-6% depending on the choice of initial angular momentum distribution (See Table 4-26). The Gershtein initial angular momentum distribution with the Markushin cascade predicts a 7% 2S population, which is similar to the value derived from the data. The initial distribution of Holtzwarth and Pfeiffer with the cascade done by Mulhauser gives a 2S population of 11%, much higher than the other two. This difference is due more to the differences in the cascade calculations than in the initial distribution of the angular momentum. The 2S population, ranging over a factor of two, from 5-11%, is still significantly larger than the population, of about 3%[16], which results from direct capture of the muon on carbon. This suggests that transfer may be a method of populating the 2S state more effectively than by direct capture alone in experiments measuring lifetimes from the 2S state.

REFERENCES

1 M. Shiff, Nuov. Cim., **22** (1961) 66

2 S. G. Baziladze, P. F. Ermolov, K. O. Oganesyan, Sov. Phys. JETP **22** (1966) 725

3 A. Bertin, A. Placci, A. Vitale, E. Zavattini, Nuov. Cim. **64A** (1969) 1053
G. Backenstoss, H. Daniel, K. Jentzsch, H. Koch, H. P. Povel, F. Schmeissner, K. Springer, R. L. Stearns, Phys. Lett. **36B** (1971) 422

4 G. Carboni, E. Iacopini, G. Torelli, V. Trobbiani, Nuov. Cim. **67A** (1982) 201

5 R. Jacot-Guillarmod, F. Bienz, M. Boschung, C. Piller, W. Reichart, L. A. Schaller, G. Torelli, Phys. Rev. **38A** (1988) 6151

6 A. Bertin, M. Bruno, A. Placci, A. Vitale, E. Zavattini, Phys. Rev. **7A** (1973) 462

7 F. Mulhauser, H. Schneuwly, R. Jacot-Guillarmod, C. Piller, L. A. Shchaller, L. Schellenberg, Muon Catalyzed Fusion **4** (1989) 365

8 H. Frauenfelder, E. M. Henley, Subatomic Physics, (Prentice-Hall, Englewood Clifts, N.J., 1974)

9 J. F. Janni, At. Dat. and Nucl. Dat. Tables **27** (1982) 147

10 H. Schmidt Böcking, Experimental Methods in Heavy Ion Physics, (Springer-Verlag, Berlin, 1978)

11 E. Fermi, E. Teller, Phys. Rev. **72** (1947) 399

12 A. S. Wightman, Phys. Rev. **77** (1950) 521

13 J. S. Cohen, R. L. Martin, W. R. Wadt, Phys. Rev. **24A** (1981) 33

14 J. S. Cohen, Phys. Rev. **27A** (1983) 167

15 V. Markushin, Electromagnetic Cascade and Chemistry of Exotic Atoms, (Plenum Press, New York, 1990)

16 H. Anderhub, H.P. von Arb, J. Böcklin, F. Dittus, R. Ferreira Marques, H. Hofer, F. Kottmann, D. Taqqu, J. Unternährer, Phys. Lett. **143B** (1984) 65

17 J. Kraiman, Thesis, College of William and Mary in Virginia, (1989) WMHEG-89-2

18 A. Bertin, M. Capponi, I. Massa, M. Piccinini, G. Vannini, M. Poli, A. Vitale, Nuov. Cim. **72A** (1982) 225

19 S. S. Gershtein, Sov. Phys. JETP, **16** (1963) 501

20 L. D. Landau, J. of Phys. USSR **6** (1932) and **2** (1932) 46

21 V. I. Petrukhin and V. M. Suvorov, Sov. Phys. JETP, **43** (1976) 595

22 V. Markushin, Private communication, April 1993

23 J. J. Livingood, Principles of cyclic particle accelerators, (Van Nostrand, Princeton, 1961)

24 L. M. Simons, Phys. Scrip. **T22** (1988) 90

25 R. L. Coldwell and G. J. Bamford, The Theory and Operation of Spectral Analysis Using ROBFIT, (American Institute of Physics, New York, 1991)

26 K. Debertin and R. G. Helmer, Gamma- and X-ray Spectrometry with Semiconductor Detectors, (Elsevier Science Publishers B. V. , New York, 1988)

27 C.T.A.M. DeLatt, FIT-Program Manual, Ver. 4.04, (Rijksuniversiteit Utrecht, Netherlands, 1991)....

28 D. Abbott, Private communication.

29 G. Arfken, Mathematical Methods for Physicists, (Academic Press, Orlando, Florida, 1985)

30 Abelbeck Software, KaleidaGraph, ver. 2.1.3, 1991

31 L. M. Simons, Private Comunication.

32 J. R. Taylor, Introduction to Error Analysis, (University Science Books, Mill Valley, CA, 1982), p.224

33 A. G. Frodesen, O. Skjeggestad, and H. Tofte, Probability and Statistics in Particle Physics, (Univrsitetsforlaget, Oslo, 1979)

34 L. D. Landau and E. M. Lifshitz, Quantum Mechanics, (Pergamon Press, 1977)

35 V. G. Zinov, A. D. Konin, and A. I. Mukhin, Sov. Phys. JEPT **46** (1964) 1919

36 W. H. Press, S. A. Teukolsky, W. T. Vetterling, and B. P. Flannery, Numerical Recipes, (Cambridge University Press, New York, 1992)

37 P. R. Bevington, Data Reduction and Error Analysis for the Physical Sciences, (McGraw-Hill, 1969)

38 S. G. Basiladze, P. F. Ermolov, K. O. Oganesyan, Sov. Phys. JEPT **22** (1966) 725

39 L. M. Simons, Physica Scripta, **22** (1988) 90

40 V. Markushin, Sov. Phys. JETP **53** (1981) 16

41 G. Holzwarth and H. J. Pfeiffer, Z. Physik **A272** (1975) 311

42 F. Mulhauser, Private communication.

43 L. M. Simons, Electromagnetic Cascade and Chemistry of Exotic Atoms, (Plenum Press, New York, 1990)

44 R. Brun, O. Couet, C. Vandoni, P. Zanarini, PAW - Physics Analysis Workstation, (CERN, Geneva, 1989)

45 Sparrow Corporation, Kmax ver. 5.0, 1993

VITA

David William Viel

Born in New Brunswick, New Jersey, August 28, 1963. Graduated from North Brunswick Township High School in June 1981. Received a B.A. in Physics from Rutgers University in May 1987. Entered the College of William and Mary in August 1987. Received an M.S. in Physics in 1989 and began thesis work toward the Ph. D. Completed degree requirements for Ph. D. in 1994.